# Structure and morphology of ultrathin iron and iron oxide films on Ag(001)

## Dissertation

zur Erlangung des Grades eines
Doktors der Naturwissenschaften (Dr. rer. nat.)

dem Fachbereich Physik der Universität Osnabrück
vorgelegt von

Daniel Bruns, Dipl. Phys.

Osnabrück, Oktober 2012

*In science there are no 'depths';*
*there is surface everywhere.*

- DR. PHIL. RUDOLF CARNAP (1891 - 1970)

# Contents

# 1 Introduction

Iron and iron oxides are of great interest in various fields of application due to their large variety of physical and chemical properties. For instance, iron oxides are well known as catalysts for several chemical reactions as, e.g., selective oxidation or dehydrogenation [1, 2]. One important issue for this application is that the oxidation state of iron is flexible and may either be $Fe^{2+}$ or $Fe^{3+}$. Therefore, iron forms oxides of different stoichiometries as FeO (wustite), $Fe_3O_4$ (magnetite) and $Fe_2O_3$ (haematite (trigonal) or maghemite (cubic)).

Furthermore, during the last years the need for new microelectronic devices with specific magnetic properties increased significantly. Spin-dependent material properties are the reason for phenomena as Giant Magneto Resistance (GMR) [3] and Tunneling Magneto Resistance (TMR) [4] which are very promising for magnetic devices. In GMR devices, two ferromagnetic layers (e.g. iron) are used to switch the electric resistivity of the device. This is done by either parallel or anti-parallel alignment of the magnetization in the ferromagnetic layers (cf. Fig 1.1).

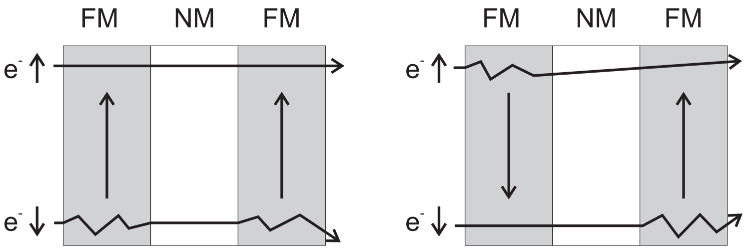

**Figure 1.1:** Illustration of GMR effect. FM stands for a ferromagnetic and NM for non-magnetic (but conducting) layer. The electrons with spin aligned parallel to the magnetization of the ferromagnetic layer are less scattered compared to electrons with spin alignment anti-parallel to the magnetization.

In addition, especially materials with high spin polarization at the FERMI level are searched in the field of *spintronics* [5]. For instance, ferrimagnetic magnetite $Fe_3O_4$ with (cubic) inverse spinell structure is a promising candidate due to its complete spin polarisation at the FERMI level [6].

All oxide devices, which are based on $Fe_3O_4$, are recently demonstrated in Ref. [7, 8]. Contrary to ferrimagnetic magnetite ($Fe_3O_4$), wustite (FeO) is an anti-ferromagnetic material with rocksalt structure. It is well known that anti-ferromagnetic layers can be used as spin valves to increase coercive fields due to pining of the magnetization at the interface. FeO, however, can only be used as spin valve for devices at low temperatures due to its low Neel temperature ($T_N$=198 K). Nevertheless, FeO layers are also studied in the field of spintronics, especially concerning TMR structures [9, 10, 11, 12].

Iron oxide films are often deposited on insulating substrates as MgO(001) because film and substrate both have cubic structures and they are lattice matched (cf. [13] and references therein). However, former studies reported a Mg interdiffusion throughout the $Fe_3O_4$

films accompanied by a Mg segregation at the surface due to annealing at temperatures above 400°C [14, 15]. This Mg interdiffusion reduces the desired spin polarization of the magnetite film.

On the other hand, deposition of iron oxides on metallic substrates has been less investigated. This is surprising since there are thorough studies on other transition metal (TM) oxides on various metal substrates (cf. Ref. [13, 16, 17, 18] as well as references therein). One huge exception for epitaxy of iron oxide on metals is the work of WEISS *et al.* who intensively studied iron oxide epitaxy on Pt(111) [19, 20, 21, 22, 23, 24]. They reported that iron oxide always grows initially as FeO(111) layer and that higher oxidation states are only possible for oxide films with film thickness beyond a few monolayers. It has to be noted that no film-substrate interdiffusion at elevated temperatures was reported for the growth of iron oxide on Pt(111).

Nevertheless, using hexagonal substrate surfaces, the formation of (111) oriented FeO films may not be too surprising. The formation of quasi-hexagonal FeO(111)-like monolayers, however, has also been reported for deposition on fcc(001) surfaces with square symmetry as, e.g., Pt(001) [25, 26] and Cu(001) [27, 28]. Here, FeO forms c(2×10) or (2×9) superstructures on Pt(001) while hexagonal MOIRÉ patterns, due to strain reducing dislocation networks, are reported for Cu(001).

Although LOPES et al. investigated the structure of 22 ML FeO(001) films on Ag(001) [29], studies on the initial growth of iron oxide layers on Ag(001) are still lacking in literature. This is astonishing, since the lattice mismatch between FeO and Ag is smaller than between FeO and other noble metal substrates (e.g. Pt).

Therefore, this work investigates the initial growth of iron and iron oxides on Ag(001). Surface structure and morphology of both post deposition annealed Fe films (in UHV and $O_2$ atmosphere) as well as reactive grown iron oxide films will be analyzed in detail by low energy electron diffraction (LEED) and scanning tunneling microscopy (STM). The stoichiometry at the surface of the iron oxide films will be determined by X-ray photoelectron spectroscopy (XPS) and AUGER electron spectroscopy (AES).

The necessary theoretical background of the techniques as well as the material system used in this work are introduced in Chap. 2 and Chap. 3, respectively.

In a first step, studies on elemental Fe films deposited on Ag(001) at RT will be briefly introduced. Afterward, the segregation of Ag at the surface of the Fe films during UHV annealing will be investigated (Chap. 5.3). This segregation has been reported for monolayer Fe films as *atom site exchange* in former studies concerning Fe monolayers on Ag(001) [30, 31]. Here, we will concentrate on the changes in surface structure that my be caused by the Ag segregation, since this is still lacking in literature.

However, the main focus of this work is to shed light on the question whether the growth of iron oxide films on Ag(001) is accompanied by the formation of strain reducing dislocation networks, or superstructures as found for other metal substrates in former studies [25, 26, 27, 28]. Here, we will distinguish between Fe films which were post deposition annealed in a thin $O_2$ atmosphere (Chap. 5.4) and reactively grown iron oxide films (Chap. 5.5).

# 2 Theoretical background

In this section the theory of crystal lattices and the theoretical background concerning the experimental methods used in this work will be introduced.

## 2.1 Crystal structures

The main objective of this work is the investigation of structure and morphology of ultra thin crystalline iron oxide films. Therefore, it is useful to first give a brief introduction to three and two dimensional crystal lattices.

### 2.1.1 Bulk lattices

A bulk crystal can be described as a periodic arrangement of atoms or groups of atoms (basis) located in each point of a three dimensional lattice. The lattice itself is defined by a lattice base vector for each spatial direction ($\vec{a}$, $\vec{b}$ and $\vec{c}$). The smallest periodically repeated spatial structure in this lattice is called *(primitive) unit cell* (cf. Fig. 2.1).

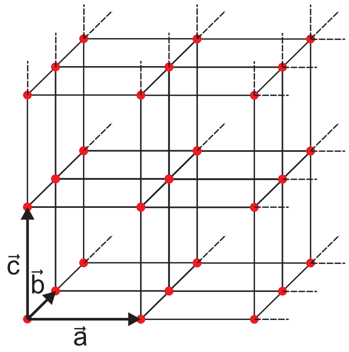

**Figure 2.1:** General composition of a crystal structure. Each point of the lattice contains a basis, represented by the red dots. The unit cell of the lattice is defined by the three lattice vectors ($\vec{a}$, $\vec{b}$ and $\vec{c}$).

The whole bulk crystal is described by translations of a unit cell with the translation vectors $\vec{a}$, $\vec{b}$ and $\vec{c}$ via

$$\mathbf{T} = n_1\vec{a} + n_2\vec{b} + n_3\vec{c}\ , \qquad 2.1$$

with $n_i \in \mathbb{Z}$. Every bulk crystal can be described as a periodic arrangement of unit cells represented by one of the well known BRAVAIS lattices [32]. Crystal lattice planes in this systems are defined by three points in the crystal lattice represented by the MILLER indices $(h, k, l)$. These MILLER indices are calculated easily from the intersection points of the crystal lattice plane with the three crystal axis $x$, $y$ and $z$ as shown in [33].

Later it can be useful to distinguish between the coordinate systems of substrate and film crystal lattice. Therefore, all crystal directions will be named as $X[a_1^* a_2^* a_3^*]$ with $X$ as the specific element or composition forming the crystal lattice from now on. For example Ag[100] as the [100] direction of the Ag substrate.

### 2.1.2 Surface lattices

Infinite extended bulk crystals as introduced in section 2.1.1 do not exist in nature, since every crystal has certain limiting planes and edges. The topmost atomic layers underneath these limiting planes are called the crystal *surface* and can be described by a two dimensional lattice similar to Eq. 2.1 via

$$\mathbf{T} = n_1\vec{a} + n_2\vec{b}\ . \tag{2.2}$$

The crystal planes below the surface are called *bulk*. The crystals that are used to support thin films are commonly called *substrates*. Hence, we will from now on use the phrase *substrate lattice* as a synonym for *bulk lattice*. The chemical surrounding at the surface differs from the surrounding inside the substrate because of missing binding partners. This change can lead to relaxations and reconstructions in the surface lattice if it is energetically favorable. Reconstructions also occur through the adsorption of foreign atoms at the surface. These adsorbate induced reconstructions are called *superstructures*. Therefore, it is necessary to describe the translation operations between the substrate lattice (given by the set of base vectors ($\vec{a}$, $\vec{b}$)) and the reconstructed surface lattice (defined by ($\vec{a'}$, $\vec{b'}$)).

In general, there are two kinds of notations to describe the relation between surface lattice and substrate, namely the WOOD'S notation [34] and the matrix notation according to PARK and MADDEN [35]. The WOOD'S notation can only be used if the surface and the substrate lattice are commensurable, thus, the angle between the base vectors of both lattices have to be the same. If that is the case the WOOD'S notation describes the relation as

$$R(hkl)\left(\frac{\vec{a'}}{\vec{a}} \times \frac{\vec{b'}}{\vec{b}}\right)/\alpha\ , \tag{2.3}$$

while $R$ represents the substrate material, $(hkl)$ are the MILLER indices of the crystal plane parallel to the surface and $\alpha$ is the rotation angle between the base of substrate and surface lattice. For incommensurable surface and substrate lattices the matrix notation according to PARK and MADDEN connects the sets of base vectors via

$$\begin{pmatrix}\vec{a'}\\ \vec{b'}\end{pmatrix} = \begin{pmatrix} m_{11} & m_{12}\\ m_{21} & m_{22}\end{pmatrix}\begin{pmatrix}\vec{a}\\ \vec{b}\end{pmatrix}\ , \tag{2.4}$$

with $m_{ij} \in \mathbb{R}$. In Fig. 2.2 an oxygen induced reconstruction of an Fe(001) surface is shown for illustration. The shown superstructure in Fig. 2.2 can be described by WOOD'S notation as

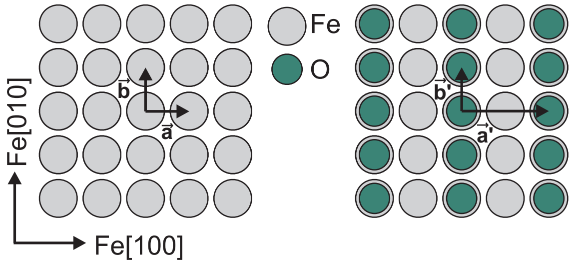

**Figure 2.2:** Illustration of an oxygen induced superstructure on a Fe(001) surface. The base vectors of the unreconstructed surface are $\vec{a}$ and $\vec{b}$, while the superstructure is defined by the base vectors $\vec{a'}$ and $\vec{b'}$ .

$$\mathrm{Fe}(001)(2 \times 1)\ , \tag{2.5}$$

while matrix notation according to Park and Madden gives

$$\begin{pmatrix} \vec{a'} \\ \vec{b'} \end{pmatrix} = \begin{pmatrix} 2 & 0 \\ 0 & 1 \end{pmatrix} \begin{pmatrix} \vec{a} \\ \vec{b} \end{pmatrix}\ . \tag{2.6}$$

### 2.1.3 Growth modes

The epitaxial growth of a thin crystalline film on a substrate is conditioned by the crystal structures, lattice misfit and the surface energies of film, substrate and interface. If the crystal structure of film and substrate are the same and the surface energies are in the same order of magnitude the growth of the film is dominated by the lattice misfit $\eta_0$ with

$$\eta_0 = 2 \cdot \frac{b_0 - a_0}{b_0 + a_0}\ . \tag{2.7}$$

Here $a_0$ and $b_0$ are the lattice constants of the substrate and the film, respectively [36]. Large lattice misfits lead to strain, which is decreased by the formation of e.g. dislocations, mosaics and undulations (dislocation networks) as will be introduced later. This is not the case if the lattice misfit between film and substrate is very small or the system consists of different crystal structures and different types of bindings (e.g. ionic crystal/metal). In this case, the ratio between the surface free energies of film and substrate and the interface free energy governs the growth mode [36]. The growth of Fe on Ag(001) (lattice misfit 0.7%) and its oxides ($\mathrm{FeO_x}$/Ag(001) (ionic crystal/metal)), studied in this work, depends strongly on the different surface free energies [37, 38, 39]. Hence, the different growth modes and their dependence on the surface free energies will be discussed in the following.

According to Ref. [40] the total free energy $F$ of a heterosystem can be approximated via

$$
\begin{aligned}
F = {} & C_0 + C_1 d + f\alpha_i + (1-f)\alpha_1 + f_2\alpha_2 \\
& \underbrace{+ f\mathrm{B}\int \mathrm{d^3x}\epsilon(\mathrm{x}) + f\mathrm{D}\sum \mathrm{b_i}\left[\ln\frac{\mathrm{R}}{\mathrm{b_i}+1}\right] - \mathrm{TS}}_{\text{strain}} \ .
\end{aligned}
\tag{2.8}
$$

Here, $C_0$ and $C_1$ are the free energies of substrate and film, respectively, while $d$ is the film thickness. The factor $f\alpha_i$ is a measure for the free energy of the interface per substrate area with $f$ as the part of the substrate covered by the film. Furthermore, $(1-f)\alpha_1$ is the free energy of the uncovered substrate area and $f_2\alpha_2$ the free energy of the film surface. Here, $f_2$ is the fraction of the film surface that covers the substrate surface. The last three terms will not be apportioned in detail here, since they are not important for further considerations. They include a homogeneous strain term resulting from lattice misfit (integral term), an energy contribution from strain fields caused by dislocations (sum term) and an entropy term due to defects and islands (TS) [36, 40]. These terms are embraced as 'strain' in Eq. 2.8.

If the growth of a film is determined by the surface free energies in the system (see above) the 'strain' terms in Eq. 2.8 can be neglected and the total free energy of the system simplifies to

$$
F \approx C_0 + C_1 d + f\alpha_i + (1-f)\alpha_1 + f_2\alpha_2 \ . \tag{2.9}
$$

It can be assumed, that the surface area of a film is larger (islands) or of the same size (flat layer) as the substrate surface area ($f_2 \geq f$) if the deposited amount of film material is more than 1ML (monolayer). According to [36] $f_2$ can, therefore, be approximated to

$$
f_2 \approx f + G_1 d \left(\frac{N_i}{f}\right)^{\frac{1}{2}} \ , \tag{2.10}
$$

with $N_i$ as the number of islands and $G_1$ as a geometry factor describing the island shape. In order to mathematically determine the minimal total free energy of the system (at thermodynamic equilibrium), the coverage $f$ is varied resulting in

$$
f = \begin{cases} \left(\frac{G_1\alpha_2 d\sqrt{N_i}}{2(\alpha_2-\alpha_1+\alpha_i)}\right) & : \alpha_2 - \alpha_1 + \alpha_i > 0 \\ 1 & : \alpha_2 - \alpha_1 + \alpha_i \leq 0 \ . \end{cases} \tag{2.11}
$$

With $\Delta\alpha = \alpha_2 - \alpha_1 + \alpha_i$ follows

$$\Delta\alpha \leq 0 \;\Rightarrow\; \textit{Frank-van-der-Merve}\text{ growth (layer} - \text{by} - \text{layer) and} \tag{2.12}$$

$$\Delta\alpha > 0 \;\Rightarrow\; \textit{Volmer-Weber}\text{ growth (islands) .} \tag{2.13}$$

If the neglected 'strain' terms from Eq. 2.8 are considered again, the third growth mode known as *Stranski-Krastanov* growth can be described. In this growth mode, the film grows pseudomorphous on the substrate up to a critical film thickness $d_{\text{crit}}$. For $d > d_{\text{crit}}$ the film starts to grow in three dimensional islands.

Fig. 2.3 illustrates the three growth modes for hetero-epitaxy.

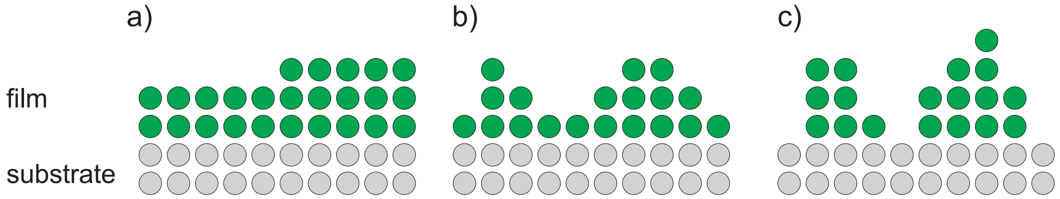

**Figure 2.3:** Different growth modes for epitaxial growth. **a)** FRANK-VAN-DER-MERVE, **b)** STRANSKI-KRASTANOV and **c)** VOLMER-WEBER growth.

## 2.2 Low Energy Electron Diffraction

Two important measurement techniques used for this work (LEED and SPA-LEED) are based on the principle of electron diffraction. The diffraction of slow electrons at crystal lattices was first observed by THOMSON and DAVISSON in the 1920s independently from each other [41]. It was found, that electrons with low kinetic energy ($E_{\text{kin}} < 1000\,\text{eV}$) can be diffracted at crystal lattices, since their DE-BROGLIE wavelength is in the magnitude of atomic distances in crystal lattices. The mean free path of electrons with this energy in matter is about 10 Å which makes this technique very surface sensitive [42]. The reciprocal lattice of a surface is a two dimensional lattice with rods extending perpendicular from each reciprocal lattice point. These diffraction rods can be seen as regions where the reciprocal lattice points are infinitely dense. The resulting pattern of an electron diffraction experiment represents the intersection of the EWALD sphere and the reciprocal lattice [43].

Furthermore, the observed diffraction pattern is always an average over a large area of the radiated sample surface. Therefore, local point defects, which are not periodically ordered, do only distribute to the diffuse background and not to the diffracted intensity. Nevertheless, periodically distributed defects like atomic steps, mosaics or dislocation networks influence the diffracted intensity and can, therefore, be analyzed. This is an advantage compared to imaging techniques that only show a very local part of the sample surface.

### 2.2.1 Kinematic theory of electron diffraction

Since electrons are charged particles there is a strong COULOMB interaction between the incoming electrons and the atoms at the sample surface. Thus, single scattering processes do almost never appear in an electron diffraction experiment. A precise description of the diffraction processes using the dynamic theory of electron diffraction is very complicated, since it includes multiple scattering processes. Therefore, a widely applied simplification is given by the kinematic theory of electron diffraction. Here, the sample surface is treated as a periodic arrangement of column like unit cells with the same form factor that reach into the bulk (cf. Fig. 2.4).

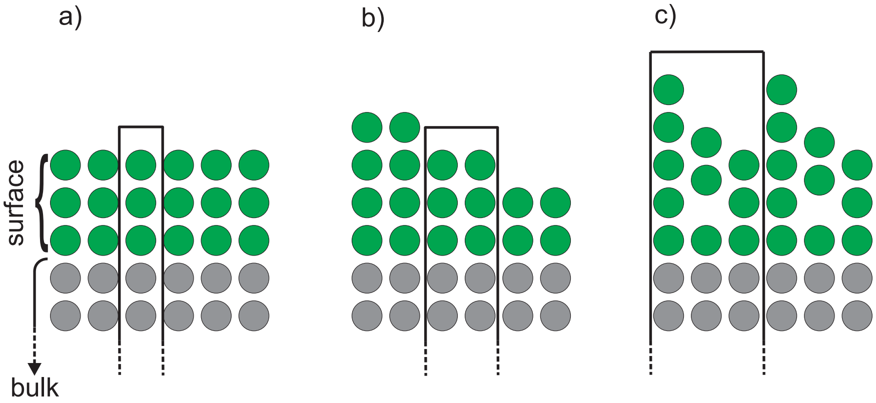

**Figure 2.4:** Column like unit cells in the kinematic theory of diffraction. a) shows an ideal surface, b) a surface with atomic steps and c) a surface with superstructures. Image was taken and adapted from Ref. [44].

In this kinematic approach side scattering processes are neglected while multiple forward and backward scattering processes inside one column are still considered. This is a sufficient assumption, since the amplitude of the atomically scattered spherical wave is angular dependent and mainly takes place in forward and backward direction [45]. In Fig. 2.5 a polar plot illustrates the angular dependence of the squared atomic scattering amplitude for low energy electrons in platinum.

Furthermore, the diffracted electrons can be treated as plane waves since the distance between electron source, sample and detector is much bigger than the electron wavelength $\lambda_{e-}$ (FRAUNHOFER-approximation). Therefore, a plane wave that is diffracted at the column of 0th order at the position $\vec{r}$ can be described as

$$\psi_0(\vec{k}_i, \vec{k}_f, \vec{r}) = f_0(\vec{k}_i, \vec{k}_f) \cdot e^{i\vec{k}_f \vec{r}} \; . \qquad 2.14$$

Here, $\vec{k}_i$ is the vector of the incoming electron wave and $\vec{k}_f$ the vector of the scattered wave. $f_0$ is the form factor of the scattering column. If the electron wave is scattered on

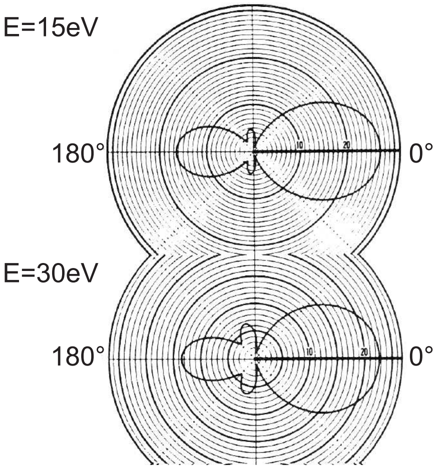

**Figure 2.5:** Polar plot of the squared atomic scattering amplitude for low energy electrons scattered at platinum. Image taken and adapted from Ref. [45].

an arbitrary column at the position $\vec{r}_n$ a phase shift $\Delta\phi = \vec{K} \cdot \vec{r}_n$ with $\vec{K} = \vec{k}_i - \vec{k}_f$ leads to

$$\psi_n(\vec{k}_i, \vec{k}_f, \vec{r}_n) = e^{i\vec{k}_f\vec{r}} \cdot f_n(\vec{k}_i, \vec{k}_f) \cdot e^{i\vec{K}\vec{r}_n} \tag{2.15}$$

for the amplitude of the diffracted wave, with $f_n$ as the form factor of the $n$-th column. The intensity in the diffraction pattern is mathematically described by the detection probability which is the square of the amplitude of all diffracted electron waves

$$I(\vec{k}_i, \vec{k}_f) = \frac{I_0}{N} \cdot \underbrace{\left| e^{i\vec{k}_f\vec{r}} \right|^2}_{=1} \cdot \left| \sum_{n=0}^{N} f_n(\vec{k}_i, \vec{k}_f) \cdot e^{i\vec{K}\vec{r}_n} \right|^2 , \tag{2.16}$$

where $N$ is the number of columns at the surface. Assuming that all columns are equivalent and have the same form factor ($f_n = f_0$) this sum can be simplified to

$$I(\vec{k}_i, \vec{k}_f) = \frac{I_0}{N} \cdot \left| \underbrace{f_0(\vec{k}_i, \vec{k}_f)}_{F} \right|^2 \cdot \left| \underbrace{\sum_{n=0}^{N} e^{i\vec{K}\vec{r}_n}}_{G} \right|^2 \tag{2.17}$$

$$\Rightarrow I(\vec{k}_i, \vec{k}_f) \propto \left| F(\vec{k}_i, \vec{k}_f) \right|^2 \cdot \left| G(\vec{K}) \right|^2 . \tag{2.18}$$

$F$ is the dynamic form factor of a column which, in the kinematic theory of electron diffraction, is the same for all columns. $G$ is the lattice factor that describes the periodicity of the columns and contains information about position and shape of the diffracted intensity. Therefore, the lattice factor $G$ can be used to investigate the crystal structure and morphology of the sample surface. The dynamic form factor $F$ describes the absolute intensity of the diffracted intensity peaks in the diffraction pattern. It also contains multiple scattering processes and is, therefore, not exactly described in the kinematic theory of electron diffraction. Hence, in the following we will concentrate on the description of the lattice factor $G(\vec{K})$, which can be written as

$$\left|G(\vec{K})\right|^2 = G(\vec{K})G(\vec{K})^* = \sum_n \sum_m e^{i\vec{K}\vec{r}_n} e^{-i\vec{K}\vec{r}_m} = \sum_{n,m} e^{i\vec{K}(\vec{r}_n - \vec{r}_m)} \ , \tag{2.19}$$

where the scattering centers are located at the crystal lattice positions

$$\vec{r}_n = n_1\vec{a} + n_2\vec{b} + (n_1, n_2)\vec{d} \ , \tag{2.20}$$

with $n_1, n_2 \in \mathbb{Z}$ [46]. Here, $\vec{a}$ and $\vec{b}$ are the surface lattice vectors and $\vec{d}$ is the vector perpendicular to the surface with the length of the layer distance. Assuming an ideal surface with no height differences between the unit cells (no steps) the position of the scattering centers simplifies to

$$\vec{r}_{n,ideal} = n_1\vec{a} + n_2\vec{b} \ . \tag{2.21}$$

Additionally, the scattering vector $\vec{K}$ can be separated into its parts perpendicular and parallel to the surface via $\vec{K} = \vec{k}_\perp + \vec{k}_\parallel$. For an ideal surface without any steps $\vec{k}_\perp$ is arbitrary in the LAUE conditions for constructive interference [33]. Thus, the scattering vector reduces to its parallel component $\vec{K} = \vec{k}_\parallel$ and Eq. 2.19 can be transformed into

$$\left|G(\vec{K})\right|^2_{ideal} = \sum_n e^{i\vec{k}_\parallel \vec{r}_{n,ideal}} = \sum_{n_1,n_2} e^{i\vec{k}_\parallel (n_1\vec{a} + n_2\vec{b})} \ . \tag{2.22}$$

It is known from LAUE theory [33] that the direct product of the primitive base vectors of reciprocal and real space is given by the LAUE equations

$$\vec{a} \cdot \vec{k}_\parallel = 2\pi h \text{ and} \tag{2.23}$$

$$\vec{b} \cdot \vec{k}_\parallel = 2\pi k \ , \tag{2.24}$$

with $h$ and $k$ as the MILLER indices.

Therefore, Eq. 2.22 results in

$$\left|G(\vec{K})\right|^2_{ideal} = \sum_{n_1,n_2} e^{2\pi i(n_1 h + n_2 k)} \ . \tag{2.25}$$

Since $n_1, n_2, h, k \in \mathbb{Z}$, this is a delta distribution of the diffracted intensity. This delta distribution represents the expected diffraction pattern from an ideal surface.

### 2.2.2 Atomically stepped surfaces

In an experiment, however, no ideal surfaces are examined as assumed in the former paragraph. Therefore, during the investigation of a sample surface using electron diffraction, additional interference effects between electron waves do appear. The electron waves can for example be diffracted on different terraces which are separated by atomic steps. These steps induce a path difference between the diffracted electron waves what leads to constructive or destructive interference (cf. Fig. 2.6). Here it is useful to introduce the scattering phase $S$ giving information whether the mentioned interference is constructive or destructive.

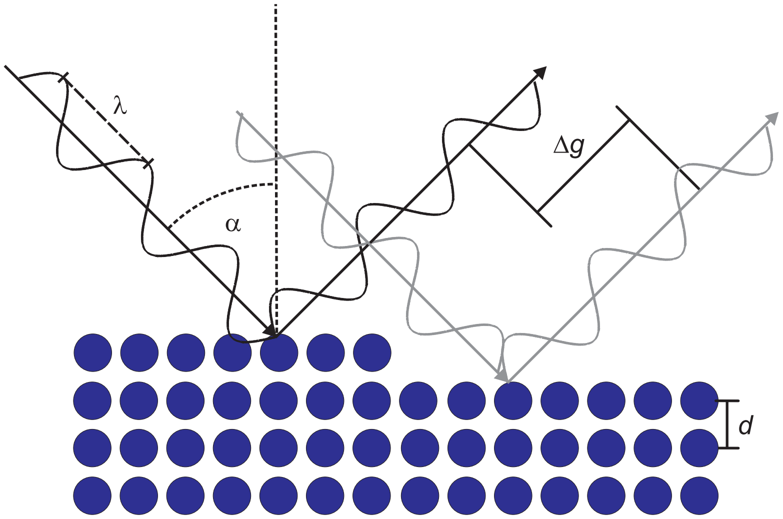

**Figure 2.6:** Path difference $\Delta g$ of two electron waves with the same De-Broglie wavelength $\lambda$ diffracted at an atomic step. The incidence angle of the electron waves is $\alpha$, while the step height at the surface is $d$.

The path difference $\Delta g$ between the two diffracted electron waves (0th order) can be calculated due to geometric reasons and in correspondence to the Bragg condition via

$$\Delta g = S\lambda = 2d\cos(\alpha) \ , \qquad 2.26$$

with step height $d$ and incidence angle $\alpha$. Using the wave number $\left|\vec{k}\right| = 2\pi/\lambda$ with its perpendicular part $\left|\vec{k}_\perp\right| = 2\left|\vec{k}\right|\cos(\alpha)$, Eq. 2.26 can be transposed to

$$S = \frac{\left|\vec{k}_\perp\right| d}{2\pi} \ . \qquad 2.27$$

In accordance to the Bragg condition (cf. Eq. 2.26) constructive interference occurs if $S$ is an integral number (*in-phase*), while for half integral $S$ the interference is destructive (*out-of-phase*). From an experimental point of view it is useful to describe the relation between the scattering phase $S$ and the electron energy, since this is the important tunable parameter in an electron diffraction experiment. Therefore, the De-Broglie wavelength $\lambda = 2\pi\hbar/\sqrt{2m_e E}$ is inserted into Eq. 2.26 which results in

$$S = \frac{d\cos(\alpha)\sqrt{2m_e E}}{\pi\hbar} \ . \qquad 2.28$$

In Chap. 2.2.1 it was shown that the shape of a diffraction spot from an ideal surface is a delta function. Nevertheless, the interference effects of the diffracted electrons at a stepped surface lead to a broadening of the observed diffraction spot. Basically, there are two kinds of stepped surfaces that result in different kinds of broadened diffraction spots. For surfaces that can be described as a two-level surface (flat surface with only two exposed layers) the diffraction spots split into two parts. The first part is a $\delta$-peak corresponding to the flat terraces as it occurs due to electron diffraction on a perfectly flat surface. The second part is a broad shoulder (diffuse shoulder) that results from the interference of electrons at the step edges between the flat terraces. The ratio of both parts depends on the scattering condition [47]. At an *in-phase* or *out-of-phase* condition only the $\delta$-peak or the diffuse shoulder can be observed, respectively, while between *in-* and *out-of-phase* the spot profile is a superposition of the $\delta$-peak and the shoulder (cf. Fig. 2.7).

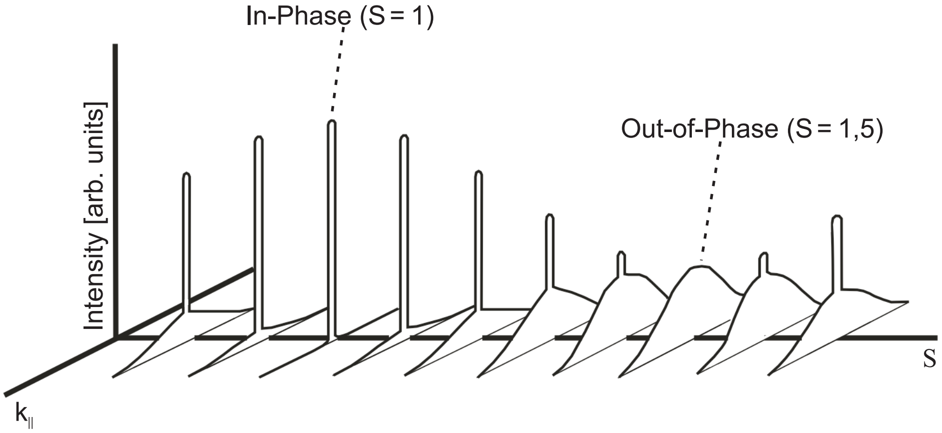

**Figure 2.7:** Observed profiles of electron diffraction spots from a randomly stepped, two level surface for different scattering phases $S$. Image is taken and adapted from Ref. [46].

For a two level surface the FWHM of the diffuse shoulder does not change with changing scattering condition and is a measure for the average size of the terraces that are separated by steps [47].

A rough surface which can not be described by a finite number of layers is called multilevel surface. The diffraction spots obtained from a multilevel surface can not be separated into two parts. The FWHM of these diffraction spots varies periodically with the scattering phase while the peak form at an *in-phase* condition is still $\delta$-shaped [47].

### 2.2.3 H(S) analysis

A typical analysis method to get information about the lateral surface morphology is the so-called *H(S) analysis*. Please note, that the theory introduced in the following applies not to two level surfaces without any non-periodically distributed defects (inhomogeneities). On the other hand, this analysis can be applied to multilevel surfaces as well as to two-level surfaces including inhomogeneities. A detailed explanation for this this restriction is given by WOLLSCHLÄGER et al. in Ref. [48]. For simplification reasons, the mathematical description of the H(S) analysis will be given for the one dimensional surface model. In the end the necessary formula will be expanded to the two dimensional theory.

For an H(S) analysis the dependence of the FWHM of the diffraction spot on the scattering phase is studied. There are several free parameters for the evaluation of experimental diffraction data. Thus, some assumptions have to be made to successfully apply an H(S) analysis to the data. The first assumption is a geometric terrace width distribution $P_T(\Gamma)$. Therefore, the probability to find larger terraces decreases exponentially with the terrace width. Secondly, a variation in step heights on the surface is assumed by the symmetric step height distribution $P_S(h)$. With this and according to Ref. [47] the diffracted intensity spot profile can be described via

$$G(\vec{k}_{||}) = \frac{1}{2[1-\cos(|\vec{k}_{||}|a)]}\left[\frac{(1-\beta_S)(1-\beta_T)}{(1-\beta_S\beta_T)} + \text{c.c.}\right] , \qquad 2.29$$

where $\vec{k}_{||}$ is the parallel part of the scattering vector $\vec{K}$ and $a$ is the lateral lattice constant. $\beta_S$ and $\beta_T$ are the FOURIER transformations of the step height and terrace width distributions $P_S\ (h)$ and $P_T\ (\Gamma)$, with

$$\beta_S = \sum_h P_S(h)e^{i2\pi Sh} \text{ and } \beta_T = \sum_\Gamma \mathrm{P}_T(\Gamma)e^{iak_{||}\Gamma} , \qquad 2.30$$

respectively. With this, the profile of the diffraction spot can be approximated by a LORENTZIAN function via

$$G(k_{||}) \propto [\kappa^2 + (a\Delta k_{||})^2]^{-1} , \qquad 2.31$$

where $\kappa$ is the half FWHM of the diffraction spot for a geometric terrace width distribution and is determined by

$$2\kappa = a\Delta k_{||} = \frac{2(1-\beta_S(S))}{\langle\Gamma\rangle} \ , \tag{2.32}$$

as shown in Ref. [46]. For single atomic steps with uniform height ($h \in \{1,-1\} \rightarrow P_S(h) = \frac{1}{2}$) follows from Eq. 2.30

$$\beta_S(S) = \frac{1}{2}e^{i2\pi S} + \frac{1}{2}e^{-i2\pi S} = \cos(2\pi S) \ , \tag{2.33}$$

and, therefore, the FWHM of the spot profile results in

$$a\Delta k_{||} = \frac{2(1-\cos(2\pi S))}{\langle\Gamma\rangle} \ . \tag{2.34}$$

It is useful to convert the FWHM of the diffraction spots into units of [%BZ], since experimental data usually gives disctances between diffraction spots in percentage of the Brillouin-zone. The spot profiles FWHM ($\Delta\tilde{k}_{||}$) expressed in units of [%BZ] is

$$\begin{aligned} \Delta\tilde{k}_{||} &= \frac{a\Delta k_{||}}{2\pi} \cdot 100\%BZ && (2.35) \\ &= \frac{\kappa}{\pi} \cdot 100\%BZ = \frac{100\%BZ(1-\cos(2\pi S))}{\langle\Gamma\rangle\,\pi} \ . && (2.36) \end{aligned}$$

Fig. 2.8 shows the dependency of FWHM of the diffuse shoulder on the scattering phase $S$ according to Eq. 2.36.

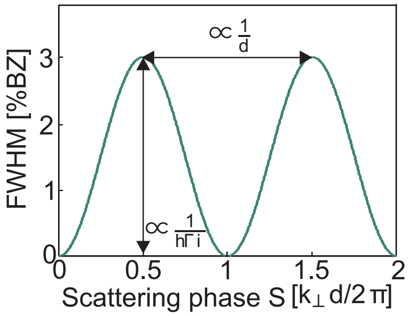

**Figure 2.8:** FWHM of the diffuse shoulder depending on the scattering phase for rough surfaces. The vertical layer distance $d$ can be determined by the distance between the maxima of the FWHM and the mean terrace width $\langle\Gamma\rangle$ can be calculated from the difference of maxima and minima. Image is taken and adapted from Ref. [46].

As mentioned before, the formalism presented up to now is only valid for the one dimensional model. The expansion to the two dimensional theory will be presented now.

### 2.2.4 Two dimensional model in H(S) analysis

In an experiment the electrons are diffracted at two dimensional surfaces. Therefore, corrections have to be applied to the presented theory. The easiest approach to expand the one dimensional to a two dimensional theory is the replacement of the LORENTZIAN function approximating the lattice factor $G(\vec{K})$ by a modified LORENTZIAN which will be described now very briefly. Since the mathematical derivation goes beyond the scope of this work, please see Ref. [47] for details. In general, the shape of the function describing the lattice factor $G(\vec{K})$ is determined by the pair correlation function $C(\vec{r})$. Having a scattering center at the position $\vec{r} = 0$, this pair correlation function describes the probability to find a second scattering center at a given position $\vec{r} \neq 0$. If the pair correlation function is the same for every direction (isotropic), this leads to a modified LORENTZIAN function

$$G(\vec{k_{||}}) \propto [1 + (\vec{k_{||}}/\kappa)^2]^{-\frac{3}{2}} \tag{2.37}$$

approximating $G(\vec{k_{||}})$ at a two dimensional surface [47]. The mentioned assumption of an isotropic pair correlation function can be proved in the experiment by the symmetry of the diffraction spots. From this correction of the LORENTZIAN function follows $a\Delta k_{||} \neq 2\kappa$. Thus, the modification of the spot profile approximation function (Lor→Lor$^{\frac{3}{2}}$) leads to a correction term in Eq. 2.36 giving

$$\begin{aligned} \Delta\tilde{k}_{||,\mathrm{2D}} &= \sqrt{2^{\frac{1}{\alpha}} - 1} \left[\frac{100\% BZ(1 - \cos(2\pi S))}{\langle\Gamma\rangle\,\pi}\right] && 2.38 \\ &= \sqrt{2^{\frac{2}{3}} - 1} \left[\frac{100\% BZ(1 - \cos(2\pi S))}{\langle\Gamma\rangle\,\pi}\right] , && 2.39 \end{aligned}$$

with $\alpha = 3/2$ as the modification factor originating from (Lor→Lor$^{\frac{3}{2}}$).

### 2.2.5 Mosaics and facets

In Chap. 2.2.3 it is presumed that the only surface irregularities are steps that separate the terraces while the surface normal is the same for every terrace. At a real surface, however, mosaics can appear if small areas of the surface (crystallites) are tilted against each other. This happens if it is energetically favorable to reduce strain inside the crystal through the formation of mosaics. The formation can be triggered by different treatments like heating. Especially metals can form dislocations inside the bulk which finally result in surface mosaics [33]. Concerning thin films, one reason for the formation of mosaics can be a large lattice misfit between film and substrate for example. In the case of surface mosaics the surfaces of the different crystallites are tilted against each other. Thus, the crystallites surface normals (and, with this, the diffraction rods) are tilted the same way. If the crystallites are not tilted in a specific orientation the tilt angles $\theta$ are distributed with a standard deviation $\Delta\theta \neq 0$ [46]. Therefore, the FWHM of the diffraction spots increases with increasing scattering phase $S$ (increasing vertical scattering vector $\vec{k}_\perp$) (cf. Fig. 2.9). The standard deviation of the mosaic spread for mosaics with no preferred orientation can be obtained via

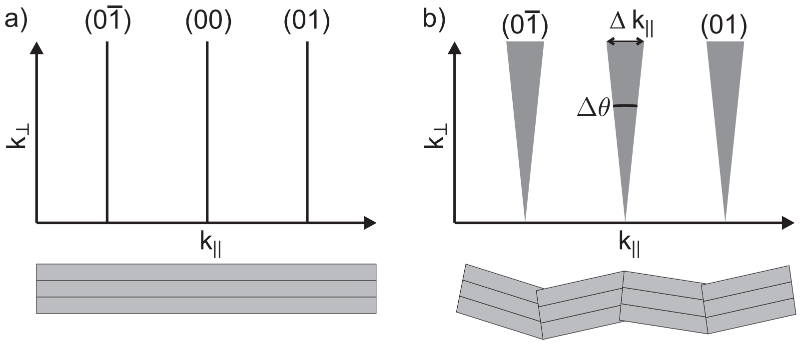

**Figure 2.9: a)** Diffraction rods from an ideal surface. **b)** Diffraction rods from a surface with mosaics without preferred direction. The FWHM increases linear with the scattering vector $\vec{k}_\perp$. Image is taken from Ref. [46] and modified.

$$\frac{\Delta k_{||}}{2 \cdot k_\perp} = \tan\left(\frac{\Delta\theta}{2}\right) \approx \frac{\Delta\theta}{2} \ , \tag{2.40}$$

for small angles $\theta$. Together with Eq. 2.36 and 2.27 the standard deviation of the mosaic spread results in

$$\frac{\Delta\theta}{2} \approx \frac{d \cdot \Delta\tilde{k}_{||}}{a \cdot 200\%\mathrm{BZ} \cdot \mathrm{S}} \ , \tag{2.41}$$

where $d$ denotes the step height and $a$ the lateral lattice constant of the investigated surface. The linear increase of FWHM of the diffraction spots due to such mosaics also affects the prior shown H(S) analysis (Chap. 2.2.3). A linear term is added to Eq. 2.36 (one dimensional theory) in order to incorporate the mosaic spread by

$$\Delta\tilde{k}_{||,\mathrm{mosaic}} = \left[\frac{100\%BZ(1-\cos(2\pi S))}{\langle\Gamma\rangle\,\pi} + \frac{a}{d}\Delta\theta \cdot S\right] \ . \tag{2.42}$$

Expansion to the two dimensional theory (cf. Eq. 2.39) results in

$$\Delta\tilde{k}_{||,\mathrm{mosaic,2D}} = \sqrt{2^{\frac{2}{3}}-1}\left[\frac{100\%BZ(1-\cos(2\pi S))}{\langle\Gamma\rangle\,\pi} + \frac{a}{d}\Delta\theta \cdot S\right] \ . \tag{2.43}$$

Again, $a$ is the lateral lattice constant and $d$ the step height at the surface. Fig. 2.10 illustrates the influence of mosaics without preferred orientation on the dependence of the FWHM on the scattering phase.

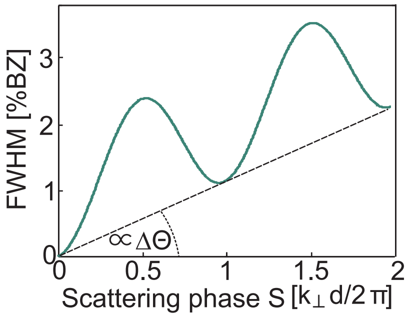

**Figure 2.10:** FWHM of the diffuse shoulder depending on the scattering phase for rough surfaces with mosaics without preferred orientation. The mosaic spread $\Delta\theta$ can be determined by the inclination angle of the curve. Image is taken and adapted from Ref. [46].

Other structural features at the surface that influence the diffraction experiments are facets. Even though facets were not detected at any surface during this work, it is useful to know how facets influence the diffraction pattern for later discussion of some experimental results. In contrast to mosaics, facets are no tilted crystallites but consist of short terraces of the same length, while the surface normal of each terrace is still the same as for the ideal substrate. Only the average orientation angle of the whole facet is not zero. In contrast to mosaics with no preferred orientation a facet exhibits a specific average orientation angle. This orientation angle corresponds to a specific crystal plane that can be characterized by the Miller indices $(hkl)$. A visualization of facets formed at a (001) surface is given in Fig. 2.11.

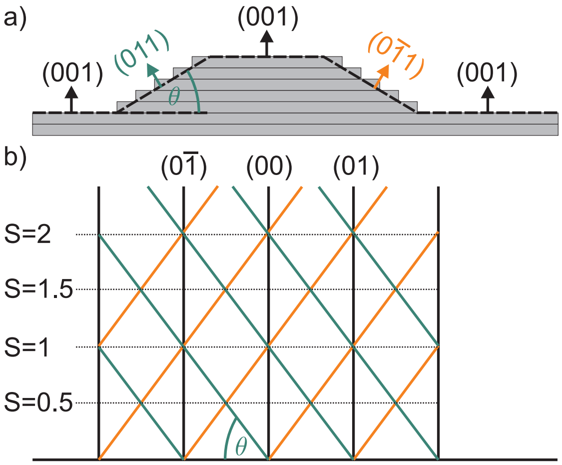

**Figure 2.11:** **a)** Illustration of two different kinds of facets formed on a (001) surface. The Miller indices correspond to the average inclination angle $\theta$. **b)** Tilted diffraction rods resulting from the facets. The inclination angle $\theta$ for the (011) facet corresponds to the tilt angle of the diffraction rods caused by this facet.

One can see that the diffraction rods caused by facets are tilted while the tilt angle corresponds to the average orientation angle of the facet. Therefore, during a diffraction experiment the diffraction spots show *satellites* that move through reciprocal space with increasing scattering phase. These satellites are in fact the diffraction spots coming from the diffraction rods caused by the facets. Since the step height on a facet is the same as on the primal surface the scattering conditions are also the same. Hence, during an in-phase condition the satellites disappear because the tilted diffraction rods intersect with the diffraction rods from the primal surface. On the other hand, during an out-of-phase condition the satellites (due to one facet) are equally separated from the central spot (cf. Fig. 2.11). Fig. 2.12 shows three examples of typical spot profiles obtained at different scattering conditions from a surface with facets.

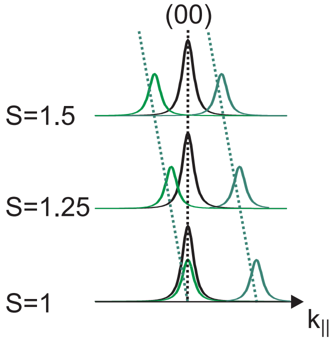

**Figure 2.12:** Typical diffraction spot profiles obtained from a (001) surface with one kind of facet (no counter facet) and remaining (001) terraces (central spot). The tilted diffraction rods result in spots that change their position in reciprocal space ($k_\perp$) with increasing scattering phase $S$. These moving diffraction spots are called *satellites*.

### 2.2.6 Superstructures and undulations

As explained in Chap. 2.1.2 a surface can exhibit different kinds of superstructures for energetic reasons or due to adsorption of foreign atoms. These superstructures lead to a change in the lateral periodicity in comparison to the unreconstructed surface (cf. Fig. 2.2). Thus, additional spots occur in the diffraction pattern that correspond to the lateral periodicity of the reconstruction.

Assuming an unreconstructed square surface unit cell with lattice vector $\vec{a}$ the reciprocal surface lattice vector is $|\vec{a}^*| = 2\pi/|\vec{a}|$. The shown $(2 \times 1)$ superstructure in Fig. 2.2 results in an unchanged surface lattice vector $|\vec{b'}| = |\vec{b}|$ and a twice as long lattice vector $|\vec{a'}| = 2|\vec{a}|$ compared to the lattice vectors of the unreconstructed surface. Therefore, the length of the reciprocal surface lattice vectors resulting from this $(2 \times 1)$ superstructure are

$$|\vec{a'}^*| = \frac{2\pi}{2|\vec{a}|} \ , \ |\vec{b'}^*| = \frac{2\pi}{|\vec{b}|} \ . \qquad 2.44$$

A schematic diffraction pattern and corresponding diffraction rods resulting from a square $(1 \times 1)$ (001) surface with a $(2 \times 1)$ superstructure (corresponding to Fig. 2.2) is shown in Fig. 2.13 for illustration.

In contrast to the diffraction rods generated by facets, the diffraction rods from a superstructure are not tilted since the the surface normal is not tilted within the formation of a superstructure. Therefore, the diffraction spots of the superstructure do not change their lateral position in reciprocal space. Nevertheless, the FWHM of the superstructure spots can differ from the FWHM of the spots caused by the fundamental surface unit cell. Comparable to terrace widths on an unreconstructed surface, the FWHM of the superstructure spots gives information about the domain sizes L of the superstructure areas at the surface. Fig. 2.14 illustrates the influence of domain sizes on the FWHM of the diffraction spots coming from a $(2 \times 1)$ superstructure on a (001) surface.

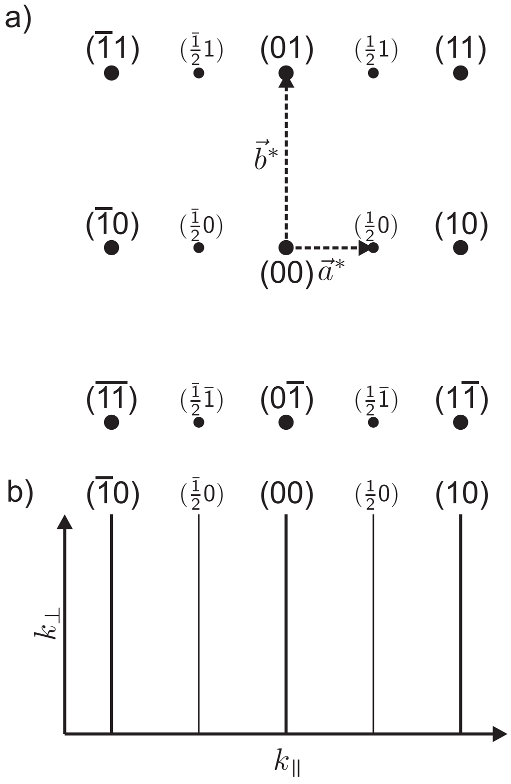

**Figure 2.13: a)** Schematic drawing of a diffraction pattern corresponding to a square (001) $(1 \times 1)$ surface with a $(2 \times 1)$ superstructure. Superstructure spots are indicated by smaller dots. The reciprocal lattice vectors of the superstructure are marked by dashed arrows. **b)** Diffraction rods corresponding to the $(2 \times 1)$ superstructure.

A similar diffraction pattern can be induced by undulations at the surface. Such undulations can for example be formed due to strain reduction between the substrate and a poorly matched film. As mentioned in Chap. 1 the thin iron oxide films investigated within this work tend to form undulations on different metallic substrates [27, 28]. Thus, it is necessary to shed some light on the characteristics of the diffraction pattern caused by an undulation.

First, the FWHM of the diffraction spots caused by an undulation does not increase linear with increasing scattering phase $S$ as it does for mosaics without preferred orientation. This might be surprising on first sight, since the surface normals at different points on an undulation also point into various directions. Therefore, the angular distribution of the surface normals on an undulation would look similar to the distribution caused by mosaics without preferred orientation (cf. Fig. 2.9). Nevertheless, the important difference is the continuous change of direction of the surface normals of an undulation. For visualization a schematic drawing of an undulation and the resulting surface normals is given in Fig. 2.15.

This continuous change in orientation retards the neighbored diffracted electrons to interfere almost constructively and contribute intensity to the diffraction pattern. However, an undulation has a certain periodicity that is caused by the interactions between film and substrate (lattice misfit, dislocations, ...). This periodicity makes the undulation act as a phase grating for the incoming electrons. Hence, additional diffraction spots with the

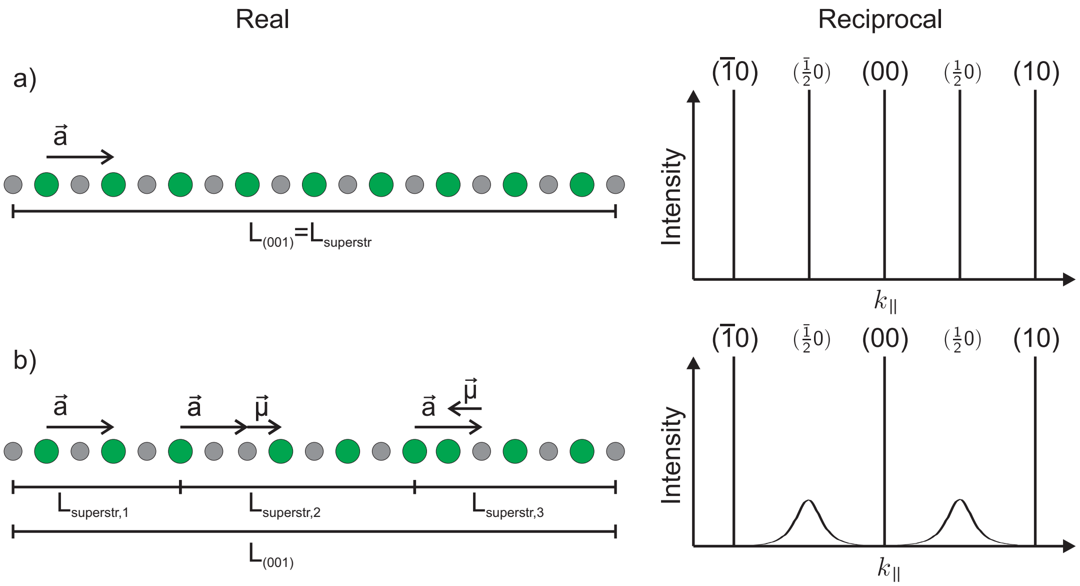

**Figure 2.14:** Side view of $(2 \times 1)$ superstructures on a (001) surface and cutouts of the resulting diffraction pattern. **a)** Diffraction spots from the superstructure are not broadened compared to the fundamental substrate spots, since the domain size L of the superstructure areas equals the domain size of the substrate (spots are $\delta$-peaks for a perfectly ordered superstructure). $\vec{a}$ is the translation vector of the superstructure. **b)** Smaller superstructure domain sizes and resulting broadening of the corresponding diffraction spots. The additional translation vector $\vec{\mu}$ marks the formation of anti-phase domains.

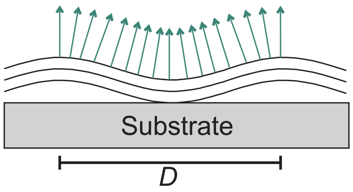

**Figure 2.15:** Schematic drawing of an undulated film on top of a substrate. The resulting surface normals are represented by green arrows. $D$ marks the periodicity of the undulation.

reciprocal distance $\Delta k_{||} = 2\pi/D$ appear in the diffraction pattern. Here $D$ is the periodicity length of the undulation. Since the undulation is usually caused by film-substrate interactions it has specific lateral orientations and periodicities that are influenced by the substrate as well as films symmetries. For example a film with a square surface unit cell could exhibit undulations in two perpendicular directions on a square substrate surface due to symmetrical reasons. (cf. Fig. 2.16).

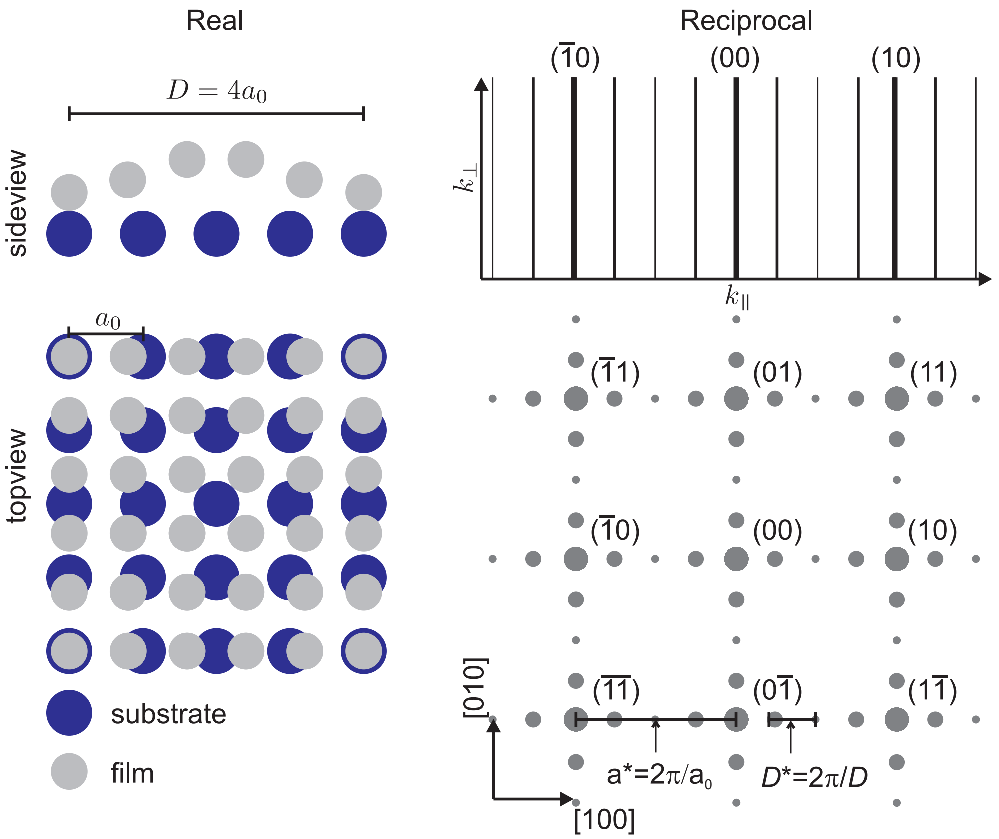

**Figure 2.16: left:** Schematic drawing of a square film that exhibits an undulation in two directions on a surface with square surface unit cell. The periodicity of the undulation is $D = 4a_0$. **right:** Diffraction pattern corresponding to the undulated film on the left side. The reciprocal distance between the additional diffraction spots is $D^* = 2\pi/D$. The smaller getting dots stand for an increasing FWHM of the diffraction spots with increasing distance from a primal substrate diffraction spot. Some diffraction spots between the fundamental spots are left out for clarity.

It is indicated in Fig. 2.16, that the FWHM of the diffraction spots increases with increasing distance from the primal substrate diffraction spots. The FWHM of the diffraction spots increases more drastically the less the undulation is ordered (variation in periodicity). On the other hand, a perfectly ordered undulation would exhibit $\delta$-shaped diffraction spots. Fig. 2.17 shows the influence of the order of the undulation on the corresponding diffraction spots.

For a not perfectly ordered undulation the FWHM of the corresponding diffraction spots increases quadratically with the order of the spots (FWHM $\propto n^2$) [49, 50]. As mentioned before, similar to the diffraction spots caused by a superstructure the spots coming from an undulation do not change their lateral position in reciprocal space with increasing scattering phase. Hence, an undulation can be seen as a special kind of superstructure (cf.

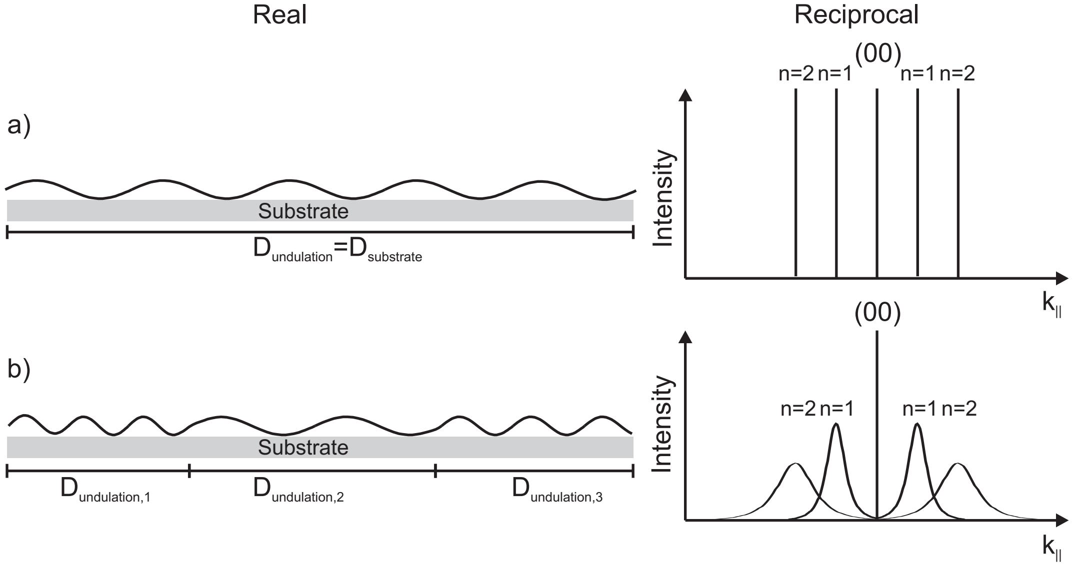

**Figure 2.17:** Side view of an undulated surface and outcuts of the resulting diffraction pattern. **a)** Diffraction spots from the undulation have the same FWHM (here $\delta$-peaks for a perfectly ordered undulation), since the domain size of the undulation equals the domain size of the substrate. **b)** Smaller undulation domain sizes and increasing FWHM of the corresponding diffraction spots with increasing order n.

Fig. 2.16, left side).

Since the undulated iron oxide films observed in this work will also be quantitatively analyzed via electron diffraction, the corresponding theoretical background will be introduced in the following.

### 2.2.7 G(S) analysis

A one dimensional, perfectly ordered undulation of a thin film can approximately be described by the oscillation $h(\mathrm{x}) = h_0 \sin\left(\frac{\mathrm{x}}{D}\right)$ where $D$ is the periodicity length of the undulation (cf. Fig. 2.18).

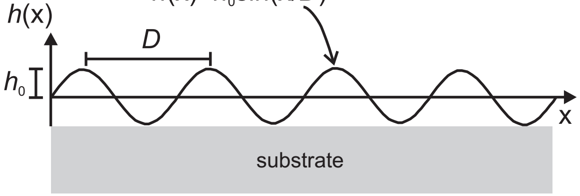

**Figure 2.18:** One dimensional undulation of a film that can be described by the oscillation $h(\mathrm{x}) = h_0 \sin\left(\frac{\mathrm{x}}{D}\right)$.

The root mean square (rms)-roughness $\omega_0^2$ of the undulation results in $\omega_0^2 = \overline{h^2} - \overline{h}^2$, while $\overline{h}^2 = 0$ for an oscillation around zero. In this case it also follows $\overline{h^2} = \frac{h_0^2}{2}$ and, therefore,

$\omega_0 = \frac{h_0}{\sqrt{2}}$.

For thin Ge films on Si(111) and Ag films on Si(001) it has already been reported that electron diffraction can also give information about the height of such undulations [49, 50]. This can be done by analysis of the behavior of the integrated satellite spot intensities from one fundamental diffraction spot, with increasing $\mathrm{k}_\perp$ (G(S) analysis). In general, the behavior of the integrated intensities is described by quadratic BESSEL functions $J_n(x)^2$, where $n$ is the order of the corresponding satellite. But in a first approximation the satellite intensities show a quadratic behavior in $k_\perp$ for very low electron energies [49]. For higher electron energies (depending on the rms-roughness of the undulation) the intensities of the satellite spots follow GAUSSIAN distributions in $k_\perp$. In this case the intensity of the central spot decreases via

$$I_0 = \mathrm{e}^{-\omega_0^2 k_\perp^2} \ . \tag{2.45}$$

This relative integrated intensity is calculated with respect to the integrated intensity of the whole diffraction spot. An increasing GAUSSIAN distribution, on the other hand, describes the behavior of the intensities of the satellite spots as

$$I_n = 1 - \mathrm{e}^{-\omega_n^2 k_\perp^2} \ , \tag{2.46}$$

where $n > 0$ is again the order of the regarding satellite spot.

Furthermore, the sum of the relative integrated intensities of all spots has to be 1. This leads to a dependency between the parameters $\omega_n$. In the case of five satellite spots (central spot, first and second order satellites), this leads to

$$1 = \mathrm{e}^{-\omega_0^2 k_\perp^2} + 1 - \mathrm{e}^{-\omega_1^2 k_\perp^2} + 1 - \mathrm{e}^{-\omega_2^2 k_\perp^2} \tag{2.47}$$

$$1 = -\mathrm{e}^{-\omega_0^2 k_\perp^2} + \mathrm{e}^{-\omega_1^2 k_\perp^2} + \mathrm{e}^{-\omega_2^2 k_\perp^2} \ . \tag{2.48}$$

For low electron energies (small values of $k_\perp$) the exponential functions from Eq. 2.48 can be written as TAYLOR series development around $\omega_n^2 k_\perp^2 = 0$ via

$$\mathrm{e}^{-\omega_n^2 k_\perp^2} = \sum_{\mathrm{m}=0}^{\infty} \frac{(-\omega_n^2 k_\perp^2)^{\mathrm{m}}}{\mathrm{m}!} \ . \tag{2.49}$$

For small values of $k_\perp$ and since $\omega_n < 1$ for all undulations with a height of $\Delta h < 2.8\,\text{Å}$ (from $\omega_0 = \frac{\Delta h}{2\sqrt{2}}$) follows $\omega_n^2 k_\perp^2 < 1$. In that case an expansion of the TAYLOR series up to the first order already results in a very small discrepancy and is, therefore, a sufficient approximation. We obtain

$$e^{-\omega_n^2 k_\perp^2} = \sum_{m=0}^{1} \frac{(-\omega_n^2 k_\perp^2)^m}{m!} = 1 - \omega_n^2 k_\perp^2 \ . \qquad 2.50$$

The GAUSSIAN behavior of the integrated spot intensities plotted against $k_\perp$ using the first order TAYLOR series approximation is presented in Fig. 2.19 b) for satellites up to second order. Since the GAUSSIANS can only serve as approximations of BESSEL functions for low electron energies, the corresponding BESSEL functions are also given in Fig. 2.19 a) for comparison.

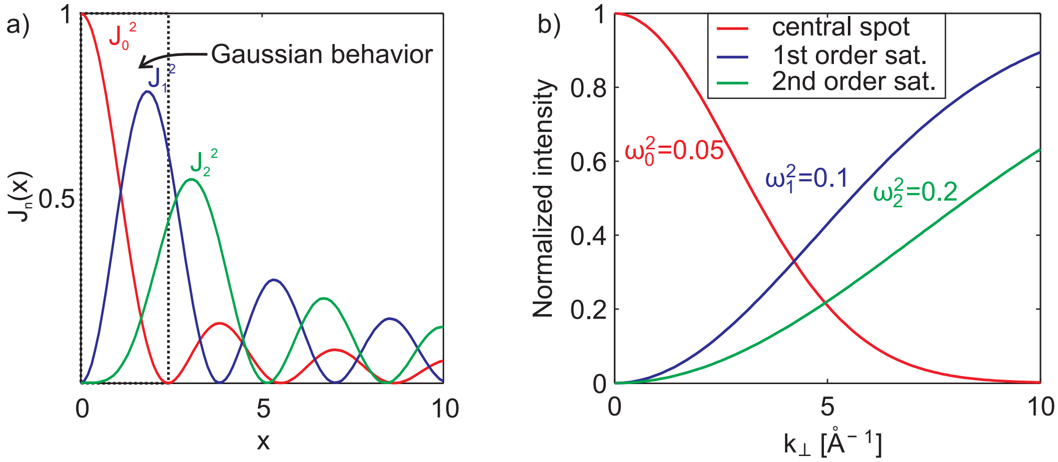

**Figure 2.19:** **a)** quadratic BESSEL functions describing typical satellite intensity behaviors for a long range of electron energies (represented by x values). **b)** Typical GAUSSIAN behavior of the normalized spot intensities plotted against $k_\perp$ using the first order TAYLOR series approximation for satellites up to second order for small values of $k_\perp$. This approximation is valid for the region marked in a). The $\omega_n$ fulfill the condition 2.53.

Using the TAYLOR series approximation up to first order one can determine a simple relation between the $\omega_n$ (satellites up to 2nd order). It is

$$1 = -1 + \omega_0^2 k_\perp^2 + 1 - \omega_1^2 k_\perp^2 + 1 - \omega_2^2 k_\perp^2 \qquad 2.51$$

$$0 = \omega_0^2 k_\perp^2 - \omega_1^2 k_\perp^2 - \omega_2^2 k_\perp^2 \ . \qquad 2.52$$

For $k_\perp \neq 0$ follows

$$\omega_0^2 = \omega_1^2 + \omega_2^2 \ . \qquad 2.53$$

Relation 2.53 can be used as a condition for the description of the intensity development of the satellite spots in $k_\perp$ for low electron energies.

Since our diffraction experiments were performed at electron energies around 100 eV and, therefore, $\omega_n^2 k_\perp^2 \approx 1$, the TAYLOR series needs to be expanded to higher orders to minimize the difference to the exponential function. In our case ($\omega_i^2 k_\perp^2 \approx 1$) an expansion of Eq.(2.50) up to third order produced sufficient results (cf. Fig. 2.20).

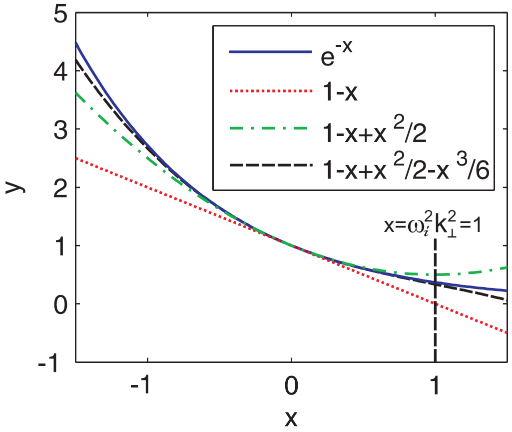

**Figure 2.20:** Development of the exponential function in comparison to the expansion of its TAYLOR series up to different orders. The discrepancy between $y = e^{-x}$ and $y = 1 - x + \frac{x^2}{2} - \frac{x^3}{6}$ is acceptably small for $x \approx 1$.

The relation between the $\omega_i$ is much more complicated in this case but can still be analytically resolved from

$$\begin{array}{ll} 1 =- & 1 + \omega_0^2 k_\perp^2 - \frac{\omega_0^4 k_\perp^4}{2} + \frac{\omega_0^6 k_\perp^6}{6} \\ + & 1 - \omega_1^2 k_\perp^2 + \frac{\omega_1^4 k_\perp^4}{2} - \frac{\omega_1^6 k_\perp^6}{6} \\ + & 1 - \omega_2^2 k_\perp^2 + \frac{\omega_2^4 k_\perp^4}{2} - \frac{\omega_2^6 k_\perp^6}{6} \end{array} \qquad 2.54$$

Hence, we used GAUSSIAN distributions to describe the behavior of the satellite intensities. The relation between the $\omega_i$ solved from Eq. 2.54 can be used as a fitting condition for the development of the relative integrated intensities of the satellite spots with increasing electron energies.

## 2.3 X-ray Photoelectron Spectroscopy

A relevant technique for the analysis of the chemical composition and the electronic structure of surfaces is **X**-ray **P**hotoelectron **S**pectroscopy (XPS). The following chapter sheds some light on this method and its theoretical basics.

### 2.3.1 The photoelectrical effect

XPS is based on the photoelectrical effect which was discovered in 1887 by H. HERTZ [51]. He found out that an electrostatically charged metal plate discharges faster if it is irradiated by light. In the following years W. HALLWACHS discovered that the discharging is an emission of electrons from the material if it is exposed to radiation above a threshold frequency [52]. The theoretical background for the understanding of this process was formed when A. EINSTEIN published his hypothesis about the quantification of electromagnetic radiation in 1905 [53].

In an XPS experiment a sample surface is illuminated with X-rays from an X-ray tube. The absorption of X-rays causes an emission of electrons from the surface atoms since, for X-rays, the absorbed energy is higher than the work function $\phi_{\mathrm{w}}$ of the emitting material. The electrons emitted from an atom inside the material have a mean free path of about 10Å in matter, what makes XPS a very surface sensitive method. For monochromatic X-rays the kinetic energy of the emitted electrons coming from the FERMI level of the illuminated material results in

$$E_{\mathrm{kin}} = h\nu - \phi_{\mathrm{w}} \; . \tag{2.55}$$

Here, $h$ is PLANCK'S constant and $\nu$ is the frequency of the incident X-rays. For electrons coming from an orbital that is closer to the nucleus Eq. 2.55 needs to be adapted considering the effective binding energy $E_{\mathrm{B}}$ of the electrons. This effective binding energy is the energy that is needed to excite an electron onto the FERMI level. Hence, Eq. 2.55 has to be written as

$$E_{\mathrm{kin}} = h\nu - \phi_{\mathrm{w}} - E_{\mathrm{B}} \; . \tag{2.56}$$

The effective binding energy $E_{\mathrm{B}}$ is characteristic for the different energy levels of different elements and is, therefore, used to identify different elements on the sample surface. In an XPS experiment the detector also has a certain work function $\phi_{\mathrm{spec}}$ that has to be regarded for the calculation of $E_{\mathrm{B}}$. Fig. 2.21 illustrates the involved energy levels of an XPS experiment on atomic magnesium.

With this the effective binding energy of an electron can be calculated from the measured kinetic energy of the electrons and Eq. 2.56 via

$$E'_{\mathrm{kin}} = E_{\mathrm{kin}} - (\phi_{\mathrm{spec}} - \phi_{\mathrm{w}}) \tag{2.57}$$

$$\Leftrightarrow E'_{\mathrm{kin}} = h\nu - \phi_{\mathrm{spec}} - E_{\mathrm{B}} \; . \tag{2.58}$$

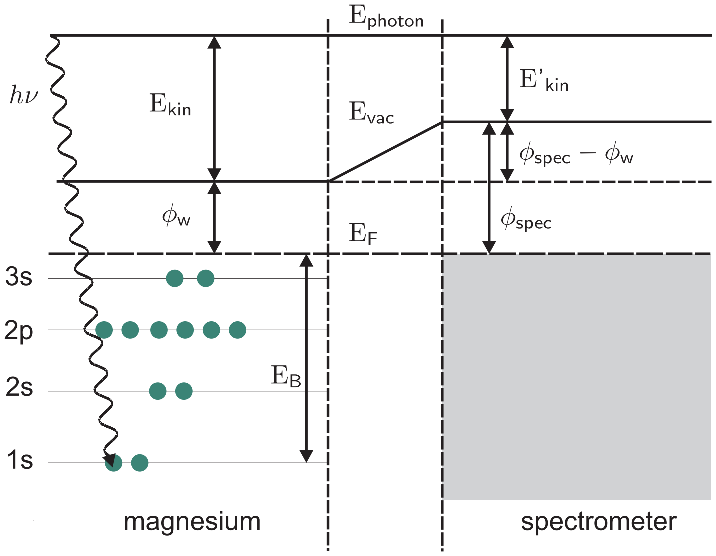

**Figure 2.21:** Schematic drawing of the energy levels involved in an XPS experiment on atomic magnesium. The incident photon has the energy $h\nu$ and excites an electron from the 1s level. The electrons have the kinetic energy $E_{\text{kin}}$ in the vacuum and reach the detector. The detected kinetic energy $E'_{\text{kin}}$ is reduced by the work function of the detector $\phi_{\text{spec}}$.

### 2.3.2 Photoemisson spectra

Shape and position of the photo emission peaks can be influenced by a number of different effects during an XPS experiment. The two most important effects that are necessary to interpret the results presented in this work will be briefly introduced below.

#### Chemical shift

The effective binding energy of an electron can be influenced by the chemical surrounding of the corresponding atom. Ionic or covalent bondings between neighbored atoms lead to a change in the effective binding energy of the electrons and, therefore, to a shift of the photoemission peaks compared to unbound atoms. A sufficient theoretical approach to describe such shifts is given by the *charge potential model*. Here, it is assumed that the additional potential formed by the chemical bonds of the valence electrons is the significant influence of the effective binding energy of the remaining electrons of the atom. The resulting effective binding energy can therefore be calculated by

$$E_{\text{B,eff}} = E_{\text{B}} + E_{\text{chem}} + E_{\text{Mad}} \ , \qquad 2.59$$

where $E_{\text{chem}}$ is the mentioned chemical potential formed by the bonding valence electrons and $E_{\text{Mad}}$ is the MADELUNG term summing up the potentials of the surrounding atoms. In practice, reference spectra from known compositions are taken from literature and compared to the measured spectra [54].

For illustration the well known example of the 1s signal of carbon in ethyl trifluoroacetate is shown in Fig. 2.22.

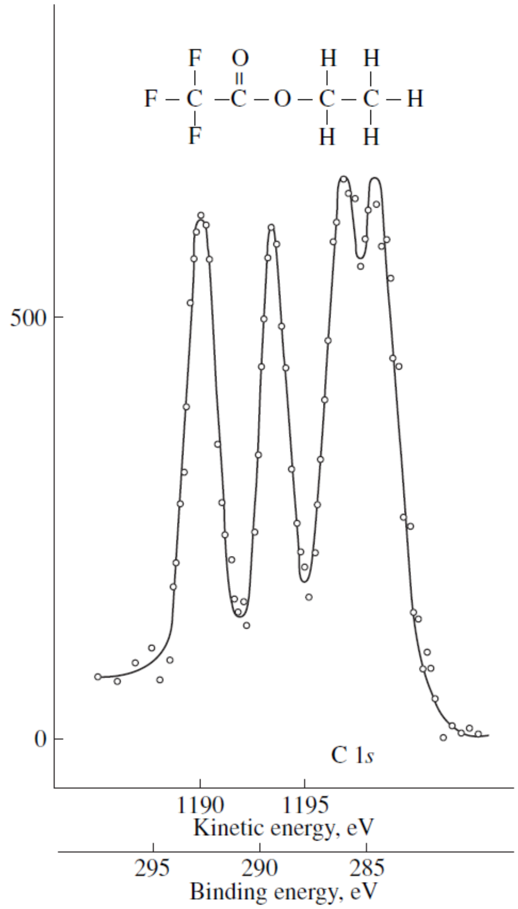

**Figure 2.22:** Chemical shift of the 1s signal of different bound carbon atoms in ethyl trifluoroacetate. Image is taken from Ref. [55].

### Charge transfer satellites

The photo emission spectra of transition metal oxides reveal additional satellites beneath the photo emission peaks of the metal due to a charge transfer between different orbitals. In FeO an electron from the 2p orbital of the oxygen can transfer to the 3d orbital of the iron. In this case the binding energy of this electron is reduced by

$$\Delta E = E(3d^{n+1}L^{-1}) - E(3d^{n}L) \ . \qquad 2.60$$

Here, $L$ denotes the regarding oxygen ligand, which transfers an electron to the $3d^n$ orbital of Fe. Hence, the satellites due to charge transfer are always shifted to lower energies. Fig. 2.23 shows a measured spectrum of the Fe2p signal from FeO taken from Ref. [56]. The charge transfer satellites are marked by arrows.

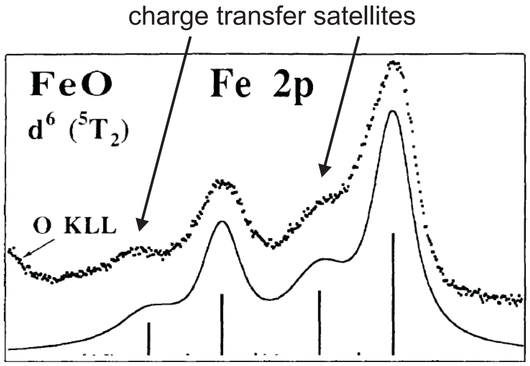

**Figure 2.23:** Fe2p signal from FeO showing the characteristic charge transfer satellites at lower energies. Image is taken and modified from Ref. [56].

## 2.4 AUGER Electron Spectroscopy

Another common method to analyze the chemical composition of surfaces is the AUGER electron spectroscopy. The hereby harnessed AUGER effect was discovered by the French physicist P. V. AUGER in 1926 during investigations on the impact of X-Rays on solids [57].

### The AUGER effect

Fig. 2.24 illustrates the atomic AUGER effect for a so-called $KL_1L_{2,3}$ transition.

In the example from Fig. 2.24 the atom gets hit by a particle with sufficiently high energy (photons, electrons, ...) and an electron from the $K$ shell is emitted from the atom. Then, an electron from the $L$ shell recombines with the generated hole in the $K$ shell. The spare potential difference can either be released by the emission of a X-ray photon (X-ray fluorescence) or by emission of an AUGER electron. X-ray fluorescence mainly takes place for heavy elements, while AUGER electrons are primarily emitted from atoms with lower atomic number (typical range is $Z < 80$ [59]). The AUGER electron is then emitted from the $L$ shell. However, AUGER spectroscopy usually is used for investigations concerning solids. Hence, the band structure for a solid has also be taken into account. In this case the valence band contains delocalized electrons with varying energy according to the band width. Therefore, the AUGER electrons can be emitted from the valence band which makes a correction for the calculation of their kinetic energy in comparison to the isolated atom model (cf. Fig. 2.24) necessary [60]. The corrected kinetic energy of an $KLL$-AUGER electron is then given as

$$E_{KL_1L_{2,3}} = E_K - E_{L_1} - E_{L_{2,3}} - \Delta E_{L_1L_{2,3}} - \phi_w \ , \qquad 2.61$$

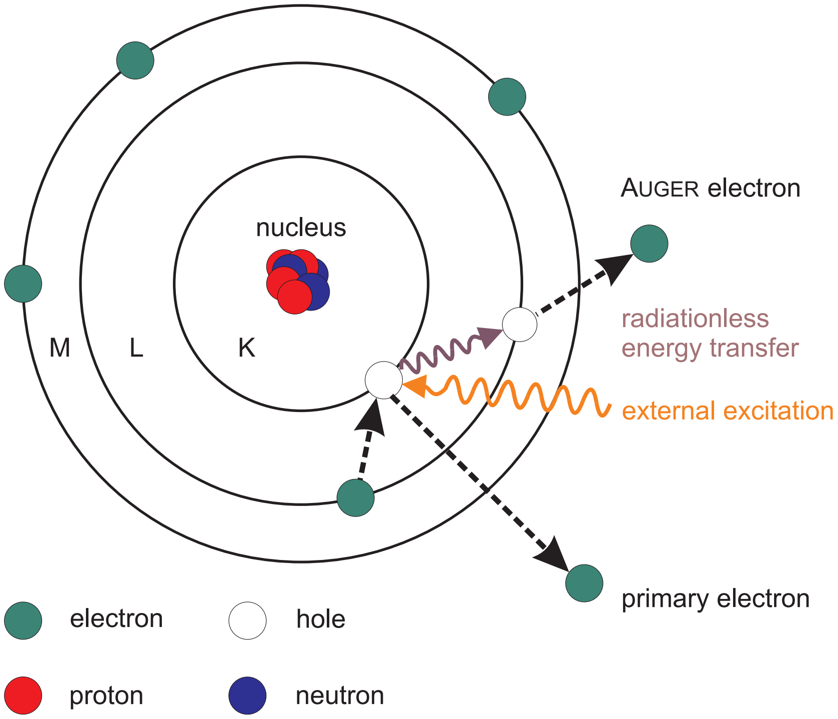

**Figure 2.24:** Schematic drawing of the Auger process for a $KL_1L_{2,3} \equiv KLL$ transition. Graphic is taken and adapted from Ref. [58].

with $\phi_w$ as the work function of the investigated material (energy difference between Fermi level and vacuum). It can be concluded from Eq. 2.61 that the kinetic energy of the Auger electrons does not depend on the energy of the incident particle as long as it is sufficient to excite core level electrons. The mean free path of the Auger electrons (which is determined by their kinetic energy) equals the depth from where the Auger electrons can come from. An experimentally obtained curve showing the mean free path of electrons in dependence of their kinetic energy in different materials is shown in Fig. 2.25

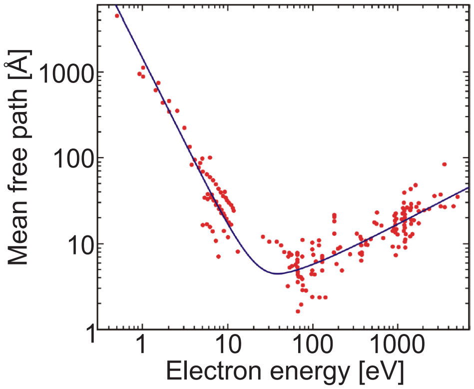

**Figure 2.25:** Experimentally obtained curve of the mean free path of electrons in dependence of their kinetic energy in different materials. Image is taken from Ref. [61] and modified.

One can see that the mean free path of AUGER electrons is about 10Å since their kinetic energy is in the range of $10 - 2000$ eV. This makes the technique very surface sensitive.

An exemplary AUGER spectrum of a cleaned Ag surface is shown in Fig. 2.26. The Ag($MNN$) transition at 351 eV is marked by a dashed line.

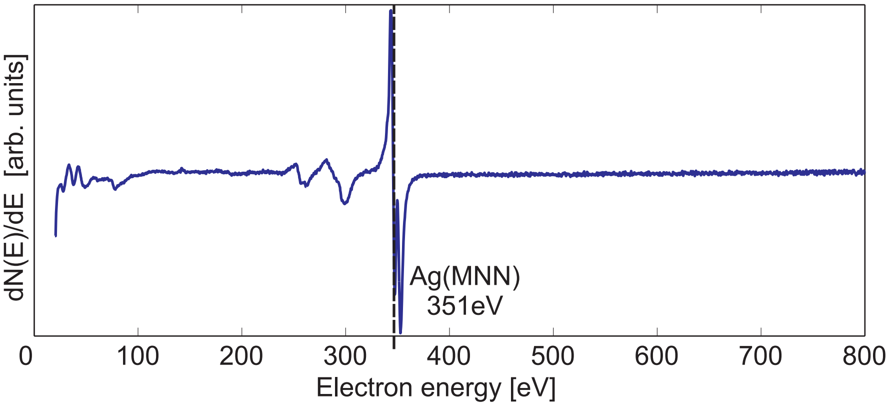

**Figure 2.26:** Exemplary AUGER spectrum of a cleaned Ag substrate. The Ag($MNN$) transition at 351 eV is marked by a dashed line. Graphic is taken and adapted from [44].

It has to be noted, that the shown spectrum is derived from the raw data via dN(E)/dE. This is the common type of presentation since the relatively small AUGER signals are superposed by a high background that increases with the electron energy due to secondary electrons that undergo multiple losses of energy [42].

## 2.5 Quantitative XPS and AUGER analysis

With both X-ray photoelectron and AUGER electron spectroscopy it is possible to get quantitative information about the chemical composition of a surface or thin film. Since determination of such information is quite similar for both techniques, the mathematical description will be wrapped up in the following section.

To obtain quantitative information from XPS, the areas underneath the peaks are calculated and weighted by sensitivity factors for the specific elements. It has to be noted that a background is subtracted from the data prior to the calculation of the areas under the peaks. In this work the well known SHIRLEY background was used (cf. Ref. [62]).

An example for the calculated area under a Ag3d photoemission peak is given in Fig. 2.27 for illustration.

Assuming a homogeneous sample and a constant photon flux as well as a fixed experimental geometry the number of photo electrons per second (intensity) in a peak can be determined by

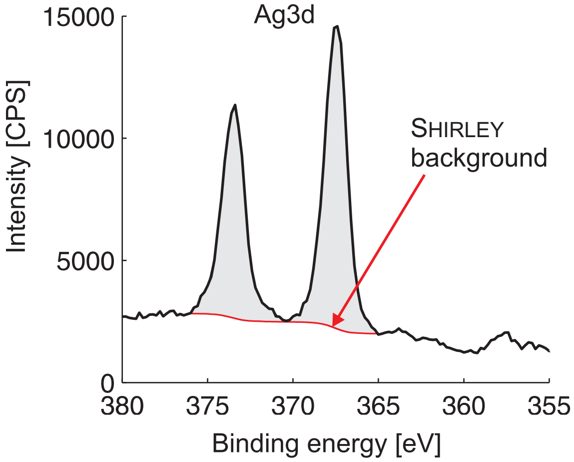

**Figure 2.27:** Calculated area under a Ag3d photoemission peak. The subtracted SHIRLEY background is indicated by a red line.

$$I = \sigma \cdot K \cdot N \cdot A \cdot T \cdot \lambda \ , \qquad 2.62$$

where $\sigma$ is the photoionisation cross section of the element, $K = \text{const}$, $N$ is the number of atoms of the specific element per $\text{cm}^3$ (atomic density), $A$ is the area of the sample from where those photoelectrons come from, $T$ is the transition function of the analyzer and $\lambda$ is the inelastic mean-free path of the photoelectrons in the concerning element [63].

Since, according to Ref. [64], the sensitivity factor for a specific element X can be defined as

$$S_\text{X} = \sigma \cdot K \cdot A \cdot T \cdot \lambda \ , \qquad 2.63$$

the number of atoms contributing photoelectrons to a specific peak results in

$$N_\text{X} = \frac{I_\text{X}}{S_\text{X}} \ . \qquad 2.64$$

Thus, the ratio $R$ between two different elements in the sample is given by

$$R = \frac{N_1}{N_2} = \frac{I_1 S_2}{I_2 S_1} \ . \qquad 2.65$$

Since the $N_X$ are atomic densities with $N_X = n_X/V_X$, the ratio $R$ can also be written as

$$R = \frac{N_1}{N_2} = \frac{n_1 V_2}{n_2 V_1} = \frac{n_1}{n_2} \ , \qquad 2.66$$

because $V_1 = V_2$. From Eq. 2.65 and 2.66 follows

$$\frac{I_1 S_2}{I_2 S_1} = \frac{n_1}{n_2} \ . \tag{2.67}$$

Similar to XPS it is possible to do a quantitative analysis of the chemical composition of the surface with AUGER electron spectroscopy by comparing the peak-to-peak intensities $I_X$ (not the areas underneath the peaks) of the different AUGER signals from the derived spectrum. Here, the sensitivities $S_X$ from XPS analysis are simply replaced by the sensitivities $\sigma_X$ for the different elements into the peak-to-peak ratio (cf. Fig. 2.28).

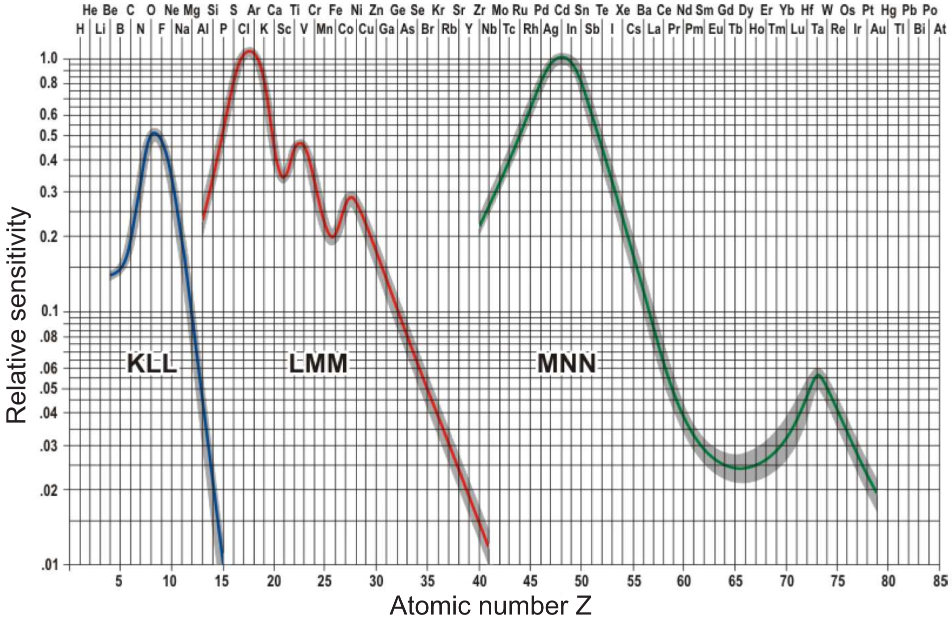

**Figure 2.28:** Relative AUGER sensitivities $\sigma_X$ of the different elements and transitions. Graphic is taken from Ref. [44] and adapted .

Thus, the ratio $R$ of two elements A and B at the surface is given by

$$R = \frac{I_{\mathrm{A}} \sigma_{\mathrm{B}}}{I_{\mathrm{B}} \sigma_{\mathrm{A}}} \ , \tag{2.68}$$

with $I_{\mathrm{A,B}}$ as the peak-to-peak intensities of the regarding AUGER transition from the derived spectrum. In this work, the quantitative XPS and AUGER analysis was mainly used to calculate coverages of deposited Fe or FeO films on the Ag surface. The theory for those calculations is rather complicated for the general case (discussed in [61] for quantitative AUGER analysis). Therefore, some assumptions have to be made in order to successfully apply the theory to the data. For a homogeneous film $F$ (e.g. growing in layer-by-layer mode) on the substrate S the normalized intensity ratio $I_{\mathrm{rel}}$ can be written according to Ref. [42] as

$$I_{\mathrm{rel}} = \frac{I_{\mathrm{F}}/\sigma_{\mathrm{F}}}{I_{\mathrm{S}}/\sigma_{\mathrm{S}} + I_{\mathrm{F}}/\sigma_{\mathrm{F}}} = 1 - e^{-D/\lambda_F} \ . \tag{2.69}$$

Here, $D$ is the film thickness, $\lambda_F \approx \lambda_S = \lambda$ is the mean free path of electrons in the material, which is approximately the same for the film and substrate (cf. Fig. 2.25), while $\sigma_S$ and $\sigma_F$ are the sensitivities of substrate and film, respectively (remember different sensitivities for AES and XPS). In the experiments performed during this work the mass equivalent evaporated onto the substrate is measured by an oscillating quartz. For a layer-by-layer growing film the thickness results in $D = c \cdot \Delta f$ where $\Delta f$ is the change in frequency of the oscillation quartz and $c = const.$ Thus, by measuring the (Auger or photoemission) intensities of film and substrate signals for different coverages $\Theta$ the unknown constant $c$ and, therefore, the absolute film thickness $D$ can be estimated using Eq. 2.69.

## 2.6 Scanning Tunneling Microscopy

The scanning tunneling microscopy (STM) was developed by G. Binnig, H. Rohrer, Ch. Gerber, and E. Weibel in 1982 and is, therefore, a very young surface analysis method [65]. It was the first method that was able to image surface topography and electronic structure on an atomic scale at the same time. G. Binnig and H. Rohrer were decorated with the Nobel price for their work in 1986.

This technique is based on the quantum mechanical tunneling effect. The position of an electron can not be determined exactly but is given by a detention feasibility $\rho(\vec{r})$. Therefore, an electron can tunnel from one state through a potential barrier into another unoccupied state with a certain probability. In an STM experiment the electrons tunnel from a state in a (very sharp) metal tip into an unoccupied state at the sample surface or vise versa. A potential difference between tip and sample leads to an increase of states that can contribute to the tunneling process (cf. Fig. 2.29).

According to Ref. [66] the tunneling current is decreasing exponentially with the distance between tip and sample via

$$J_T \propto \frac{V_T}{s} \cdot e^{-A\sqrt{\phi}s} \ , \tag{2.70}$$

with the applied potential difference $V_T$, the tip-surface distance $s$, the average work function of tip and sample $\phi$ and $A = 1.025\,(\sqrt{\mathrm{eV}}\mathrm{\AA})^{-1}$ denoting the vacuum gap.

Basically, there are two different modes to operate an STM namely *constant height* and *constant current* mode, while only the latter mode was used in this work. In the *constant*

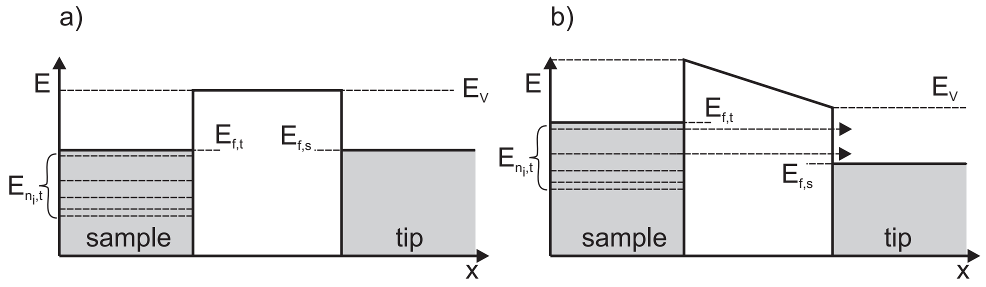

**Figure 2.29:** $E_{f,t}$ and $E_{f,s}$ denote the FERMI levels of tip and sample, respectively, while $E_V$ marks the potential barrier due to the vacuum. **a)** Situation without an applied potential difference. The probability of tunneling electrons is in this case negligible for all states $E_{n_i,t}$ in the sample. **b)** The applied potential difference leads to an increase of states $E_{n_i,t}$ that can contribute to the tunneling process.

*current* mode a feedback loop constantly monitors the tunneling current and makes position adjustments to the tip to maintain a constant tunneling current. Here, the distance between tip and surface is varied by a piezo and recorded as hight information. This mode is advantageous for investigations on rough surfaces since it prevents the tip from crashing into the sample surface.

The tunneling current does not only depend on the tip-surface distance but also on the different states that are involved in the tunneling process. Thus, one has to be carefully interpreting the STM topography images, since even surface atoms with the same distance to the tip can show a different contrast due to their different electronic states.

### 2.6.1 The one dimensional tunneling effect

The above mentioned tunneling effect shall now be considered in more detail since it is the main process involved in an STM experiment. For reasons of simplification we will only look at the one dimensional tunneling effect. Fig. 2.30 illustrates the one dimensional tunneling process for the case of an electron tunneling from a sample state into an unoccupied tip state.

In this example the FERMI energies of sample and tip are shifted due to an applied voltage. The wave function describing the tunneling electron is exponentially damped during tunneling through the potential barrier. If the one dimensional stationary SCHRÖDINGER equation is applied to the wave function describing the electron the transmission coefficient $T$ can be determined. $T$ is the ratio of the squared absolute values of the wave function before and after tunneling, respectively, and can according to Ref. [68] and Ref. [69] be approximated to

$$T(E,V_0,s) = \frac{16E(V_0-E)}{V_0^2} \cdot e^{-\frac{2}{\hbar}\sqrt{2m(V_0-E)}\cdot s} \;, \qquad 2.71$$

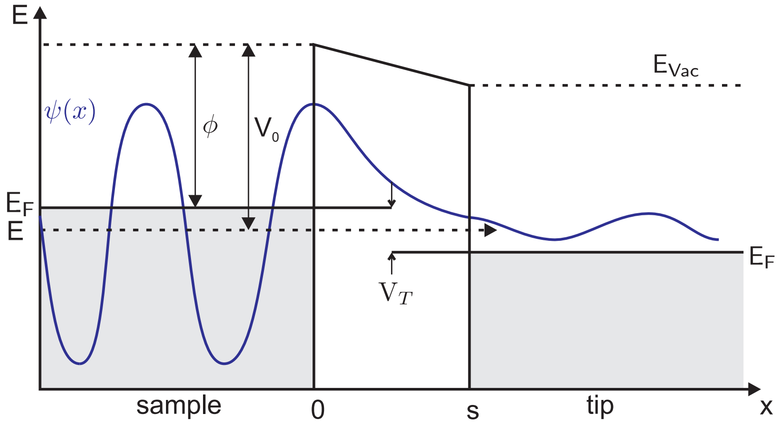

**Figure 2.30:** Schematic drawing of the one dimensional tunneling process of an electron represented by its wave function $\psi(x)$ from the sample into the tip. The FERMI energies ($E_F$) of sample and tip are shifted due to an applied voltage $V_T$. The work function of the sample is $\phi$. Image is taken from Ref. [67] and modified.

if the potential barrier is broad enough ($\sqrt{\frac{2m(V_0-E)}{\hbar^2}} \cdot s \gg 1$). Here, $E$ is the electron energy, $V_0$ is the height of the potential barrier, $s$ is the tip-surface distance and $m$ is the electron mass. It has to be noted, that the expression $\sqrt{2m(V_0-E)}$ is only real for $V_0 \geq E$. This is indeed the condition for the tunneling of electrons from the sample into the tip. For $V_0 < E$ parts of the potential barrier get classically available for the electrons. In this classically available region the electrons with the right wavelength can form standing waves what drastically increases the tunneling probability and, therefore, the measured current. This effect is known as *field emission resonance* and was discussed in former studies [70, 71]. Therefore, this case is not considered in the following (cf. Fig. 2.30).

From Eq. 2.71 follows that the tunneling current $J_T$ is proportional to

$$J_T \propto e^{-\frac{2}{\hbar}\sqrt{2m(V_0-E)} \cdot s} \,, \qquad 2.72$$

for the one dimensional approximation. Nevertheless, this model does not include influences from the three dimensional shape of surface and tip potential. An exact three dimensional description of the process, however, is very complex and goes beyond the scope of this work. Therefore, the widely used TERSOFF-HAMANN-approximation, which gives a sufficient description of the tunneling process in an STM experiment, will be discussed in the following.

### 2.6.2 TERSOFF-HARMANN-approximation

J. TERSOFF and D. R. HAMANN developed a description of the STM method in 1983 that is commonly used today [72]. It is based on the assumption that the local density of states

$\rho_T(E_F)$ is maximal at the top atom of the tip where the distance to the sample is the smallest. Only this top atom contributes to the tunneling process and its wave function is assumed to be spherical (s-wave funktion). The approximation uses the many-particle tunneling theory from BARDEEN [73]. GOTTLIEB at al. applied BARDEEN'S theory to scanning tunneling microscopy [74], where the tunneling current can be described via

$$J_T = \frac{4\pi e}{\hbar} \int_0^{eV_T} \rho_0(E_F - eV_T + \epsilon)\rho_T(E_F + \epsilon)|M|^2 d\epsilon \ , \tag{2.73}$$

with the density of states at the tip $\rho_T(E)$ and at the surface $\rho_0(E)$ and the applied voltage $V_T$. $|M|^2$ is the transition matrix which contains the wave functions of sample and tip (cf. Ref. [73]). With this formalism TERSOFF and HAMANN found that the tunneling current is only depending on the density of FERMI level states at the surface point that is closest to the tip with

$$J_T \propto V_T \rho_{\mathrm{surf}}(R, E_F) \ . \tag{2.74}$$

Here, $R$ is the position of the topmost atom at the tip over the sample surface, $E_F$ is the FERMI energy at the corresponding surface position and $V_T$ is the applied potential at the tip. Eq. 2.74 shows one more time that an STM image is not an actual topographic illustration of the sample surface but a mapping of the density of states.

### 2.6.3 Topographic height measurements in STM

Since we will also estimate topographic heights from our STM measurements, we would like to briefly address some non-topographic effects that can lead to a change in contrast during an STM measurement. Here, we present some STM measurements on reactively grown FeO films on Ag(001) as examples. These films, however, will be discussed in Chap. 5.5 in detail.

It is well known from literature, that different bias voltages can lead to a change in contrast in an STM image [75, 76, 77]. The reason for this is the increasing number of electronic states that can contribute to the tunneling process with increasing bias voltage (cf. Chap. 2.6). As shown in Fig. 2.31, we changed the bias voltage during one series of measurements to analyze the influence on the image contrast.

As predicted in other studies [75, 76, 77] a changing bias voltage leads to an inversion of contrast in our case. The FeO island in Fig. 2.31 a) seems to be lowered into the substrate, while the same island points out of the sample surface in Fig. 2.31 b).

This effect was already reported for the growth of NiO on Ag(001) by SEBASTIAN et al. [78] and can be illustrated by the model shown in Fig. 2.32.

Using low bias voltages only the electrons from the states of the Ag substrate can contribute to the tunneling process (cf. Fig. 2.32 a)). In the FeO islands on top of the Ag substrate

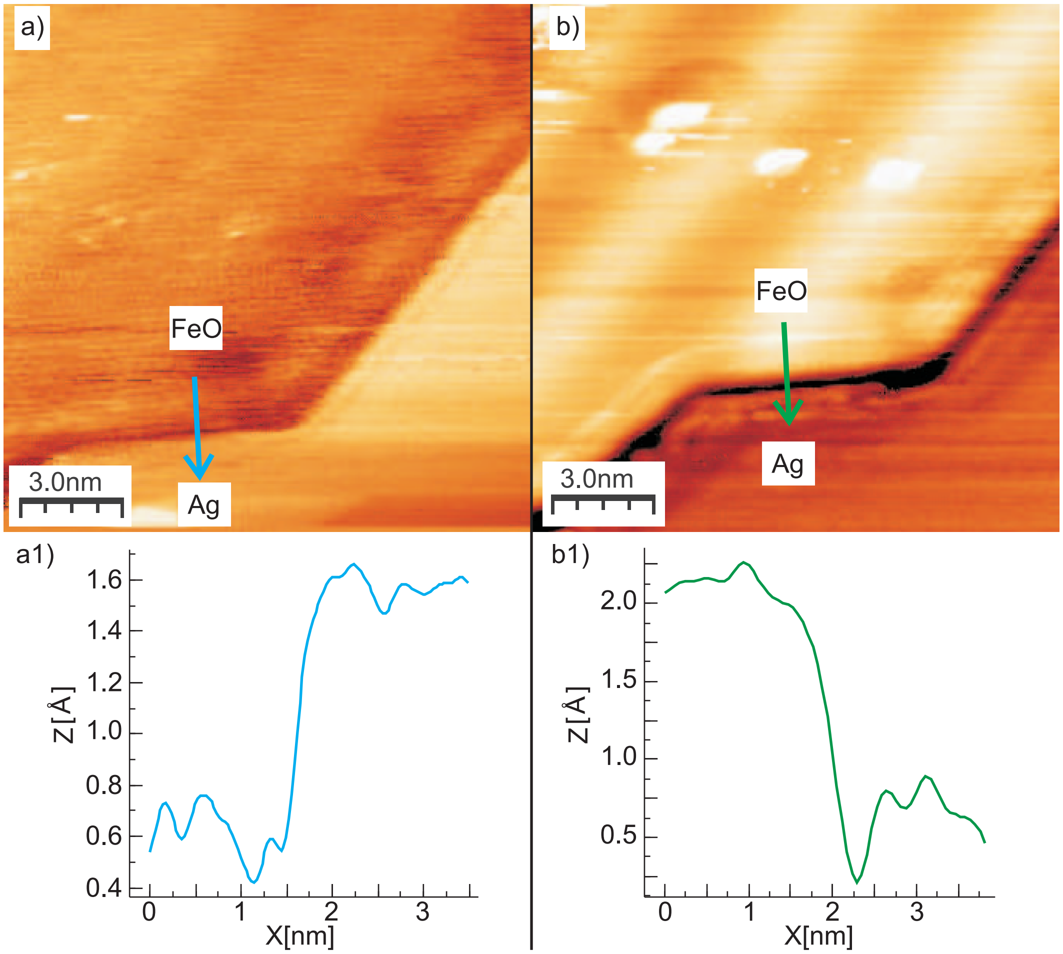

**Figure 2.31:** STM micrographs of a 0.5 ML FeO film (same region). Bias voltage is $U_{\mathrm{a}} = 480\,\mathrm{mV}$ for **a)** and $U_{\mathrm{b}} = 1200\,\mathrm{mV}$ for **b)**. The directions of the linescans in **a1)** and **b1)** correspond to the arrows in **a)** and **b)**.

the transmitting electrons can be scattered and the measured tunneling current is reduced. Since the STM is operated in constant current mode, this leads to an approach of the tip towards the sample surface over an FeO island. Thus, the FeO island seems to be lowered into the substrate (cf. Fig. 2.32 a1)). For higher bias voltages the electrons from the valence band of the FeO island can contribute to the tunneling process (cf. Fig. 2.32 b)). Thus, the FeO island points out of the substrate in the STM image (cf. Fig. 2.32 b1)) [78].

Furthermore, we observed a change in contrast by only varying the tunneling current $I_T$ which is presented in Fig. 2.33.

One can see, that a slight increase $I_T = 2\,\mathrm{nA}$ to $I_T = 2.3\,\mathrm{nA}$ in tunneling current already changes the contrast, and therefore, the obtained height information drastically. Since in the used constant current mode the tunneling current is a measure for the tip-surface

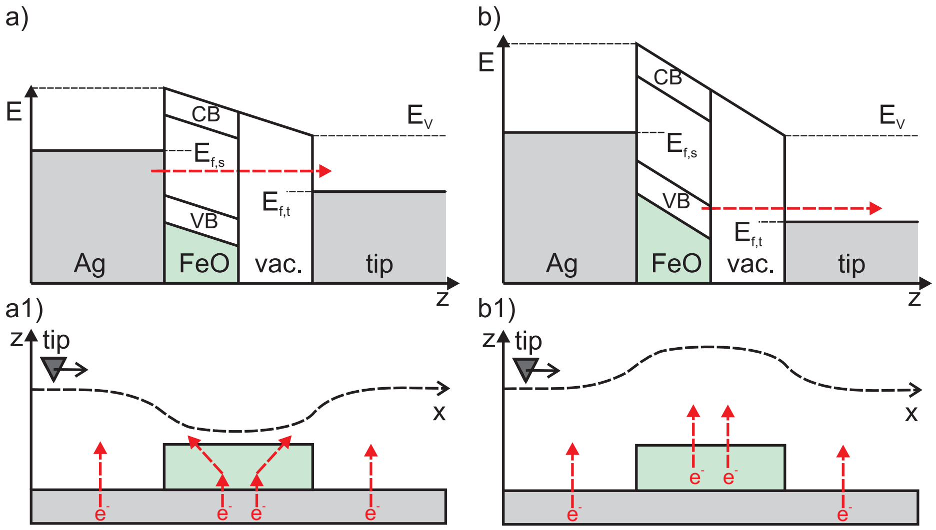

**Figure 2.32:** Illustration of the tunneling process from a Ag sample with an FeO film on top. CB and VB are the conducting band and the valence band of the FeO film, respectively. **a)** For low bias voltages only electrons from the states inside the Ag substrate can contribute to the tunneling process. **b)** For high bias voltages the electrons from valence band of the FeO film can contribute to the tunneling process. The resulting path of the tip for low and high bias voltage is shown in **a1)** and **b1)**, respectively

distance. With increasing tunneling current, the tip-surface distance decreases. This influences the tunneling probability for the contributing states (cf. Fig. 2.30).

Another effect can be seen in Fig. 2.34 a) where a few lines seem to be brighter (topographically higher) than the rest of the image (marked by blue arrow). This is caused by a too fast measurement (low step size and counting time) as illustrated in Fig. 2.34 b). Here, the STM tip is removed from the surface due to a strongly three dimensional structure. The feedback loop is not able to approach the tip back to the surface fast enough due to the high measuring speed. Therefore, the average height of this line appears higher than for other lines.

Thus, it has to be kept in mind that height information obtained from an STM measurement has to be taken carefully. Certain values need to be verified by another experimental method which is not sensitive to the electronic structure of the FeO film but to the position of the atoms nuclei.

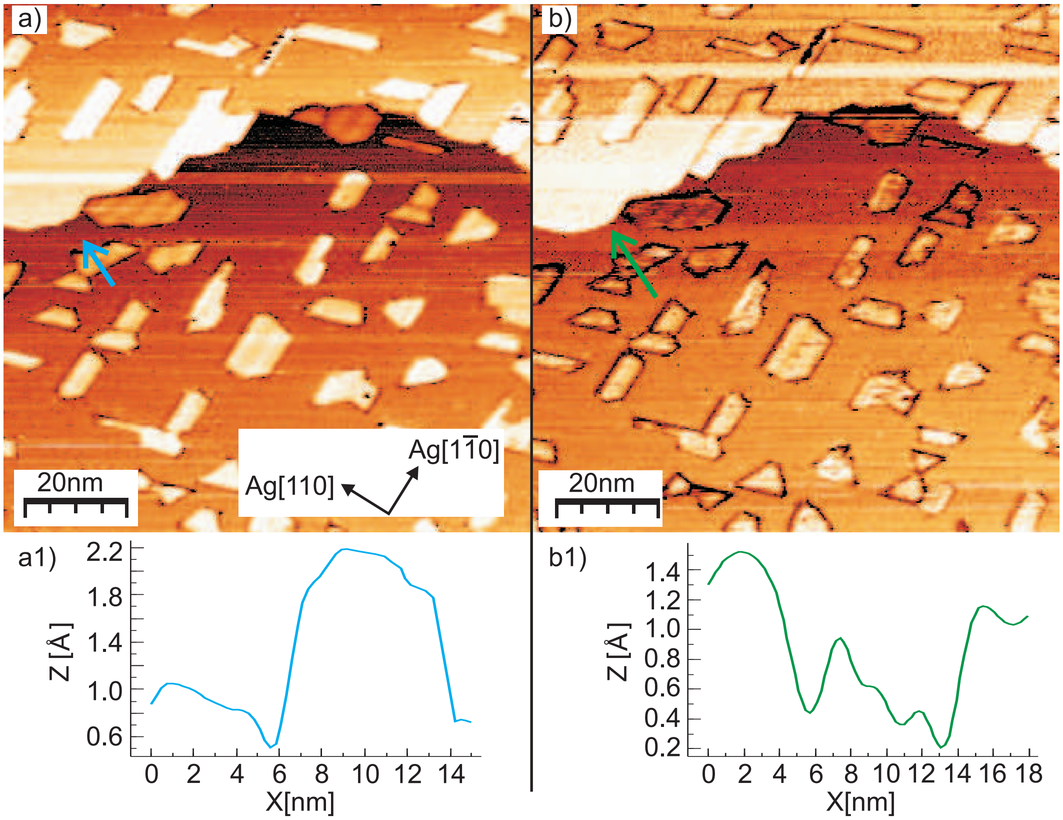

**Figure 2.33:** STM micrographs of the 0.25 ML FeO film at $U_a = 805\,\text{mV}$ tip bias (same region). In **a)** the tunneling current is $I_T = 2\,\text{nA}$, while in **b)** it is slightly increased to $I_T = 2.3\,\text{nA}$. This increase already leads to a strong change in contrast. Some FeO islands do change their appearance from lowered to pointing out of the substrate. The direction of the linescans in **a1)** and **b1)** is indicated in the corresponding micrographs.

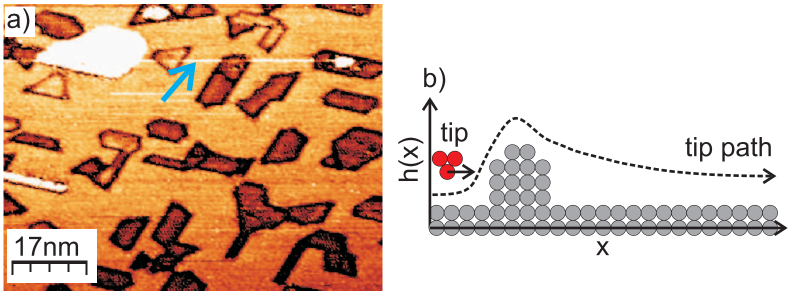

**Figure 2.34: a)** STM micrograph showing a few lines that seem to be brighter (topographically higher) than the rest of the image as indicated by a blue arrow. This is caused by a too fast measurement as illustrated in **b)**.

# 3 Material system

In the following section the materials used in this work will be introduced. First, the structural and physical properties as well as the fabrication parameters of Ag(001) substrates will be discussed. Afterward, the properties of crystalline iron films and the different iron oxides are introduced.

## 3.1 The substrate - Ag(001)

Ag has the atomic number Z=47 and belongs to the group of noble metals. It shows a very high thermal and electric conductivity ($\kappa = 429 \frac{\mathrm{W}}{\mathrm{m \cdot K}}$, $\sigma = 61.35 \cdot 10^6 \frac{\mathrm{A}}{\mathrm{m \cdot V}}$) and its melting temperature is $T_{\mathrm{melt}} = 962°\mathrm{C}$. Ag crystallizes in the face centered cubic structure (fcc) and exhibits the lattice constants $a = b = c = 4.09\,\mathrm{Å}$ [79]. Fig. 3.1 shows a bulk unit cell of Ag with indicated crystal directions.

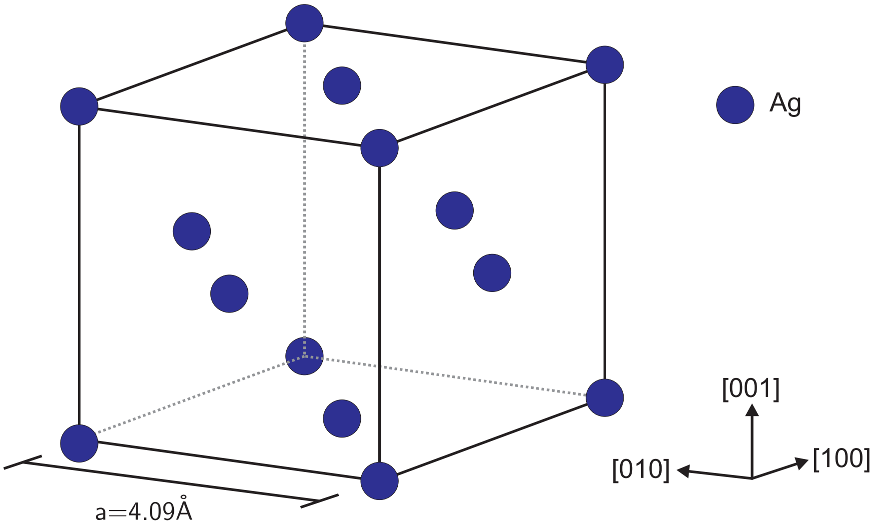

**Figure 3.1:** Schematic drawing of the Ag bulk unit cell (fcc). The lattice constant $a = 4.09\,\mathrm{Å}$ and the crystal directions are displayed for illustration.

In this work Ag(001) single crystals were used as substrates. According to the producing company *Mateck* the depth of roughness is $\Delta R < 0.03\,\mu\mathrm{m}$ at the surface of the polished crystals and the orientation accuracy is $\Delta\alpha < 0.1°$. As mentioned in Chap. 2.1.2 the lattice constants of surface and bulk can differ. In the case of Ag(001) the surface lattice constant is given by the next neighbor distance $a_{\mathrm{nn}} = a/\sqrt{2} = 2.89\,\mathrm{Å}$. A schematic drawing of the Ag(001) surface is presented in Fig. 3.2

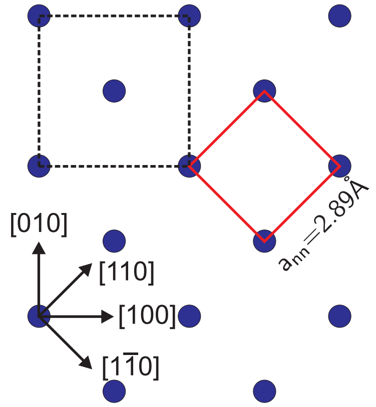

**Figure 3.2:** Schematic drawing of the Ag(001) surface. The surface as well as bulk unit cells are indicated by a red square and a dashed, black square, respectively. The surface lattice constant $a_{\mathrm{nn}} = 2.89$ Å and the surface directions are displayed for illustration.

## 3.2 The adsorbates

Since there are three different stoichiometric types of iron oxide, namely FeO (wustite), $Fe_3O_4$ (magnetite) and $Fe_2O_3$ (maghemite or hematite), the following chapter will provide information about the physical and structural properties of iron and its different oxides. Bulk crystals as well as thin films of these materials will be distinguished in the following. Prior to the introduction of the adsorbate material system Fig. 3.3 provides a phase diagram of bulk iron and its oxides as a function of temperature and oxygen partial pressure. This phase diagram was theoretically calculated from Kettler et al. [80].

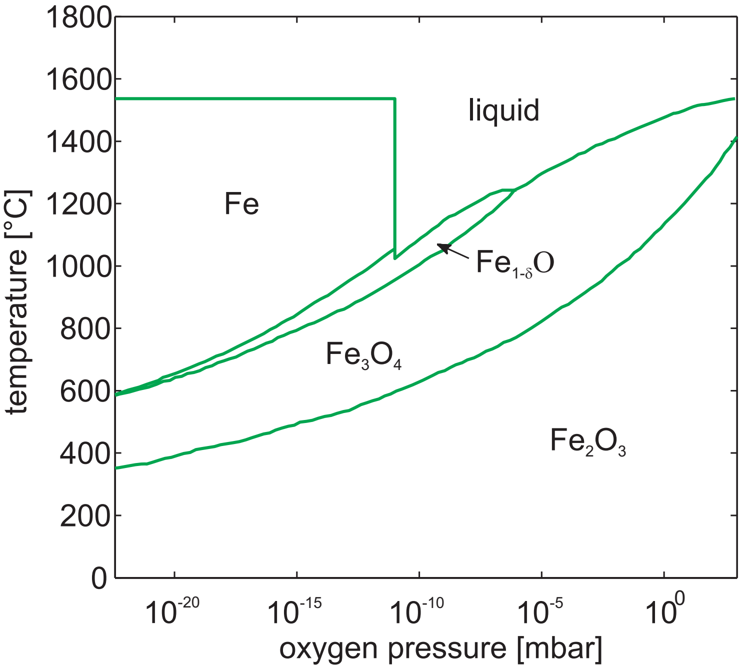

**Figure 3.3:** Phase diagram of bulk iron and its different oxides as a function of temperature and oxygen partial pressure calculated by Kettler et al. [80]. Image taken from Ref. [81] and adapted.

### 3.2.1 Iron

The transition metal Fe has the atomic number Z=26 and is one of the most stable elements. The melting point of Fe is $T_{\text{melt}} = 1538°\text{C}$. Below a temperature of 910°C it crystallizes in a stable body centered cubic (bcc) structure ($\alpha$-modification). The lattice constants of the Fe $\alpha$-modification are $a = b = c = 2.87\,\text{Å}$. Above a temperature of 910°C Fe crystallizes in the allotrope $\gamma$-modification with a fcc structure [79]. Nevertheless, all Fe films investigated within this work were treated at temperatures significantly lower than 910°C. Therefore, only the Fe $\alpha$-modification will be discussed in more detail now.

A schematic drawing of the $\alpha$-Fe bulk unit cell is presented in Fig. 3.4.

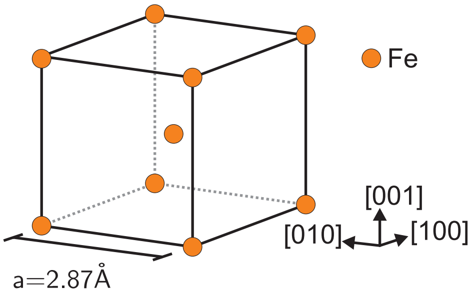

**Figure 3.4:** Schematic drawing of the $\alpha$-Fe bulk unit cell. The lattice constant $a = 2.87\,\text{Å}$ and the crystal directions are displayed for illustration.

For a bcc lattice the surface lattice constant equals the bulk lattice constant. Therefore, the lattice mismatch between Fe(001)(2.867 Å) and Ag(001)(2.89 Å) is only 0.7% and it is plausible that Fe grows in (001) direction on Ag(001) at room temperature (RT). At least for Fe(001) films with a thickness $D > 0.7\,\text{nm} \cong 5\text{ML}$ this has been proved in former studies [37, 82]. Fig. 3.5 illustrates the growth of Fe(001) on Ag(001) at RT.

One can see that the Fe unit cell grows rotated by 45° on the Ag(001) surfaces due to the lattice misfit of only 0.7% in this orientation.

It has to be noted, that studies concerning Fe films with thickness lower than 5ML reported about 3D island growth of Fe on Ag(001) [37, 38, 83]. TYSON et al. calculated the surface free energies of metal surfaces at $T = 0\,\text{K}$ resulting in $\gamma_{\text{Fe}} = 2.4\,\text{J/m}^2$ and $\gamma_{\text{Ag}} = 1.2\,\text{J/m}^2$ [83]. As explained in Chap. 2.1.3 this indicates a 3D (VOLMER-WEBER) growth mode of Fe on Ag. EGELHOFF presented a vector calculation adapting the droplet model to a crystalline system using the surface tensions of film and substrate [38].

A schematic drawing of the growth model reported by EGELHOFF is presented in Fig. 3.6.

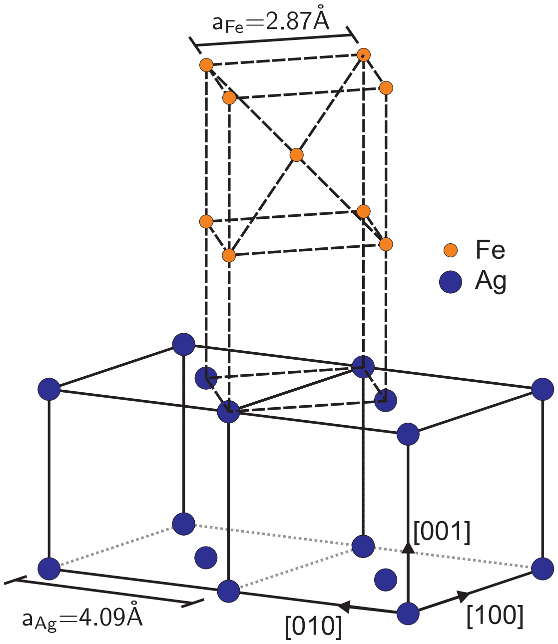

**Figure 3.5:** Schematic drawing of Fe(001) growing on Ag(001). The bulk lattice constants of both Fe and Ag as well as the crystal directions of Ag are displayed for illustration. The Fe bulk unit cell grows rotated by 45° on the Ag(001) surface due to the lattice misfit of only 0.7% in this orientation. Some Ag atoms in the unit cells are not shown for clarity reasons.

This model assumes that, if agglomeration occurs, the Fe(011) surface is favored for the side of the clusters (lowest free energy). The resulting force acting at the points A, B and C can be easily calculated via

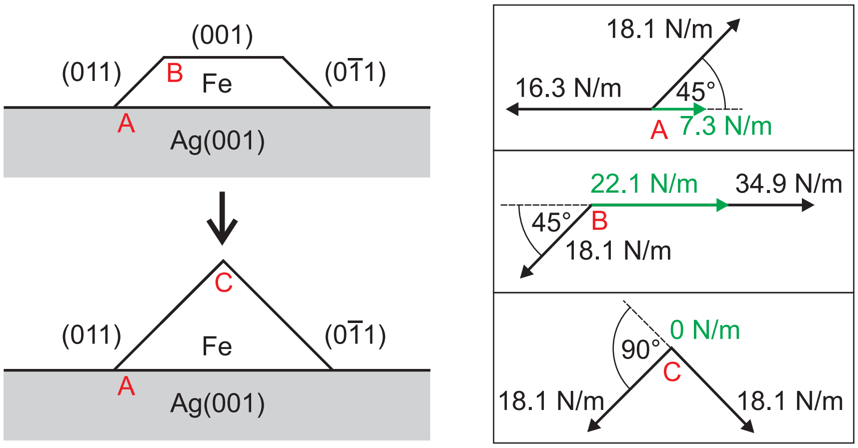

**Figure 3.6:** Schematic drawing of the surface tensions contributing to the growth of Fe(001) on Ag(001) as suggested by EGELHOFF [38]. The forces are acting at the marked points A, B and C. In this structure, the forces at both points A and B drive the Fe to recede, and stability is reached only when the pyramid is complete.

$$\mathbf{F}_{\mathrm{res}} = \mathbf{F}_1 - \mathbf{F}_2 \cos(\alpha) \ . \qquad 3.1$$

In this simple model, stability is only reached when the Fe pyramids are complete. This model was derived from calculations at $T = 0\,\mathrm{K}$, but can still serve as a clue to the initial growth of Fe on Ag(001) at RT as observed in former studies [37, 38].

### 3.2.2 FeO - wustite

Wustite is the stoichiometric iron oxide with the lowest contingent of oxygen and it is not stable under ambient conditions. Therefore, FeO forms iron discontinuities which are often indicated by the notation $\mathrm{Fe}_{1-\delta}\mathrm{O}$ with $(0.04 < \delta < 0.12)$ [84]. Wustite contains only bivalent iron ions ($\mathrm{Fe}^{2+}$) and has rocksalt structure with a bulk lattice constant of $a = b = c = 4.33\,\text{Å}$ [1]. The rocksalt structure of FeO can be build up from two fcc lattices that are shifted by $a/2$ along an edge of the unit cell. The first fcc lattice consists only of $\mathrm{Fe}^{2+}$ ions while the second fcc lattice contains only $\mathrm{O}^{2-}$ ions. The bulk unit cell of FeO is presented in Fig. 3.7.

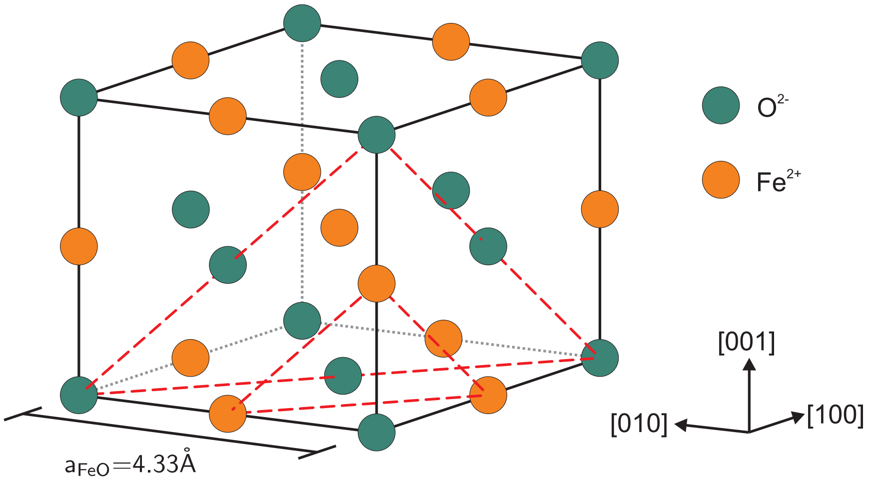

**Figure 3.7:** Schematic drawing of the FeO bulk unit cell. The lattice constant $a = 4.33\,\text{Å}$ and the crystal directions are displayed for illustration. The crystallographic (111) planes that contain only one type of ion are marked by red, dashed triangles.

For the interpretation of some experimental data it is useful to have a closer look on the (111) planes in this crystal. Thus, the crystallographic (111) planes in FeO are marked by red, dashed triangles in Fig. 3.7. Each (111) plane of FeO consists either of $\mathrm{Fe}^{2+}$ or $\mathrm{O}^{2-}$ ions, respectively. Although, FeO has a cubic bulk structure the (111) planes exhibit a hexagonal surface unit cell with a surface lattice constant (nearest neighbor distance) $a_{\mathrm{N.N.}} = 3.06\,\text{Å}$. The layer distance of the (111) planes is $d = a/\sqrt{3} = 2.5\,\text{Å}$. A side- and a topview of the FeO(111) planes is shown in Fig. 3.8.

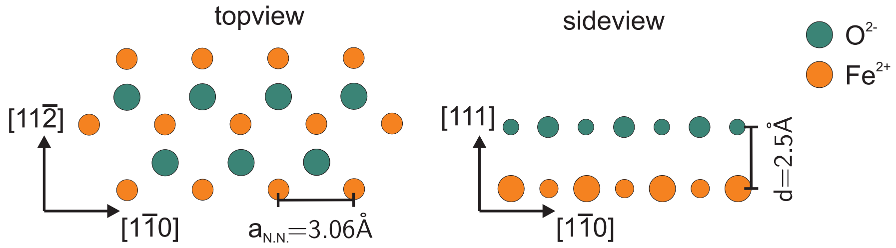

**Figure 3.8:** Schematic drawing of the FeO (111) planes consisting either of $Fe^{2+}$ or $O^{2-}$ ions. The surface lattice constant $a_{\mathrm{nn}} = 3.06\,\text{Å}$ and the layer distance $d = 2.5\,\text{Å}$ as well as the FeO crystal directions for side- and topview are displayed for illustration. Larger ions are closer to the eye.

### 3.2.3 $Fe_3O_4$ - magnetite

Magnetite ($Fe_3O_4$) crystallizes in the inverse spinel structure (cubic) with the lattice constants $a = b = c = 8.39\,\text{Å}$. $Fe_3O_4$ contains both $Fe^{2+}$ and $Fe^{3+}$ ions. An inverse spinel can generally be described with the constitutional structure formula $B(BA)C_4$. It consists of an fcc sublattice formed by atoms of type C, a tetrahedral sublattice occupied by another kind of atoms (B) and an octahedral sublattice containing atoms of type B and A. In the case of magnetite the fcc sublattice (C) is formed by $O^{2-}$ ions, the tetrahedral sites contain $Fe^{3+}$ (B) ions and in each case 1/2 of the octahedral sites is occupied by randomly distributed $Fe^{3+}$ (B) or $Fe^{2+}$ (A) ions [1]. Therefore, the structure formula of magnetite is

$$\mathrm{B(BA)C_4} \mathrel{\hat{=}} \mathrm{Fe^{3+}(Fe^{3+}Fe^{2+})O_4^{2-}} \ . \tag{3.2}$$

Fig. 3.9 shows a schematic drawing of the $Fe_3O_4$ bulk unit cell.

Magnetite is a ferrimagnet with a magnetic moment of $4\mu_B$ because of the antiparallel coupling of the spin moments of the tetrahedral and octahedral sites. It has to be noted that magnetite exhibits a full spin polarization at the FERMI level [6].

It is well known from former studies that the (001) surface of $Fe_3O_4$ exhibits a $(\sqrt{2} \times \sqrt{2})R45^\circ$ superstructure [85, 86, 87]. In these studies the observed superstructure was explained either by a termination by tetrahedral iron ions or by octahedral coordinated iron and oxygen ions. Here, the actual termination depends strongly on the preparation parameters [13].

### 3.2.4 $Fe_2O_3$ - maghemite and hematite

$Fe_2O_3$ can exist in two different stable structures, namely maghemite ($\gamma$-$Fe_2O_3$) and hematite ($\alpha$-$Fe_2O_3$). Hematite reveals a trigonal corundum structure while maghemite crystallizes in a defect-spinel structure and can be seen as $Fe^{2+}$ deficient magnetite structure containing only $Fe^{3+}$ ions. To achieve charge balance a part of the octahedral sites that are occupied by $Fe^{2+}$ in magnetite are unoccupied in maghemite [1].

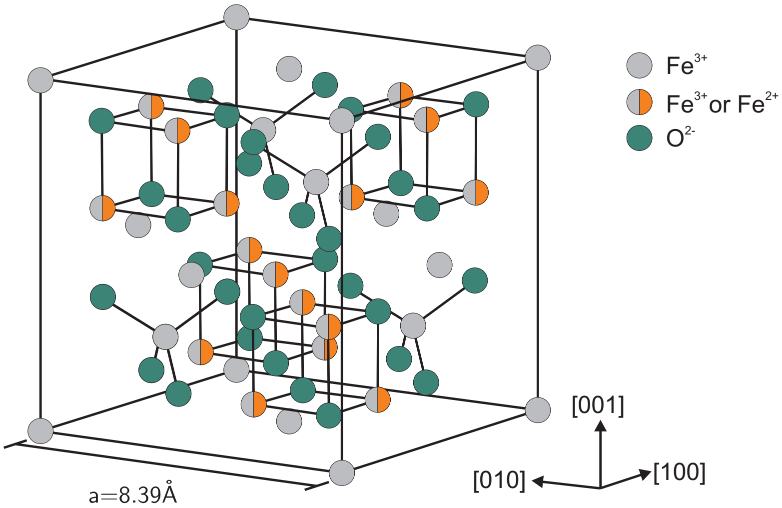

**Figure 3.9:** Schematic drawing of the $Fe_3O_4$ bulk unit cell. The surface lattice constant $a = 8.39\,\text{Å}$ as well as the crystal directions are displayed for illustration. The fcc sublattice is formed by $O^{2-}$ ions, the tetrahedral sites contain $Fe^{3+}$ ions and in each case 1/2 in total of the octahedral sites is occupied by randomly distributed $Fe^{3+}$ or $Fe^{2+}$ ions [1]. For clarity reasons all possible octahedral and tetrahedral sites are indicated in the picture.

The kind of structure in which $Fe_2O_3$ grows depends strongly on the substrate. Since the Ag(001) substrates used in this work have a square surface unit cell, it is likely that $Fe_2O_3$ would grow as maghemite on top of Ag(001). Hence, the bulk structure of hematite will wot be considered in the following. The bulk lattice constants of maghemite are $a = b = c = 8.34\,\text{Å}$ and its bulk unit cell is presented in Fig. 3.10.

It has to be noted, that all possible octahedral and tetrahedral sites are indicated in Fig. 3.10, although not every possible site is occupied by an $Fe^{3+}$ ion (see above).

### 3.2.5 Lattice mismatch between Ag(001) and the adsorbates

For the epitaxial growth of thin films the lattice mismatch between substrate and adsorbate is an important factor. A small lattice misfit (low strain) can be essential to grow films with low defect density. A larger lattice misfit, on the other hand, can lead to dislocations at the substrate-film interface which can have a huge impact on the surface structure for example by forming undulations, mosaics or domain boundaries. Concerning thin iron oxide films, a large lattice misfit to the substrate can (from an energetic point of view) even favor the formation of a specific stoichiometric iron oxide phase. The lattice misfits $\eta_0$ as well as the corresponding lattice constants and layer distances for the different (001) oriented iron oxides are given in Tab. 3.1

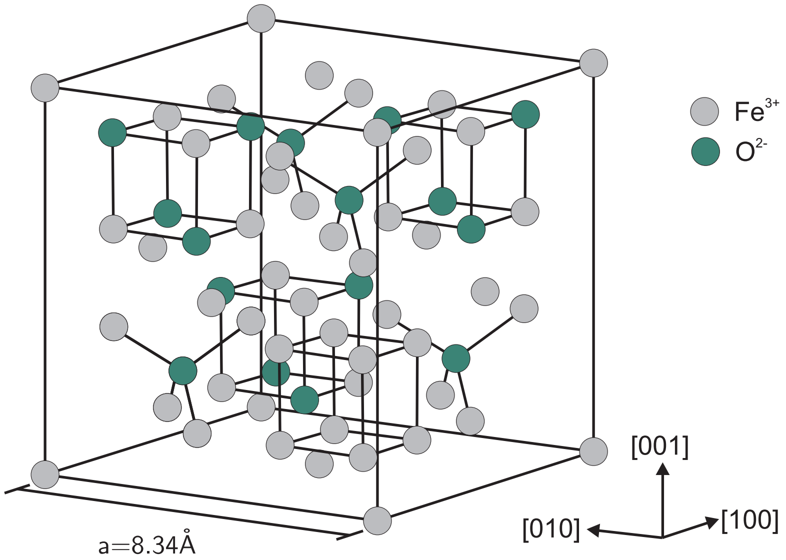

**Figure 3.10:** Schematic drawing of the maghemite bulk unit cell. The surface lattice constant $a = 8.34\,\text{Å}$ as well as the crystal directions are displayed for illustration. The fcc sublattice is formed by $O^{2-}$ ions, the tetrahedral sublattice sites as well as the octahedral sublattice sites can contain $Fe^{3+}$ ions (not all sites are occupied to achieve charge balance) [1]. For clarity reasons all possible octahedral and tetrahedral sites are indicated in the picture.

| | $a$[Å] | $d$[Å] | $\eta_0$ to Ag(001)[%] |
|---|---|---|---|
| Ag(001) | 4.09 | 2.05 | - |
| Fe(001) | 2.87 | 1.44 | 0.7 |
| FeO(001) | 4.33 | 2.17 | 5.9 |
| $\gamma$-$Fe_2O_3$(001) | 8.34 | 2.95 | 2.0 |
| $Fe_3O_4$(001) | 8.39 | 2.97 | 2.7 |

**Table 3.1:** Lattice mismatch $\eta_0$ between Ag(001) and iron as well as the three (001) oriented iron oxides. The corresponding lattice constants and layer distances are also displayed for comparison.

# 4 Experimental setup

In the following chapter the experimental setup inside the used UHV chambers will be introduced. Afterward, the technical setup of the used techniques LEED, SPA-LEED, XPS, AES and STM will be described very briefly. In the end the different sample preparations will be discussed.

## 4.1 The UHV chambers

Two different UHV chambers were used during this work. The first chamber is equipped with a LEED, an XPS and an STM while the second UHV chamber has a SPA-LEED as well as an AES system. The base pressure in both experimental chambers is $10^{-10}$ mbar. Fig. 4.1 shows photos and a layout sketch of both chambers.

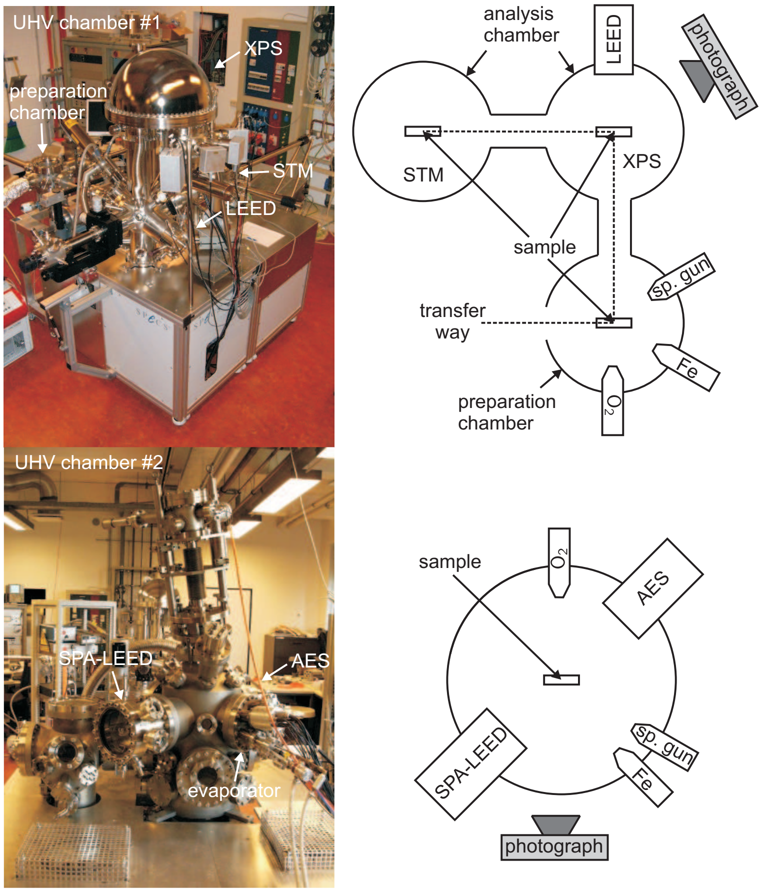

**Figure 4.1:** Photos and schematic drawings of the two UHV chambers used during this work. The direction from which the photograph was taken is indicated in the schematic drawings.

All sample holders in the UHV chambers are able to heat the sample up to $T = 600^\circ$ C via electron bombardment heating.

## 4.2 SPA-LEED and LEED

An important analysis method for the determination of surface structures within this work is SPA-LEED. This technique is based on the diffraction of low-energy electrons at crystal surfaces (cf. Chap. 2.2). The used SPA-LEED is a commercialized second generation OMICRON system. Fig. 4.2 shows a schematic build-up of the SPA-LEED system. The electrons are accelerated from an electron gun at energies between 0eV and 500eV and focussed onto the sample surface by a lens system. These electrons are diffracted at the sample surface and can return through the SPA-LEED optics where they are focused into a channeltron detector. The electrons pass an electric field generated by an octopole plate system on their way through the SPA-LEED optics. This electric field is varied within the measurement (constant electron energy) and, therefore, the incident angle of the electron beam onto the sample changes and the reciprocal space can be scanned laterally.

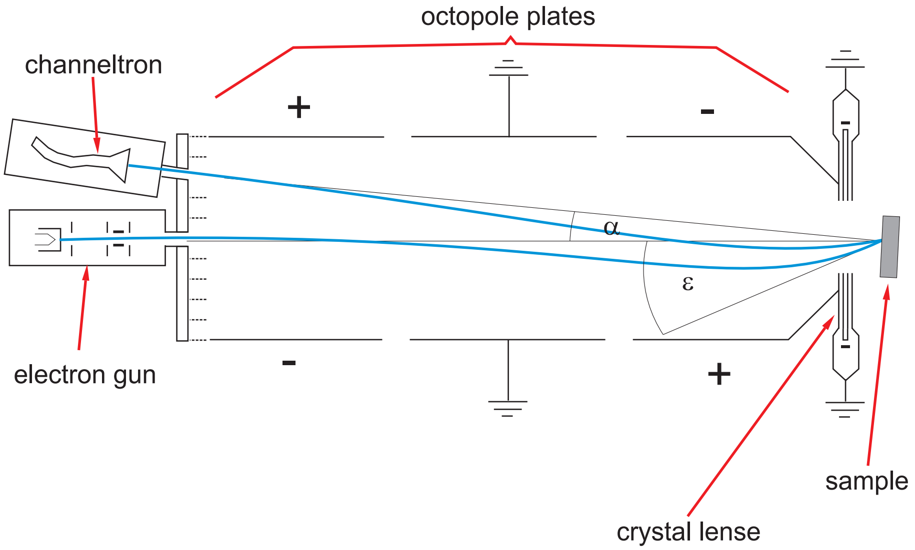

**Figure 4.2:** Schematic build-up of the OMICRON SPA-LEED system used within this work.

An advantage over conventional LEED is the possibility to analyze the specular diffraction rod, which is not covered by the electron gun. Additionally, the analysis of the spot profiles can give quantitative information about surface structure and morphology (e.g. terrace widths, mosaic spread, step height), while a LEED allows only a qualitative analysis. This is due to the digital recording of the diffracted intensities measured with the channeltron detector in the SPA-LEED system. Also, the transfer width of the SPA-LEED system is with about 100nm ten times larger compared to the transfer width of a LEED (10nm).

The transfer width describes the coherence length of the electron beam at the surface and is, therefore, a measure for the lateral resolution of the LEED or SPA-LEED system. Thus, SPA-LEED allows to investigate larger crystalline structures at the sample surface compared to LEED [88].

Nevertheless, LEED is a sufficient method to get an idea about the surface structure and was also used within this work. The main difference to a SPA-LEED system is the detection of the diffracted electrons by a screen instead of a channeltron. The electrons that are diffracted under different angles are displayed simultaneously on the screen which supersedes an octopole deflecting unit. A build-up sketch of a LEED system as used for this work is presented in Fig. 4.3.

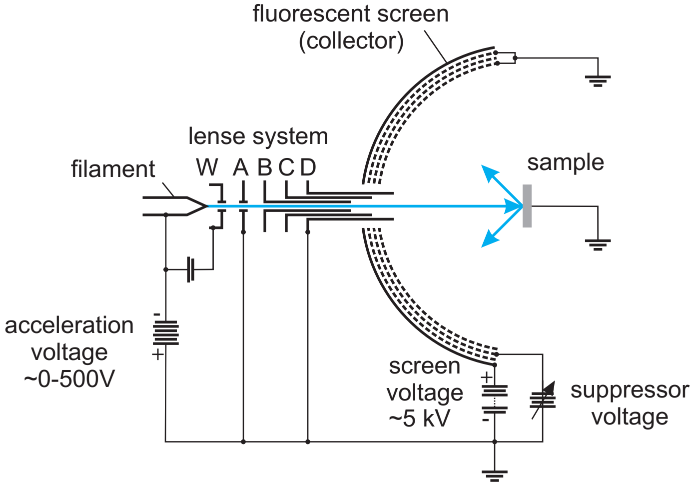

**Figure 4.3:** Schematic build-up of the LEED system used within this work. The Image is taken from Ref. [89] and modified.

The electrons from the filament are accelerated toward the sample passing a Wehnelt-cylinder (W) and an electrostatic lens system (A, B, C, D) where the beam is collimated and focused. The diffracted electrons are displayed on a fluorescent screen. A counter voltage of $0 - 300\,\mathrm{V}$ is applied to the suppressor grid to cull inelastically scattered electrons.

## 4.3 Scanning Tunneling Microscope (STM)

The STM used in this work is a type *Aarhus 150* SPM (scanning probe microscope) produced by the company SPECS. The STM is mounted on a heavy aluminum block that is mechanically decoupled from the UHV chamber by spiral springs and viton bands to suppress vibrations of high as well as low frequency. The detector head is embedded into the aluminum block and has two motors for approaching and scanning the sample surface, respectively. The first motor is a so-called inch-worm motor that approaches the tip to the sample surface until a tunneling current is measured. Afterward, the fine approach is done by a piezo motor. This piezo motor is also allowing a maximum lateral scanning range of

$(2 \times 2)\,\mu\text{m}^2$. The assembly of the detector head of the STM is shown in Fig. 4.4.

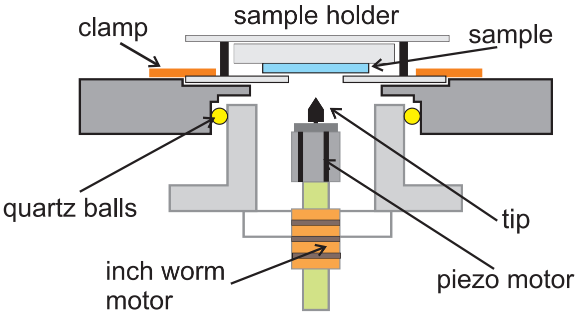

**Figure 4.4:** Schematic drawing of the STM detector head. Image taken and adapted from Ref. [67].

The tip is made of an etched tungsten wire. Here, the tungsten wire is electrochemically etched in a caustic potash. This leads to a very sharp tip. In UHV the tungsten tip gets sputtered by $Ar^+$ ions to remove the oxide layer covering the tip. A scanning electron microscope image from an etched tip is shown in Fig. 4.5.

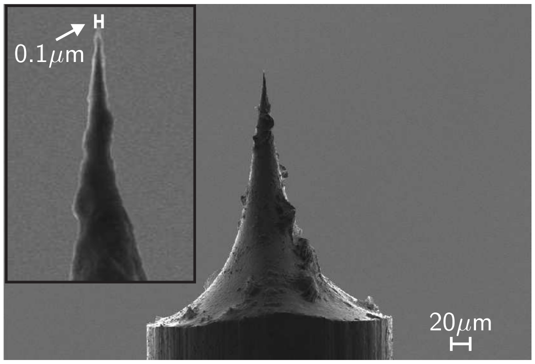

**Figure 4.5:** **S**canning **E**lectron **M**icroscope (SEM) image of the etched tungsten tip. The tip shows a diameter of around $0.1\,\mu\text{m}$ in this image. Probably the diameter of the tip is even smaller, since this image was taken at the resolution limit of the SEM.

The STM can be operated either in constant current or constant height mode. The constant height mode is only suited for very flat surfaces, since the tip may crash into three dimensional structures. For this work only the constant current mode was used. This mode reduces the risk of crashing the tip into the sample surface (cf. Chap. 2.6). All STM measurements in this work were performed at RT at a base pressure of $10^{-10}$ mbar. The STM images presented in this work were processed with the software WSxM from Horcas et al. [90].

## 4.4 AES

The used Auger **E**lectron **S**pectrometer AES for this work was produced by PERKIN-ELMER (cf. Fig. 4.6). The electrons are emitted by a filament and accelerated onto the sample surface at an energy of 2keV. The electron beam is focused by a Wehnelt cup (V1) and electron lenses (V2) onto the sample with a beam diameter of 1mm at the focus point. The emitted Auger electrons from the sample reach a cylindrical mirror analyzer (CMA) that can be passed only by electrons of a specific energy due to the electric field inside the CMA. The passed electrons are detected by an electron multiplier. The electric field inside the CMA is varied during an AES experiment so that an energy spectrum of the emitted electrons can be obtained.

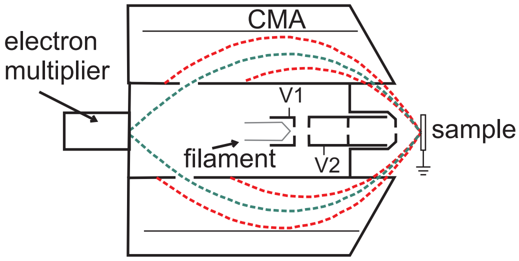

**Figure 4.6:** Schematic build-up of the AES optics used in this work. Only the electrons that have the fitting kinetic energy can pass the CMA (dashed, green lines).

## 4.5 XPS

For chemical analysis of the sample surface also an XPS from SPECS was used. The X-ray source is of the type *XR50* and the semi spherical analyzer is a *PHOIBOS 150*. The X-rays are emitted from an Al anode. Since the XPS has no monochromator the photoemisson spectra are mainly influenced by the most intense emission lines of the Al anode, which is $E_{K,\alpha} = 1486.6\,\text{eV}$. A schematic drawing of the X-ray source and the semi spherical analyzer is given in Fig. 4.7.

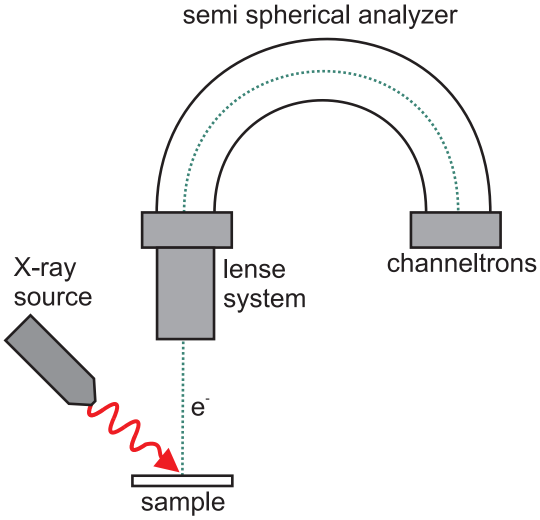

**Figure 4.7:** Two dimensional schematic build-up sketch of the SPECS XPS system used in this work.

The emitted photoelectrons are focused by lense system and enter a semi spherical analyzer afterward. Only photoelectrons with a specific energy can pass the analyzer and reach the channeltrons. Therefore, by varying the electric field inside the semi spherical analyzer a spectrum of the emitted photoelectrons is obtained. The *PHOIBOS 150* analyzer possesses a six channeltron array and during a measurement the signals of all six channels are added up.

## 4.6 The evaporator

An illustration of the Fe evaporator is shown in Fig. 4.8. For the deposition of the films for this work an electron bombardment evaporator was used. A positive voltage of 1kV is applied to an Fe rod. Electrons are emitted from a tungsten filament and accelerated onto the Fe rod due to the positive potential. Therefore, the Fe is heated up until it sublimates. The Fe vapor is guided out of the copper cell through two apertures that are used to restrict the molecular beam to the substrate. A shutter at the end of the evaporator can be used to cut off the molecular beam immediately. Finally, the amount of evaporated material can be determined by an oscillating quartz, since the decrease in eigenfrequency of the quartz is proportional to the adsorbed mass on it. This decrease is described by the Sauerbrey equation

$$\Delta f = -S_f \frac{\Delta m}{A} \ . \qquad 4.1$$

Here, $S_f$ is the Sauerbrey constant that includes the eigenfrequency of the quartz as well as its density. $\Delta m$ is the mass adsorbed on the area $A$ on the quartz surface [91].

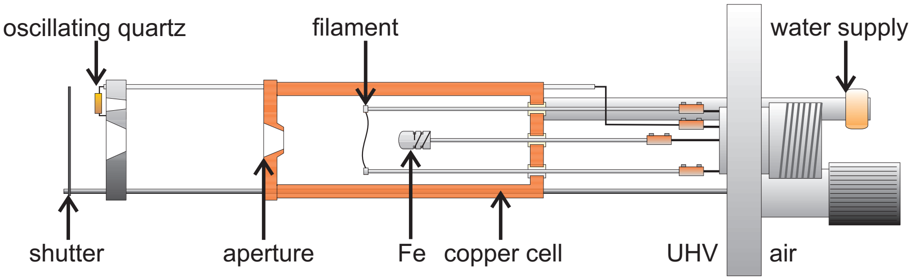

**Figure 4.8:** Schematic drawing of the used Fe evaporator. The fundamental parts are indicated by black arrows. The image was taken from Ref. [67] and modified .

## 4.7 Sample preparation

In the following the cleaning process of the Ag(001) substrates and the three different sample preparations investigated during this work will be presented.

**Preparation of the Ag(001) substrates**

All Ag(001) substrates used in this work were prepared the same way. The as-delivered substrates are transfered into the UHV chamber. The surface is etched by $Ar^+$ sputtering at a substrate temperature of 200°C for 30 minutes. The $Ar^+$ partial pressure is $10^{-4}$ mbar and the ion current is 100nA at an accelerating voltage of 1kV. Afterward the substrate is annealed at 500°C in UHV for 30 minutes with a temperature ramp of 5°C/min. This procedure is repeated for several cycles until the LEED or SPA-LEED patterns show sharp diffraction spots of the expected $(1 \times 1)$ structure of Ag(001) and XPS or AES show no contaminations at the surface (e.g. carbon or oxygen), respectively. Fig. 4.9 shows a LEED pattern and an XP spectrum of a prepared Ag(001) substrate. A detailed analysis of the prepared substrate surface including STM measurements will be given in chapter 5.1.

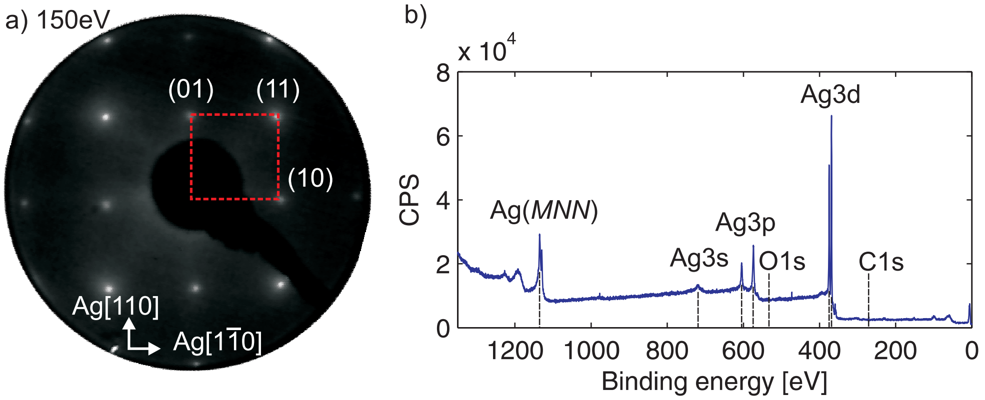

**Figure 4.9: a)** LEED pattern of a prepared Ag(001) substrate at an electron energy of 150 eV. The expected $(1 \times 1)$ structure is clearly visible marked by a dashed, red square. **b)** XP spectrum (survey) of a prepared Ag substrate. The Ag3s, Ag3p, Ag3d photoemission peaks and the Ag($MNN$) AUGER transition are marked by dashed lines. There are no contaminations visible in the spectrum (e.g. C or O).

### UHV annealed Fe films on Ag(001)

Within the first preparation process Fe films of different thickness were deposited at RT onto the cleaned Ag(001) substrates. The deposition was done by molecular beam epitaxy (cf. Chap. 4.6) of iron (99.99%) at a pressure of $10^{-8}$ mbar. The film thickness was calibrated after deposition via quantitative AES (cf. Chap. 2.5). Structure, morphology and chemical composition of the as-depostited films were analyzed by SPA-LEED and AES or LEED, XPS and STM, respectively. Afterward, the films were annealed in UHV at 250°C for 50 minutes to investigate the reported Ag segregation [30, 31]. The annealed films were also analyzed by all prior named techniques epending on the UHV chamber the films were prepared in.

### Fe films annealed in $O_2$ on Ag(001)

In another approach the as-deposited Fe films (same deposition parameters as described above) were annealed in $10^{-5}$ mbar $O_2$ at 300°C for 1h. We performed STM and LEED measurements before and after the annealing process to investigate the surface structure of the films.

### Reactive deposition of Fe in $O_2$ atmosphere on Ag(001)

The third preparation method is based on the reactive deposition of Fe in an $O_2$ atmosphere ($10^{-5}$ mbar) at substrate temperatures of 200°C up to 400°C. The temperature dependence on the structure and morphology of the films as well as their stoichiometry was investigated by SPA-LEED and AES or LEED, XPS and STM, respectively.

# 5 Experimental results and discussion

This chapter deals with the experimental results obtained during this work. The prepared samples were analyzed by LEED, SPA-LEED, STM, XPS and AES (introduced in Chap 4). The three different film preparations described in Chap. 4.7 lead to significant differences in structure and chemical composition of the films. Thus, the experimental results from each preparation will be considered in detail individually followed by a separate discussion. In each discussion the experimental results will be compared to other studies. An overall conclusion will be given afterward in Chap. 6.

At first, structure and chemical purity of the prepared Ag(001) substrates will be analyzed, followed by the description of the as deposited Fe films on top of the substrates. Chap. 5.3 will be about the Fe films annealed in UHV and in Chap. 5.4 the structure and composition of the Fe films annealed in $O_2$ will be analyzed. The last chapter 5.5 will shed light on the iron oxide films grown by reactive deposition of Fe in $O_2$ atmosphere.

## 5.1 The prepared Ag(001) substrates

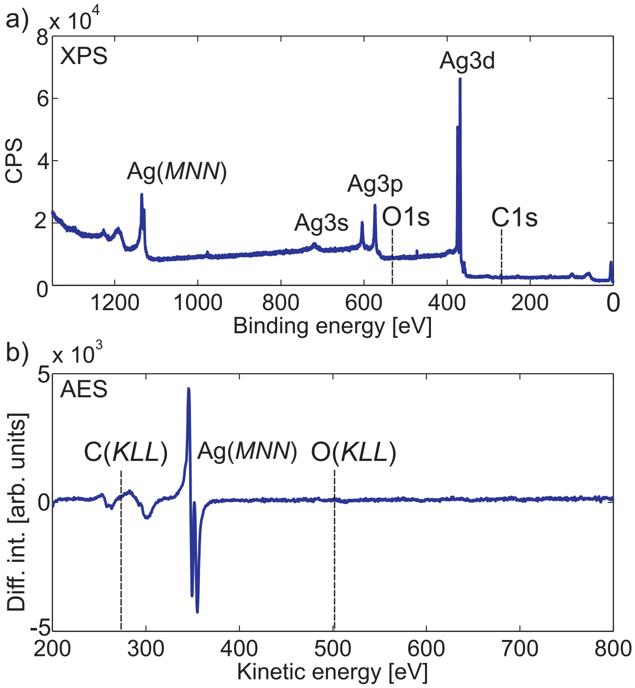

**Figure 5.1: a)** XP spectrum (survey) of a prepared Ag substrate. The Ag3s, Ag3p, Ag3d photoemission peaks and the Ag($MNN$) Auger transition are indicated. There are no contaminations visible in the spectrum (e.g. C or O). **b)** AE spectrum of a prepared Ag substrate. The Ag($MNN$) Auger transition is marked and no contamination with either O (O($KLL$) at 503eV) or C (C($KLL$) at 271eV) can be detected.

All Ag(001) substrates that served as foundation for the produced iron and iron oxide films were prepared in the same way explained in Chap. 4.7. Since the substrates were prepared in two different UHV chambers it is important to ensure that the cleaned substrates are of the same quality. Otherwise a reliable comparison of the produced films would not be possible in the following. At first, the chemical purity of the substrate surface after the cleaning process was analyzed by either AES or XPS, depending on the UHV chamber the substrate was prepared in. Fig. 5.1 shows AE and XP spectra of such cleaned Ag(001) substrates.

One can clearly see Ag photoemission peaks in the XP spectrum and the Ag($MNN$) Auger transition in the AE spectrum. No contamination of the cleaned Ag(001) surfaces by carbon or oxygen, for instance, can be found.

Furthermore, surface structure and crystalline quality of the Ag(001) substrates were investigated by STM as well as SPA-LEED, or LEED. Exemplary diffraction patterns obtained from prepared Ag(001) surfaces by SPA-LEED and LEED are shown in Fig. 5.2.

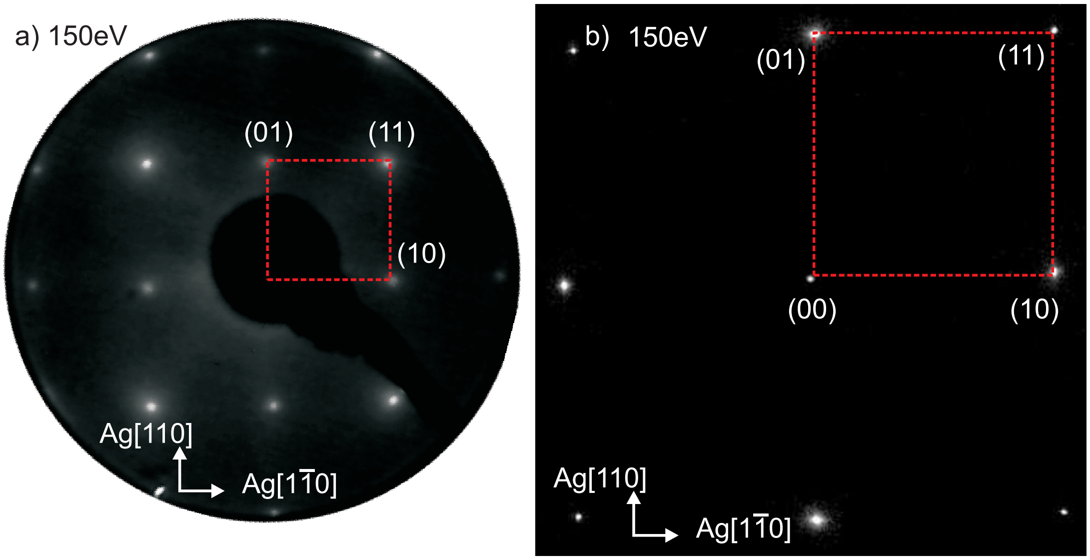

**Figure 5.2:** a) LEED and b) SPA-LEED diffraction patterns of the prepared Ag(001) substrate. Both patterns show the typical (1 × 1) structure of a Ag(001) surface due to its square surface unit cell. The spots are sharp and intense, while there is only a very low diffuse background in both patterns. Some fundamental diffraction spots are named for clarity. The (00) spot in a) is covered by the electron gun.

In both diffraction patterns a clear (1 × 1) structure corresponding to the square surface unit cell of Ag(001) can be seen. The diffraction spots are sharp and intense while the diffuse background is quite low in both patterns. This indicates a low point defect density at the surface with large crystalline areas.

Linescans of the (00) spot obtained from the SPA-LEED measurements were used to determine the crystalline quality of the surface in more detail. Fig. 5.3 illustrates the spot profiles measured in Ag[1$\bar{1}$0] direction at different electron energies.

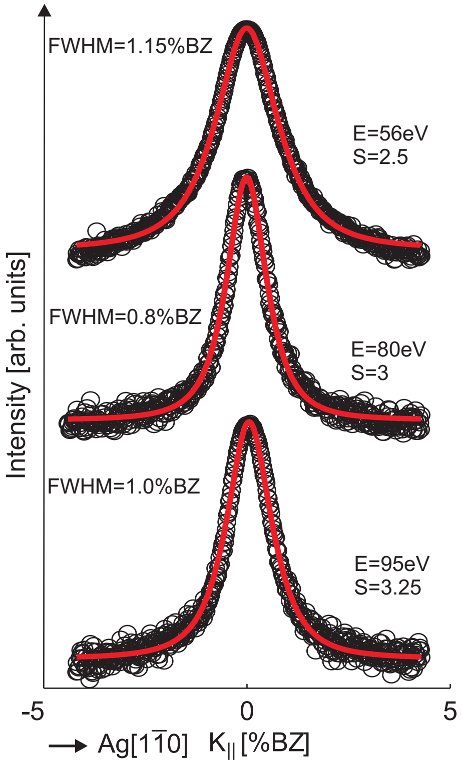

**Figure 5.3:** Profiles of the (00) spot measured in Ag[1$\bar{1}$0] direction. Electron energies are 56 eV ($S = 2.5$), 80 eV ($S = 3$) and 95 eV ($S = 3.25$). The profiles are fitted by LORENTZIAN functions. The resulting FWHM are indicated beneath the profiles.

The profiles were fitted by single LORENTZIAN functions using the software *ReflexFit* from S. GEVERS [46]. For these three spot profiles the FWHM of the (00) spot is the smallest at an *in-phase* condition of Ag(001) (here $S = 3$, FWHM $= 0.8\%$ BZ) while it has a bigger value at an *out-of-phase* condition (here $S = 2.5$, FWHM $= 1.15\%$ BZ). The FWHM of the (00) spot at the intermediate phase condition $S = 3.25$ lies in between those values (FWHM $= 1.0\%$ BZ). From now on all given scattering conditions are scaled to the atomic layer distance of the substrate Ag(001) ($d = 2.05$ Å) for reasons of comparability.

It was described in Chap. 2.2.3 that the behavior of the FWHM of the diffraction spots with increasing electron energy (or increasing scattering phase $S$) can give information about average terrace widths, mosaic spreads and layer distances at the sample surface (H(S) analysis). Hence, Fig. 5.4 shows the evaluation of the FWHM of the (00) spot depending on the scattering phase.

The periodicity $\Delta S^{\mathrm{osc}}$ of the FWHM depends on the atomic step height $d$ while the amplitude $\Delta K_{||}^{\mathrm{osc}}$ is determined by the average terrace size $\Gamma$. The additional linear increase of the FWHM is caused by surface mosaics. Its slope $m = \Delta K_{||}^{\mathrm{lin}} / \Delta S^{\mathrm{lin}}$ is proportional to the mosaic spread $\Delta\vartheta$ at the surface (cf. Chap. 2.2.3). The values for $\Gamma$, $\Delta\vartheta$ and $d$ calculated from the H(s) analysis shown in Fig. 5.4 are $\Gamma = 96$ nm, $\Delta\vartheta = 9$ mdeg, and $d = 2.04$ Å.

It has to be noted that the expected $\Delta S^{\mathrm{osc}}$ for step heights of bulk Ag(001) are very good reflected by the curves of the clean Ag(001) substrate seen in Fig. 5.4. This cosine-like

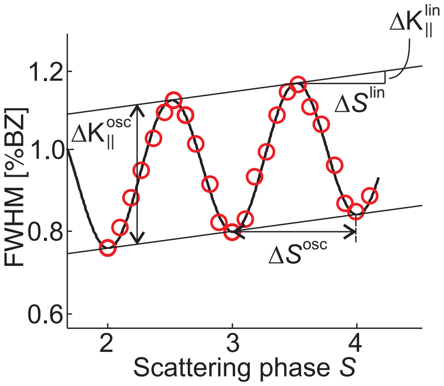

**Figure 5.4:** FWHM of the (00) spot depending on the scattering phase. The values $\Delta S^{\text{osc}}$, $\Delta S^{\text{lin}}$, $\Delta \text{K}_{||}^{\text{osc}}$ and $\Delta \text{K}_{||}^{\text{lin}}$ which are needed for calculation of the terrace width $\Gamma$, the mosaic spread $\Delta\vartheta$ and the layer distance $d$ are indicated for clarity.

behavior of the FWHM points to the exclusive presence of monoatomic steps at the surface. Additionally, the mosaic spread $\Delta\vartheta = 9\,\text{mdeg}$ is negligible. In connection with the large average terrace width of $\Gamma = 96\,\text{nm}$ this speaks for a long range order and a very low point defect density at the Ag(001) surface. We would like to point out, that the calculated average terrace width of $\Gamma = 96\,\text{nm}$ is very close to the maximum transfer width and, therefore, the resolution of the SPA-LEED system (cf. Chap. 4.2). Hence, it is likely that the actual average terrace width is even bigger than the calculated value. By extrapolation of the FWHM for $S \to 0$ (FHWM(S=0)= 0.64 %[BZ]) one can estimate the average lateral crystallite size to $D = 45\,\text{nm}$.

Finally, we performed STM measurements in order to investigate the prepared Ag(001) surfaces and to verify the results from the electron diffraction experiments. This is also reasonable since only UHV chamber #2 is equipped with a SPA-LEED system and UHV chamber #1 with a LEED and an STM. Hence, it is guaranteed that all prepared substrates in both chambers are of the same quality. All STM measurements were performed at RT at a base pressure of $10^{-10}$ mbar. An exemplary selection of STM micrographs obtained from one prepared Ag(001) substrate is shown in Fig. 5.5.

It can be seen that the prepared Ag(001) surface reveals large and flat terraces which are separated by either some short terraces (step bunch) or just one monoatomic step. The terrace width (of the large terraces) is clearly larger than 100 nm. The terraces are atomically flat with no detectable defects. In this work we either used a simple greyscale colormap (white=high and black=low) or the colormap presented in Fig. 5.5 a) for comparison. For quantitative height information we provide linescans from the two dimensional STM micrographs in this work.

Lineprofiles obtained from the prepared Ag(001) substrate are shown in Fig. 5.6. These lineprofiles are cutouts from the two dimensional STM images in Fig. 5.5 and are indicated in the images by red and green arrows.

Fig. 5.6 a) shows the periodicity of the next neighbor atoms at the Ag(001) surface. The average distance between next neighbor atoms results in 2.9 Å which is in agreement with literature values ($a_{\text{N.N.}} = 2.9\,\text{Å}$). A linescan along a step at a terrace edge can be seen in Fig. 5.6 b).

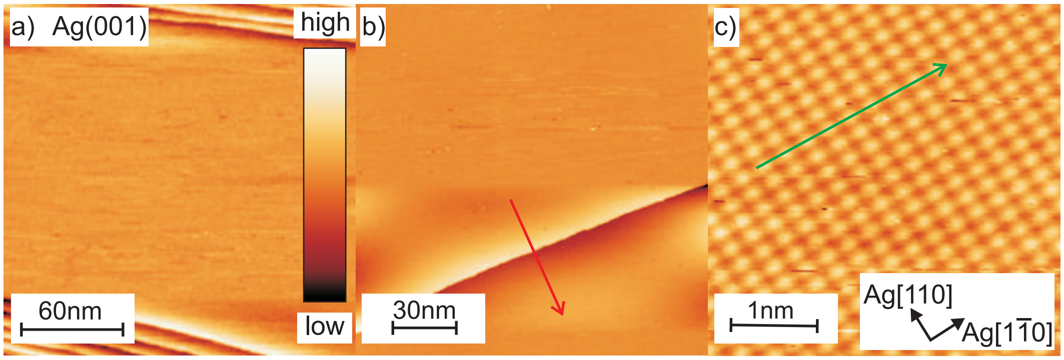

**Figure 5.5:** STM micrographs of the prepared Ag(001) surface. Bias voltage is 1 V and tunneling current is 1 nA in a) and b) as well as 0.3 V and 1.2 nA in c). Large, flat terraces are separated by either a) some short terraces or b) just one monoatomic step. Image c) shows, that the Ag(001) terraces are in fact atomically flat with no detectable defects. The red and green lines in b) and c) mark corresponding lineprofiles that can be seen in Fig. 5.6.

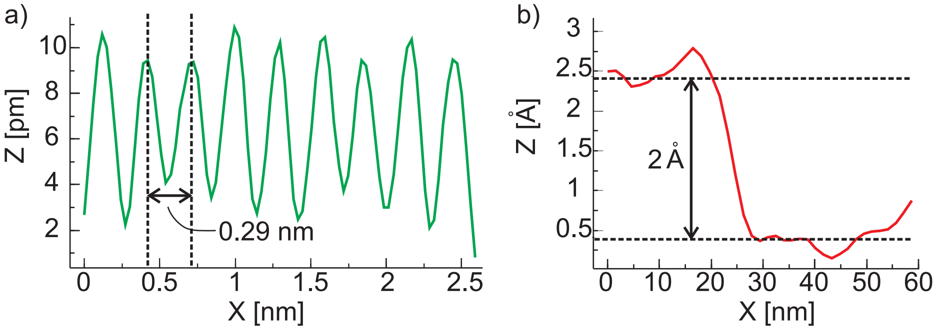

**Figure 5.6:** Lineprofiles taken from the two dimensional STM images of Fig. 5.5. **a)** shows a lineprofile revealing the periodicity of the next neighbor atoms at the Ag(001) surface. The average distance between next neighbor atoms results in 2.9 Å. The profile given in **b)** is a linescan along a step at a terrace edge. The step height is $d_{\text{step}} \approx 2$ Å.

Although, height measurements with an STM have to be taken carefully (cf. Chap. 2.6.3), one can see that the step height is $d_{\text{step}} \approx 2.0$ Å, which agrees to the literature value ($d_{\text{step,lit}} = 2.1$ Å) of a monoatomic step at Ag(001). This reflects well the results from the prior shown H(S) analysis. Thus, biatomic steps at the surface can be excluded. All in all, the Ag(001) substrates from both chambers have the same sufficient quality after the preparation described in Chap. 4.7.

## 5.2 Ag(001) substrates $Ar^+$ etched at RT

As shown in former studies it is crucial to use a sufficient substrate temperature during sputtering the Ag(001) surface [92]. The temperature which leads to the large, defect free Ag terraces shown before is about 200°C. A lower substrate temperature during sputtering leads to a roughening of the substrate surface. At the beginning of our experiments we etched a Ag(001) substrate via $Ar^+$ sputtering at RT and did STM measurements for comparison. Some STM images obtained from the Ag(001) substrate $Ar^+$ etched at RT are presented in Fig. 5.7.

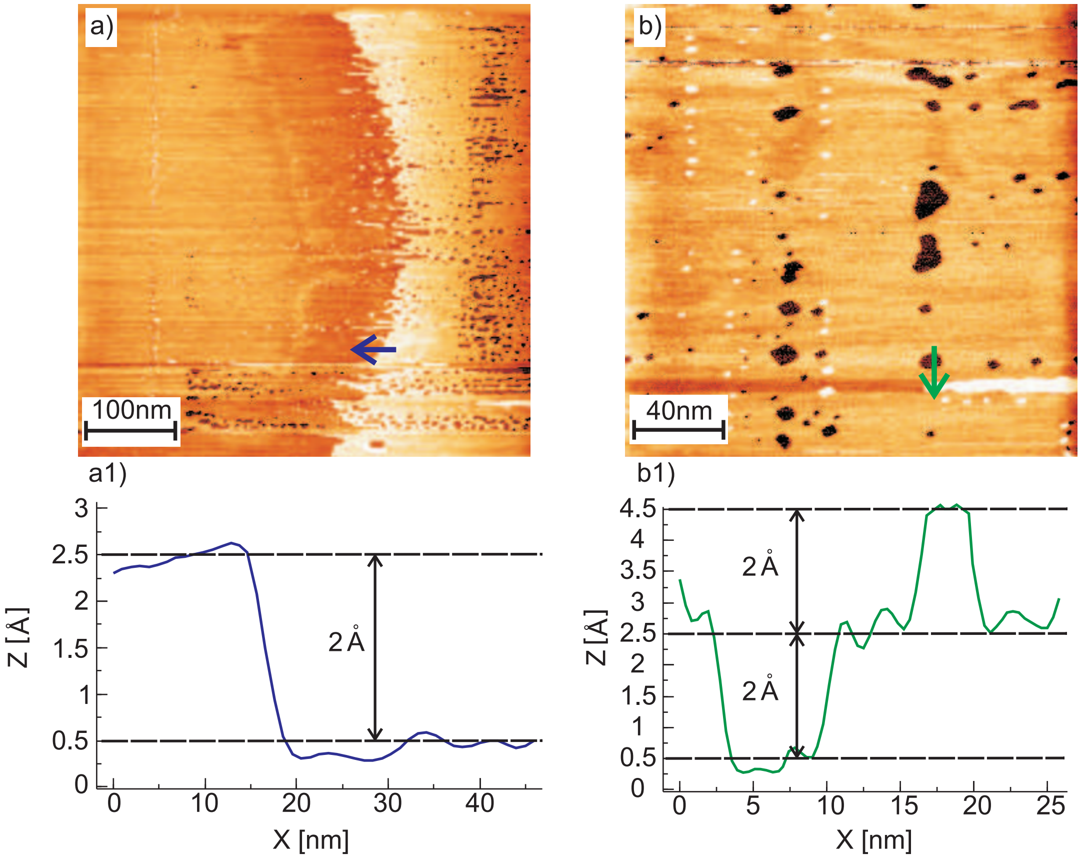

**Figure 5.7:** STM micrographs of the Ag(001) substratre $Ar^+$ etched at RT. Bias voltage is 1 V and tunneling current is 1 nA. Image a) shows the roughening of the step edges at the surface and image b) reveals some holes and islands. Linescans a1) and b1) underneath the two dimensional micrographs provide information about the step heights at the surface. The direction of the linescans is indicated by arrows in two dimensional images above. All steps are still about 2 Å high, pointing to monoatomic Ag(001) steps.

One can clearly see holes and islands at the surface and that the step edges of the terraces are roughened. Nevertheless, the linescans shown in Fig. 5.7 proof that the formed holes and islands as well as the step edges do still have monolayer (ML) height corresponding to Ag(001). The LEED patterns obtained from the substrate $Ar^+$ etched at RT still show a $(1 \times 1)$ structure. Nevertheless, a higher diffuse background compared to the pattern corresponding to the substrates $Ar^+$ etched at 200°C can be seen in Fig. 5.8.

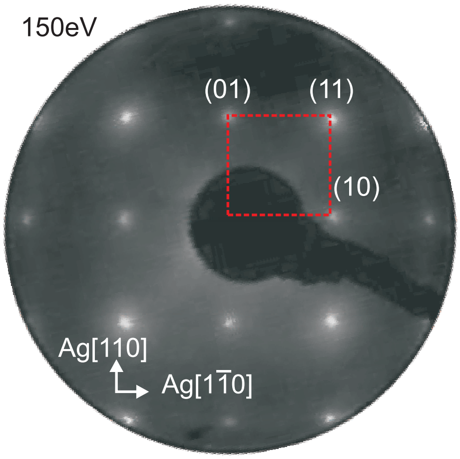

**Figure 5.8:** Diffraction pattern of the $Ar^+$ etched Ag(001) substrate at RT obtained at 150 eV. The diffuse background is higher compared to the diffraction pattern from the substrates $Ar^+$ etched at 200°C.

The higher diffuse background indicates a higher density of non periodically ordered defects at the surface. It has to be noted, that all films characterized in this work were deposited on well prepared Ag(001) substrates as shown before (cf. Chap. 5.1).

## 5.3 Post deposition annealing of Fe films on Ag(001) in UHV

The next section of this work will deal with ultra thin Fe films deposited on Ag(001) at RT. The as-deposited Fe films were investigated by AES, SPA-LEED and STM. After the examination of the Fe films, the films were annealed in UHV to determine the reported Ag segregation and its dependency on the Fe film thickness [30, 31]. This Chapter serves as a pre-investigation towards the reactive grown and post deposition annealed (PDA) iron oxide films on Ag(001).

### 5.3.1 As deposited Fe films on Ag(001)

In a first step, the absolute thicknesses of the as-deposited Fe films were calibrated with quantitative AES analysis as described in Chap. 2.5. Therefore, the normalized intensity ratio

$$\frac{\mathrm{Fe}(LMM)}{\mathrm{Ag}(MNN) + \mathrm{Fe}(LMM)} \tag{5.1}$$

including the elemental sensitivities $\sigma_i$ (cf. Chap. 2.4) was evaluated for different Fe film thicknesses. The relative film thickness was measured with an oscillating quartz in units of Hz (mass equivalent) for each Fe film (cf. Eq. 4.1).

Fe films with a mass equivalent of 50Hz to 500Hz ($\Delta$f = 50Hz) were grown to get a responsible data set for the quantitative AUGER analysis. It has to be mentioned that all Fe films were deposited on cleaned substrates, meaning that the Fe film was not grown successively. Some exemplary AE spectra are shown in Fig. 5.9.

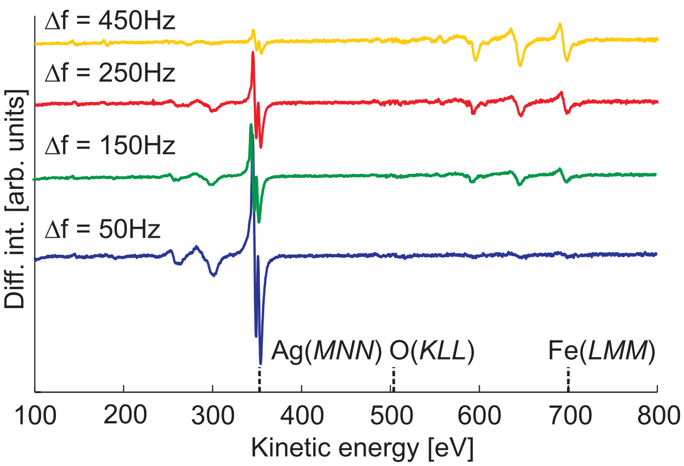

**Figure 5.9:** Some exemplary AE spectra obtained from Fe films of different thickness on Ag(001). The Fe($LMM$)(703eV) and the Ag($MNN$)(351eV) AUGER transitions are indicated by dashed lines. There is no contamination (e.g. O($KLL$)(503eV)) visible.

One can see that the Ag($MNN$)(351eV) signal decreases while the Fe($LMM$) (703eV) signal increases with increasing Fe coverage. In addition, there was no contamination (e.g. O($KLL$)(503eV)) of the films found in any AE spectra. These spectra (and the ones not shown here) were used to determine the absolute Fe coverage via Eq. 2.69. The resulting curve of relative AUGER intensities over film thickness is shown in Fig. 5.10.

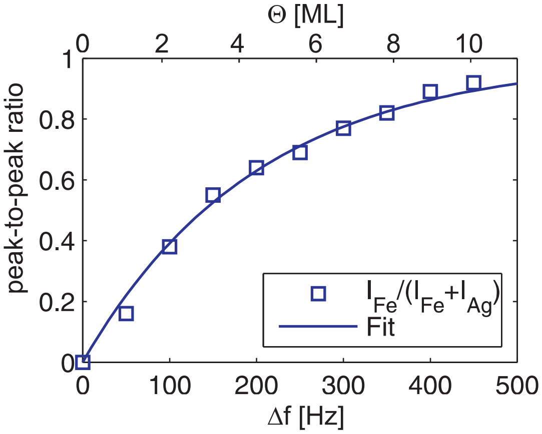

**Figure 5.10:** Normalized intensity ratio between the Fe($LMM$)(703eV) and the Ag($MNN$)(351eV) signal including the sensitivities $\sigma_i$ over coverage. The coverage in ML was calculated from Eq. 2.69.

From the curve fit in Fig. 5.10 the absolute Fe film thicknesses were calculated (upper horizontal axis). As explained in Chap. 2.5 this quantitative AES analysis is only exact for layer-by-layer growing Fe films. It is known from other studies that Fe tends to grow as three dimensional islands on Ag(001) for the first few monolayers [37, 38]. Nevertheless, the shown quantification can serve as a first clue to estimate the coverage from the Fe films as it will be shown in the following.

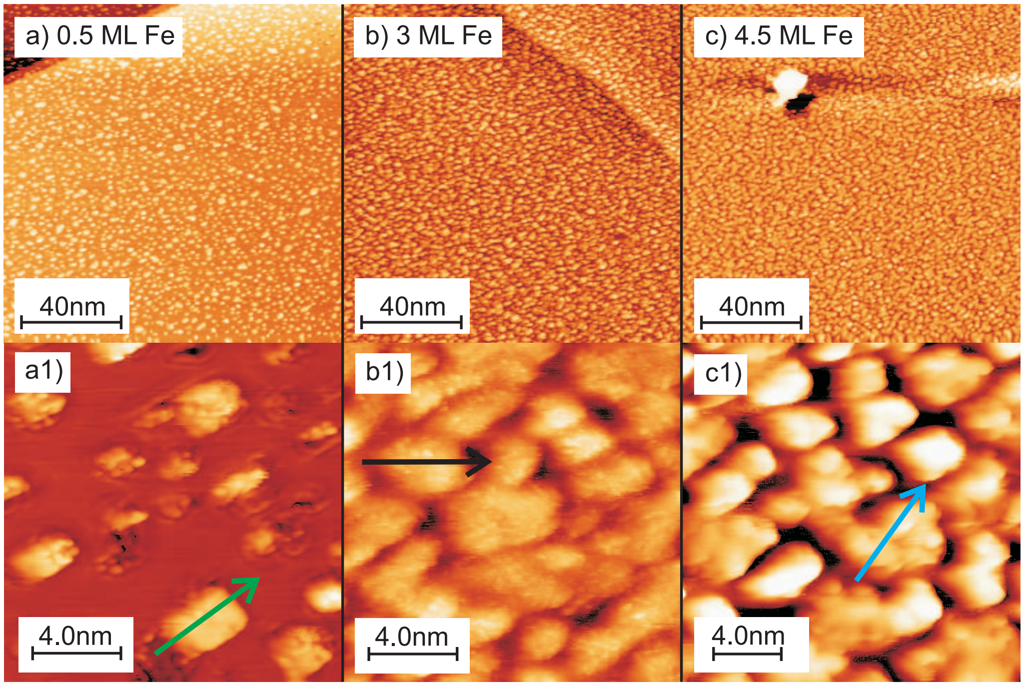

**Figure 5.11:** STM micrographs of the a) 0.5 ML Fe film, the b) 3 ML Fe film and the c) 4.5 ML Fe film. Bias voltage is 1 V, tunneling current is 1 nA.

After calibration of the film thickness we produced a 0.5 ML, a 3 ML and a 4.5 ML Fe film (calibrated after deposition with XPS (cf. end of Chap. 2.5)) on Ag(001) substrates in UHV chamber #1 and performed STM measurements. Fig. 5.11 gives an overview of the surface structure of the 0.5 ML, the 3 ML and the 4.5 ML Fe film as observed with STM.

It can be seen, that the Fe films do not completely wet the substrate but grow in three dimensional islands in a more or less columnar growth mode. The islands of the 0.5 ML Fe film have no preferred accumulation sites, like step edges and seem to grow randomly distributed over the surface. These Fe islands have a homogeneous height of 2.6 Å (cf. Fig 5.12 a)) while the surface is about 30% covered by the Fe islands. Considering a Fe(001) layer distance of $d_{\mathrm{Fe}(001)} = 1.44$ Å this leads to an effective coverage of 0.5 ML in agreement to XPS.

The Fe islands of the 3 ML and the 4.5 ML Fe film, however, are densely packed with diameter of $(5 \pm 1)$nm while the size of the boundaries between the islands is $(1 \pm 0.5)$nm for both films. This boundaries lead to an effective coverage of 80% for these films. Only the height of the islands differs from 4.8 Å for the 3ML film to 6.8 Å for 4.5ML film (cf.

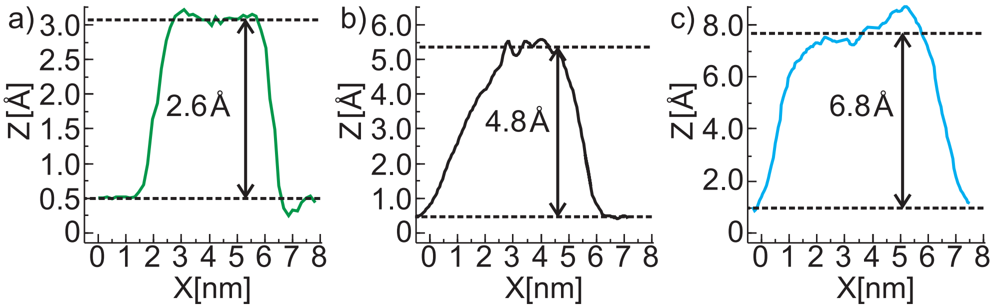

**Figure 5.12:** Linescans obtained from the STM micrographs shown in Fig 5.11. a) 0.5 ML, b) 3 ML and c) 4.5 ML. The directions of the linescans are indicated by correspondingly colored arrows in Fig 5.11.

Fig 5.12 b) and c)). This is in agreement with the deposited amount of Fe in both cases assuming, that the trenches reach down to the Ag substrate.

Even though the Fe film does not grow as a flat layer on the Ag(001) substrate as implied in the AES analysis above, the homogeneous shape of the islands and the high effective coverage justify this assumption. The shape of the step edge of the Ag substrate seems not be significantly influenced by the deposited Fe comparing Fig. 5.11 a) and b) to Fig. 5.5. Finally, there is a cluster visible in Fig. 5.11 c) which will not be further regarded in the following.

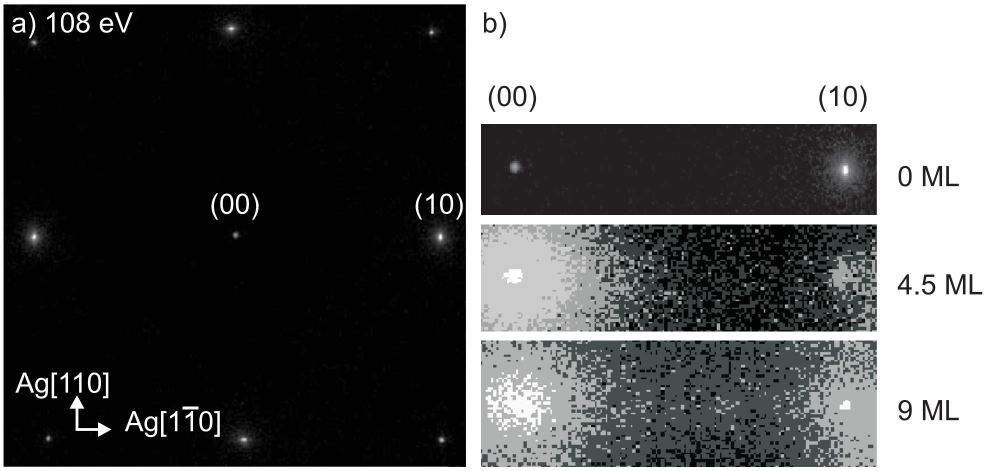

**Figure 5.13:** a) Diffraction pattern from the cleaned Ag(001) substrate for comparison. b) Outcuts of the diffraction patterns obtained from the as-deposited 4.5 ML and 9 ML Fe films. Electron energy was always 108 eV.

Since STM gives only an impression about local structures at the surface we also produced a 4.5 ML and a 9 ML Fe film in UHV chamber #2 and investigated them by SPA-LEED in order to observe the changes in surface structure and morphology in dependency on the increasing Fe coverage. Fig. 5.13 shows cutouts of the diffraction patterns obtained from the as-deposited Fe films at 108 eV.

The cutouts of the diffraction patterns obtained from the 4.5 ML and the 9 ML Fe film in Fig. 5.13 b) show very weak diffraction spots of (1 × 1) structures. This points to (at least partial) formation of Fe(001). Nevertheless, the intensity of the diffraction spots is quite low compared to the background which indicates a large amount of point defects in the as grown Fe(001) films and a loss of crystallinity.

### 5.3.2 Annealing in UHV

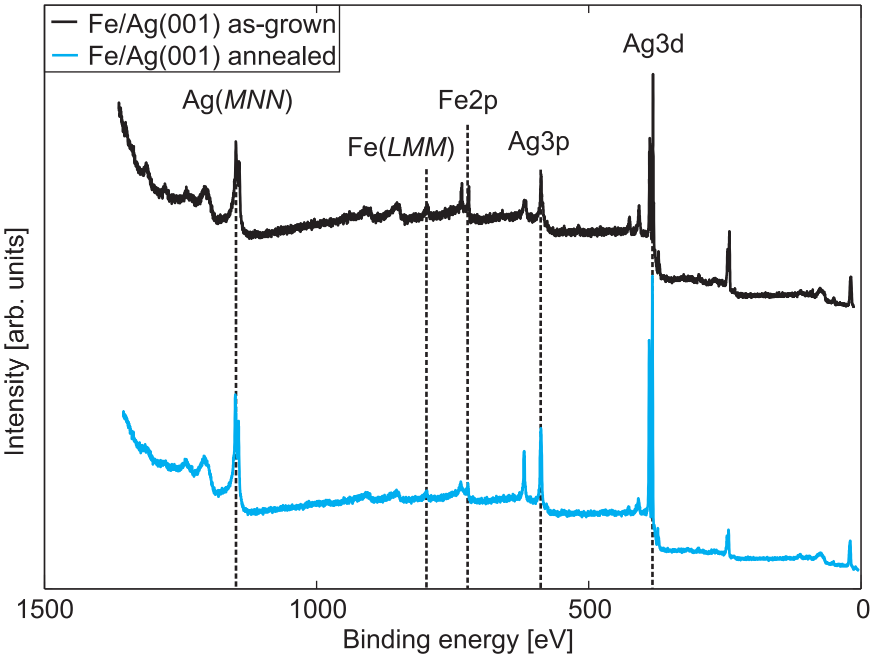

**Figure 5.14:** XP spectra of the as-grown and the annealed 3 ML Fe film. The positions of the Ag and Fe Auger transitions as well as photoemission peaks are indicated by dashed lines.

After investigating the as-deposited Fe films we annealed the films in UHV (cf. Chap. 4.7) at 300°C for 50 minutes and analyzed the samples with AES, XPS, STM, LEED and SPA-LEED afterwards. First, the XP spectra of the 3 ML Fe film before and after annealing in UHV are presented in Fig. 5.14.

It can be seen that the Fe signals (Fe($LMM$) and Fe2p) have decreased, while the Ag signals (Ag($MNN$), Ag3d and Ag3p) increased upon annealing the film in UHV. This effect can be attributed either to de-wetting of Fe islands during annealing or to segregating Ag which was reported several times for temperatures above 250°C [30, 31]. The Ag/Fe ratio at the surface can be estimated from the areas under the Fe2p and Ag3d peak including the element specific cross sections (cf. Chap. 2.5). This results in Ag/Fe=3:1 prior to annealing and Ag/Fe=5:1 after annealing in UHV.

A LEED pattern at 108 eV of the UHV annealed 3 ML Fe film is shown in Fig. 5.15.

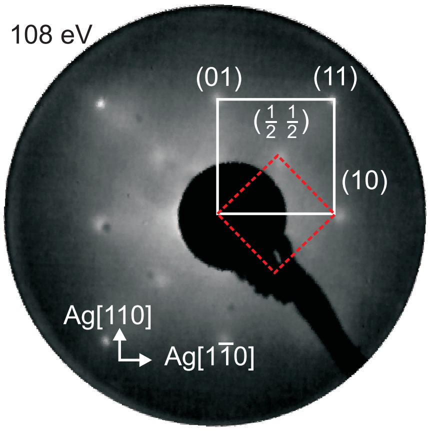

**Figure 5.15:** LEED pattern of the UHV annealed 3 ML Fe film at 108 eV. The diffraction pattern shows a clear $(1 \times 1)$ structure (white square) as well as a $(\sqrt{2} \times \sqrt{2})$R45° superstructure (dashed, red square).

The diffraction pattern shows a clear $(1 \times 1)$ structure as well as a $(\sqrt{2} \times \sqrt{2})$R45° superstructure. Although the fundamental diffraction spots can also result from a $(\sqrt{2}\times\sqrt{2})$R45° superstructure, we assume that the diffraction pattern is a superposition of a $(1 \times 1)$ and a $(\sqrt{2} \times \sqrt{2})$R45° structure. Possibly, the $(1 \times 1)$ structure is the result of a well ordered Ag film, which segregates at the surface during annealing, as suggested by XPS and reported before [30, 31].

In order to analyze the changes in surface structure due to UHV annealing of the 3 ML Fe film in more detail we also performed STM measurements at RT. Some exemplary STM images of different magnification are presented in Fig. 5.16 to give an overview of the film surface structure.

Clearly, the surface structure changed drastically compared to the as-deposited Fe films (cf. Fig. 5.11). The column-shaped Fe islands are gone and the surface can be broken down into three elements. 1) large, almost square-shaped islands with small clusters on top (cf. blue, dashed circles) , 2) branched clusters (cf. red, dashed circles) and 3) atomically flat areas in between. These atomically flat areas show square surface symmetry on an atomic scale as shown in Fig. 5.16 d). No $(\sqrt{2} \times \sqrt{2})$R45° superstructure observed by LEED was detected on any of the atomically flat areas.

The step edges of these flat areas are oriented either along Ag[110] or Ag[1$\bar{1}$0] direction. We also present a linescan perpendicular to such a step edge in Fig. 5.17 a). The step height resulting from the linescan is 2 Å which corresponds to the step height of Ag(001).

The almost rectangular islands do all have a similar apparent height of about 5 Å (cf. Fig. 5.18), while the branched clusters reveal heights of $2 - 3$ Å.

We did not observe a $(\sqrt{2} \times \sqrt{2})$R45° superstructure on these structures. However, this might be a result of the cluster-like surface on these structures, since it is very hard to

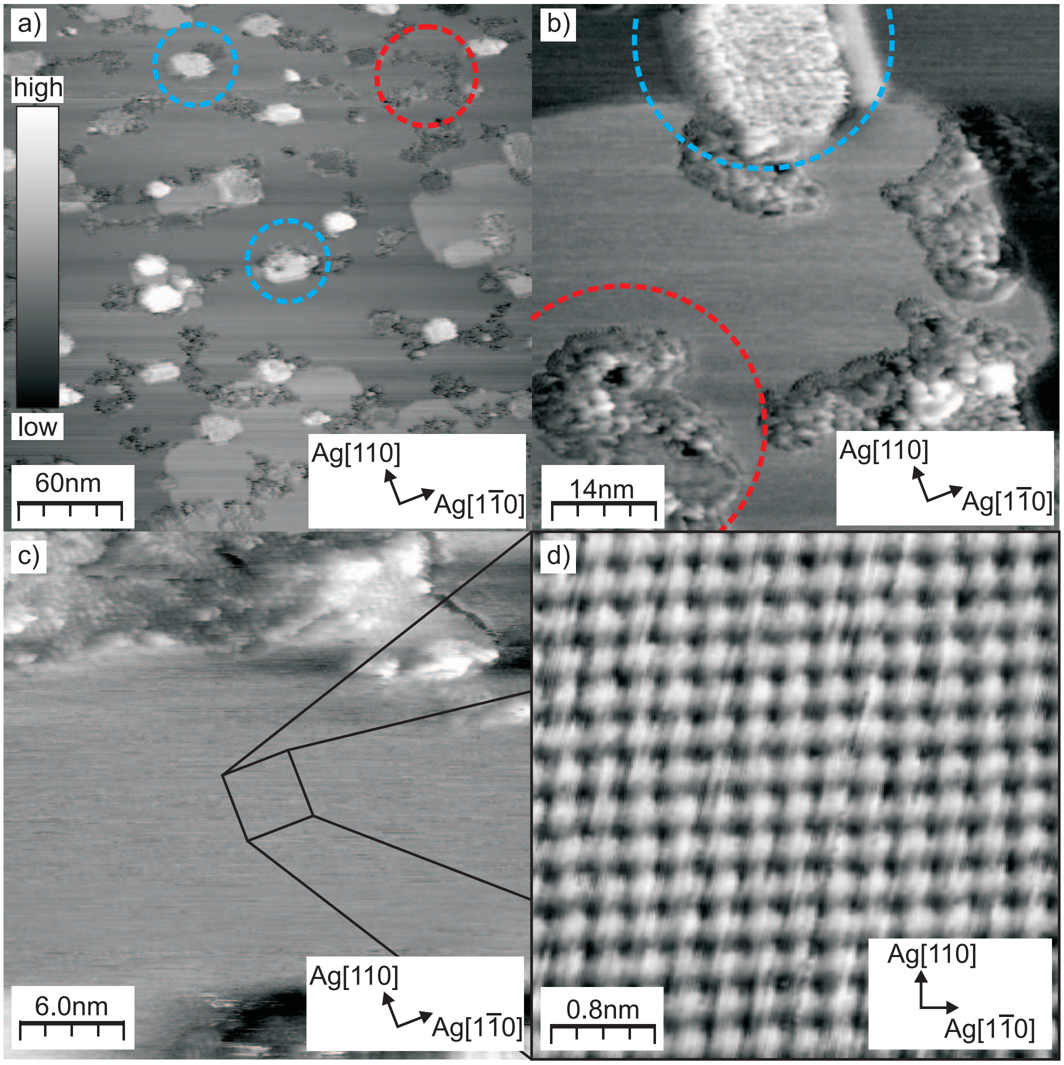

**Figure 5.16:** STM images of the 3 ML Fe film after annealing in UHV. Bias voltage and tunneling current are 0.3 V and 1 nA for a), b) and c), while it is 50 mV and 2 nA for d). Some islands and some branched clusters are marked by blue, dashed circles or red, dashed circles, respectively. The enlarged area in d) is indicted in c). An exemplary color map is shown in **a)**

get to atomic resolution with an STM on highly three dimensional surfaces. Considering the height of the islands of about 5 Å and their three dimensional surface, we assume that these islands are residual Fe at the surface (cf. Fe islands in Fig. 5.11). Hence, the Fe islands from the as-deposited 3 ML film did affiliate to larger, separated Fe islands upon UHV annealing. Nevertheless, the height of the Fe islands does not differ from the height of the as-deposited Fe islands (see above). A linescan of an atomically flat area is presented

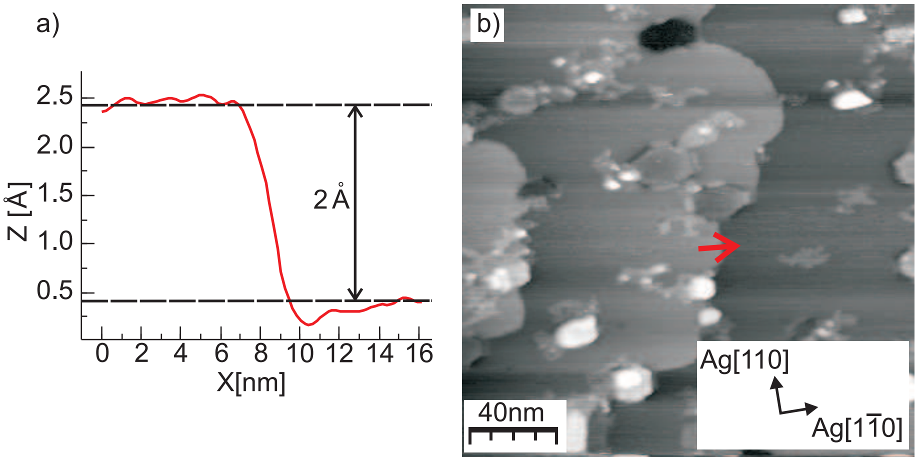

**Figure 5.17: a)** Linescan perpendicular to a step edge of the atomically flat area taken from **b)** ($V = 0.3\,\text{V}\,, I = 1\,\text{nA}$). The direction of the linescan is indicated by a red arrow.

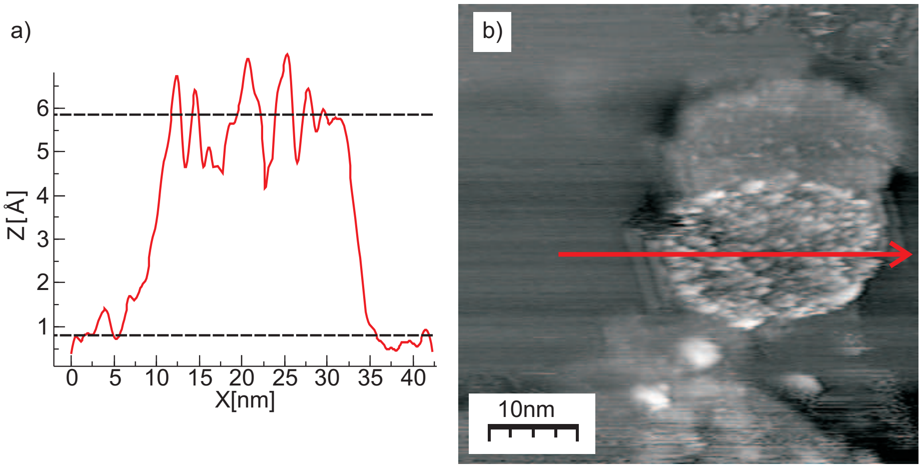

**Figure 5.18: a)** Linescan over an almost rectangular island. The height of the island is about 5 Å and diameter is 27 nm. Bias voltage and tunneling current are $U = 260\,\text{mV}$ and $I = 1.4\,\text{nA}$. The linescan is a cutout from the micrograph presented in **b)**.

in Fig. 5.19 b).

Since the lattice mismatch between Fe and Ag is only 0.7 %, the measured atomic distance of 2.9 Å can correspond to either Fe(001) or Ag(001). In agreement to the strong increase of Ag at the surface after annealing in UHV (cf XPS above) and the step height of 2 Å at the edges of the atomically flat areas, we assume that these areas are Ag(001). This is supported by comparison of surface free energies of Fe(001) and Ag(001), since Fe(001) grows in Volmer-Weber mode on Ag(001) (see above) it is likely that Ag(001) wets

Fe(001) (colloquially known as *'Murphys law of epitaxy'*).

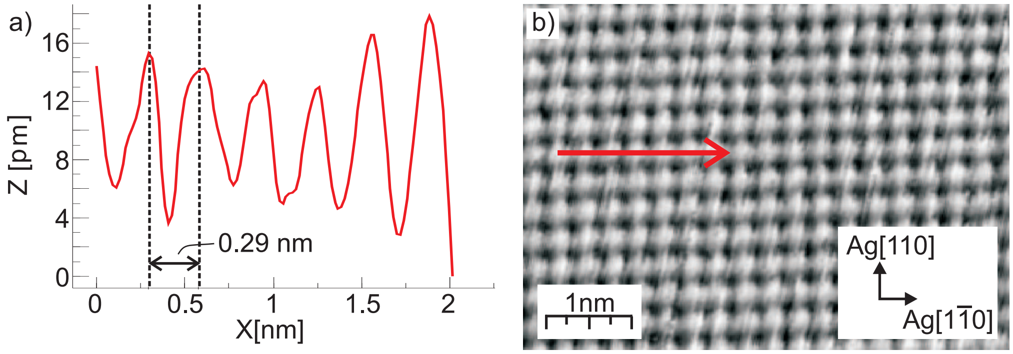

**Figure 5.19:** **a)** Linescan along an atomic row taken from **b)** ($V = 0.05\,\mathrm{V}\,, I = 2\,\mathrm{nA}$). The direction of the linescan is indicated by a red arrow. The STM image in **b)** is taken from a flat area at the surface of the UHV annealed 3 ML Fe film.

Comparing the size of the residual Fe islands to the flat Ag(001) areas in relation to the deposited amount of 3 ML Fe prior to UHV annealing, it is likely that a large amount of iron is buried under the well ordered Ag(001) film. Furthermore, the Ag:Fe ratio expected from the STM measurements would be about 10:1. Since the actual Ag:Fe ratio (determined by XPS) is only 5:1, this points to the presence of iron underneath the segregated Ag film. A thermal desorption of iron can be excluded at annealing temperatures of 300°C.

We also prepared UHV annealed 4.5 ML and 9 ML Fe films in UHV chamber #2 to do SPA-LEED measurements on the $(\sqrt{2} \times \sqrt{2})$R45° superstructure observed in the LEED pattern (see above) in order to quantify the surface structure in more detail. Before showing the SPA-LEED results, we present AES measurements of the Fe films before and after annealing in UHV to guarantee a similar sample preparation as before.

The AE spectra of the 4.5 ML and 9 ML Fe film (before and after annealing) are shown in Fig. 5.20.

The peak-to-peak intensities of the Fe($LMM$)(703eV) and the Ag($MNN$)(351eV) signal increase after annealing at 250°C for 50 minutes for both Fe films. The $I_{\mathrm{Ag}} : I_{\mathrm{Fe}}$ peak-to-peak ratio including the sensitivities $\sigma_i$ prior to annealing results in 0.6:1 for the 4.5 ML film and 0.1:1 for the 9 ML film, respectively (cf. Fig. 5.20). After annealing the ratio increases to 1.5:1 for the 4.5 ML film and 0.8:1 for the 9 ML film. This increase of Ag at the surface is in agreement with the XPS measurements of the 3 ML Fe film.

The SPA-LEED diffraction patterns obtained from the 4.5 ML and 9 ML Fe films after annealing at 250°C for 50 minutes show clear $(1 \times 1)$ structures (cf. Fig. 5.21).

This matches the LEED pattern of the 3 ML Fe film shown before and indicates well ordered segregated Ag films in agreement to the STM results presented above. The diffraction spots still have a large FWHM ($\approx 10\,\%$BZ for the 4.5 ML film and $\approx 16\,\%$BZ for the 9 ML film) which again points to smaller grain sizes compared to the clean Ag(001) substrate. Additionally, both diffraction patterns show a weak $(\sqrt{2} \times \sqrt{2})$R45° superstructure as it

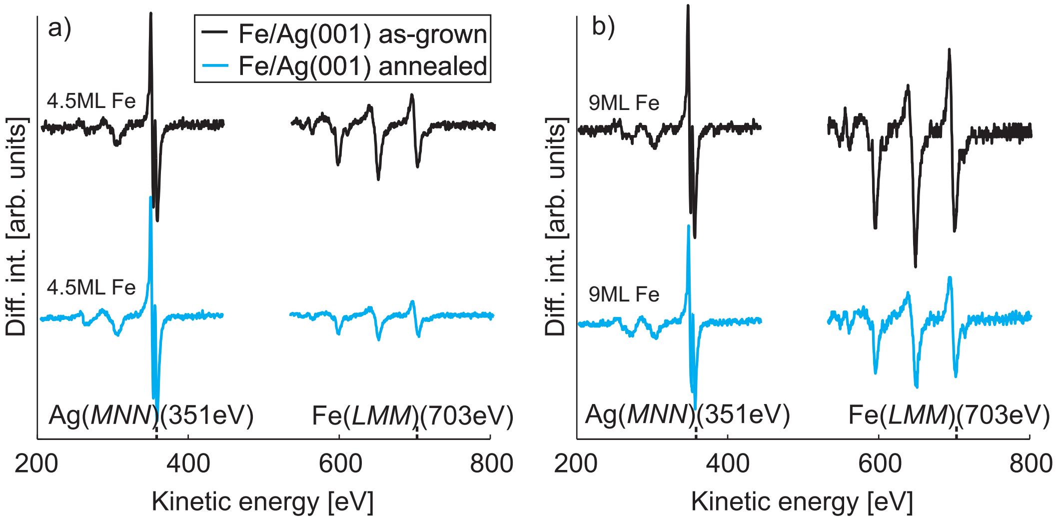

**Figure 5.20:** AE spectra of the as-grown and the annealed 4.5 ML (a) and 9 ML (b) Fe films, respectively. The positions of the Ag($MNN$) and the Fe($LMM$) transition are indicated by small dashed lines.

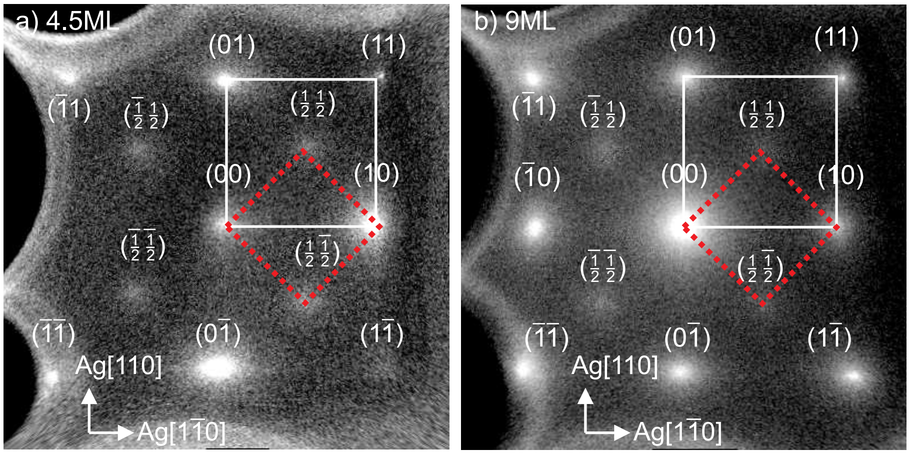

**Figure 5.21:** two dimensional Diffraction pattern of a) the 4.5 ML Fe film and b) the 9 ML Fe film after annealing at 250°C. Electron energy is 144eV. Both films show clear $(1 \times 1)$ diffraction pattern and an additional $(\sqrt{2} \times \sqrt{2})$R45° superstructure.

was also seen in the prior shown LEED pattern.

Fig. 5.22 shows linescans of the (00) diffraction spot of the annealed Fe films and the Ag(001) substrate at an electron energy of $E = 144\,\mathrm{eV}$ which corresponds to an in-phase condition of Ag(001).

The spot profiles were again fitted by two LORENTZIANS describing the central peak and the diffuse shoulder, respectively (cf. description above). An increase of the FWHM of

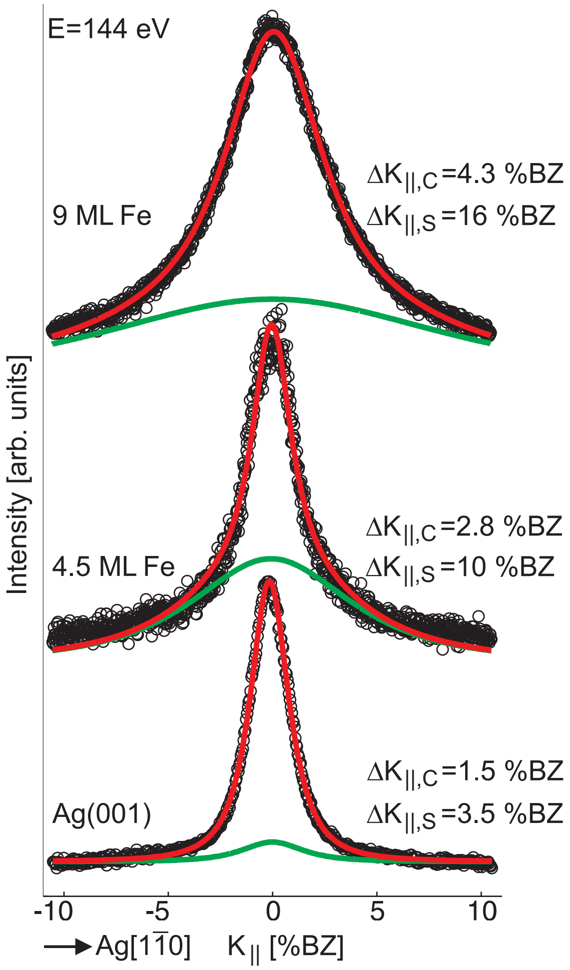

**Figure 5.22:** Linescans of the (00)-spot obtained from the clean Ag(001) substrate, the 4.5 ML Fe film and the 9 ML Fe film after annealing in UHV. Electron energy is 144 eV for all measurements. $\Delta K_{||,S}$ and $\Delta K_{||,C}$ indicate the FWHM of the diffuse shoulder (green, solid line) and of the central spot, respectively.

both central peak and diffuse shoulder of the (00) spot can be observed with increasing film thickness pointing to an increasing defect density.

We also performed (00)-spot profile measurements of the 9 ML Fe film during the entire annealing process. The electron energy was constantly 74 eV which corresponds to an in-phase condition of Fe(001). Thus, the diffraction experiment is sensitive e.g. to grain sizes but not to atomic steps of Fe. Three exemplary line scans of the (00) spot recorded after different annealing times are shown in Fig. 5.23 a) for comparison.

The spot profiles were again fitted by two LORENTZIAN functions. The first LORENTZIAN described the central peak of the profile using a constant FWHM of 3 %BZ. The second LORENTZIAN described the diffuse shoulder of the spot profile. Fig. 5.23 b) presents the FWHM evolution of the diffuse shoulder over annealing time.

At t=0 the FWHM of the diffuse shoulder is 26 %BZ which decreases during the annealing procedure and stagnates at a value of 16 %BZ after approximately 30 minutes. Further annealing had no influence on the FWHM of the shoulder. This is in agreement with the two dimensional diffraction patterns presented in Fig. 5.13 and Fig. 5.21 and indicates the reduction of defects at the surface during annealing.

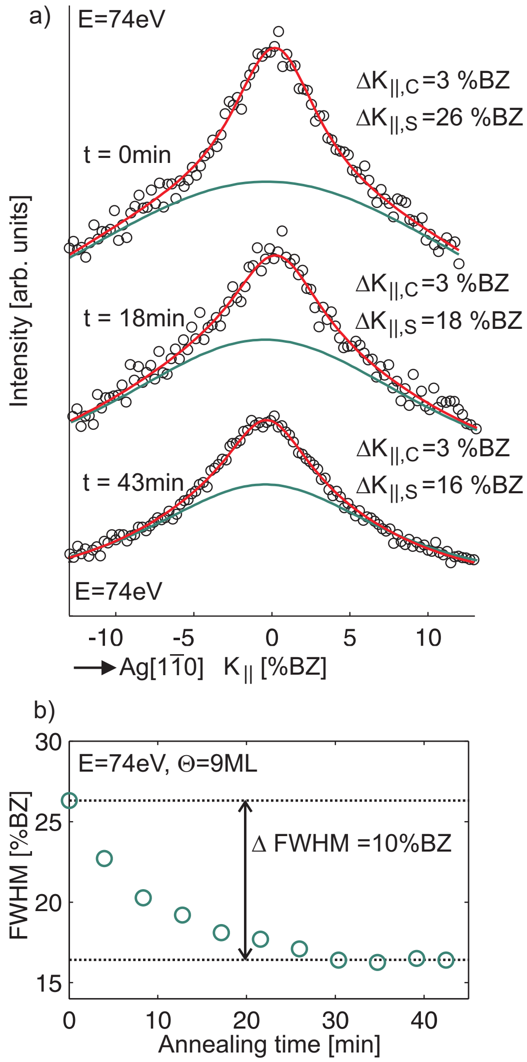

**Figure 5.23:** a) Exemplary linescans of the (00) spot of the 9 ML Fe film after annealing at t=0, 18 and 43 minutes. The diffuse shoulder is displayed by a green LORENTZIAN for comparison. b) Evolution of the FWHM of the diffuse shoulder of the (00) spot during annealing over time. Electron energy is 74 eV.

From the FWHM behavior of the central peak (of the (00) diffraction spot) in dependence on the electron energy one can also get information about average terrace widths, layer distances and mosaic spreads (cf. Chap. 2.2.3). Therefore, we analyzed this behavior for the prepared Ag(001) substrate as well as for the 4.5 ML and the 9 ML Fe(001) films after annealing. Assuming that the diffuse shoulder is caused by inhomogeneities its FWHM has to be constant [47]. This assumption is in agreement with our spot profile analysis.

Thus we observed the evolution of FWHM of the central peak over electron energy. As expected for the case of epitaxial grown films with formation of atomic steps the FWHM of the central peak oscillates with the electron energy. Fig. 5.24 presents the dependence of FWHM of the central peak on the scattering phase $S$ corresponding to Ag(001).

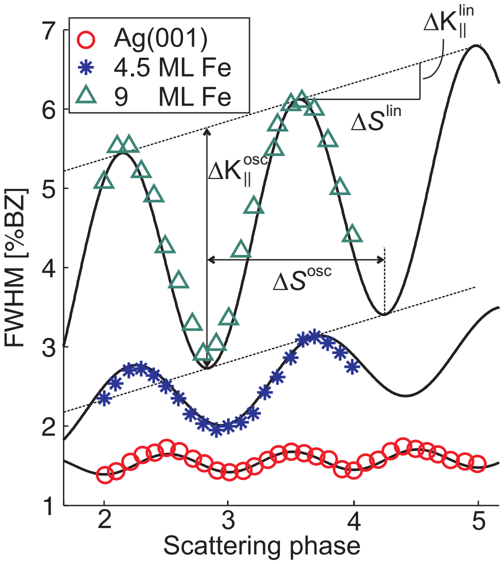

**Figure 5.24:** H(S) analysis of the clean Ag(001) substrate, the 4.5 ML and the 9 ML Fe(001) film after UHV annealing. The values used for the quantitative H(S) analysis (see below) are exemplary marked for the 9 ML Fe(001) film.

One can see that the FWHM oscillates with $S$ for substrate and both annealed Fe(001) films. This reflects the strong increase of order at the surface after annealing at 250°C. The increased crystallinity (appearance of (1 × 1) diffraction pattern) is accompanied by formation of atomic steps that cause the oscillation of the FWHM of the central spot.

It has to be noted that the expected minimal FWHM for step heights of bulk Ag(001) and Fe(001) are very good reflected by the curves of the clean Ag(001) substrate and the annealed 9 ML Fe film, respectively (cf. Fig. 5.24). Obviously, the mosaic spread increases for increasing film thickness, although, even for the 9 ML Fe(001) film its value is only $\Delta\vartheta = 0.073°$ and therefore almost negligible. The average terrace width decreases more drastically with increasing Fe coverage from 40 nm for the clean Ag(001) substrate to 4.6 nm for the 9 ML Fe film. The detailed values resulting from this analysis are presented in Tab. 5.1.

| | $\Delta\vartheta$ | $\Gamma$ | d |
|---:|---|---|---|
| Ag(001) | 0.007° | 80nm | 2.04 Å |
| 4.5 ML Fe(001) | 0.038° | 15nm | 1.38 Å |
| 9 ML Fe(001) | 0.073° | 4.6nm | 1.44 Å |

**Table 5.1:** Resulting values from the H(S) analysis presented in Fig. 5.24 for the mosaic spread $\Delta\vartheta$, the average terrace width $\Gamma$ and the step height d.

### 5.3.3 Discussion

The as-grown Fe films consist of three dimensional, column-shaped islands of the same size. The weak (1 × 1) structure in the diffraction patterns of the 4.5 ML and the 9 ML

Fe film indicate that the islands (at least partially) consist of low ordered Fe(001). This is in agreement with former studies concerning the epitaxial growth of iron on Ag(001) [37, 93]. The thin Fe(001) films on Ag(001) undergo a strong change in structure and morphology upon annealing in UHV at 250°C. The diffraction patterns from the annealed Fe(001) films point to an increase of order at the surface during the annealing process (cf. Fig. 5.21). Nevertheless, the average domain size (also denoted as $\Gamma$ in Tab. 5.1) of the annealed Fe films is still significantly smaller than the average terrace width $\Gamma$ of the prepared substrate. However, it is known from former studies that annealing temperatures above 250°C lead to a great amount of segregated Ag [30, 31]. This was already observed in our experiments by XPS and AES showing increasing Ag signals after annealing the films in UHV (cf. Fig. 5.20 and Fig. 5.14). Also the diffraction patterns of the annealed Fe films reveal an additional weak $(\sqrt{2} \times \sqrt{2})$R45° superstructure. This might be a result of surface segregating Ag, since other studies reported an Ag-adatom exchange during UHV annealing of ultra thin Fe films on Ag(001) [31]. This adatom exchange would lead to the observed $(\sqrt{2} \times \sqrt{2})$R45° superstructure, which is illustrated in Fig. 5.25.

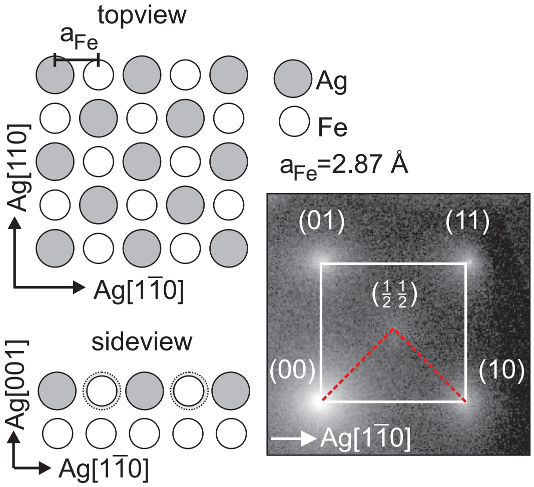

**Figure 5.25:** Schematic drawing of the reported $(\sqrt{2}\times\sqrt{2})$R45° superstructure induced by atomic site exchange as suggested by Ref. [31]. This site exchange would lead to the observed additional $(\frac{1}{2}\frac{1}{2})$ spots in the diffraction pattern (cutout) shown for comparison.

Nevertheless, we did not observe a $(\sqrt{2}\times\sqrt{2})$R45° superstructure on the flat terraces of the UHV annealed films via STM. Therefore, we can not give any evidence for the correctness of the model suggested in [31]. In our case, the flat terraces show a square atomic $(1 \times 1)$ structure with a next neighbor distance of 2.9 Å. In connection with the XPS and AES results, this $(1 \times 1)$ structure points to the segregation of well ordered Ag(001) areas during annealing of the Fe films. It is possible that the $(\sqrt{2} \times \sqrt{2})$R45° superstructure observed in the diffraction experiments is located on the small rectangular islands or the branched clusters (cf. Fig. 5.16), which we assume to be of Fe. This would agree with the weak corresponding diffractions spots, that point to a low order in the superstructure. However, we were not able to get to atomic resolution in the STM measurements of those strongly three dimensional (Fe) islands and clusters. Nevertheless, the Fe in these islands and branched structures is much less than expected from the AES and XPS measurements. Hence, Fe might be buried underneath the flat Ag(001) areas. This assumption is supported by the lower free energy of an Ag(001)/Fe(001) interface compared to the the free energy of the Fe(001) surface (cf. Fig. 3.6). Thus, a buried Fe film between a Ag(001) substrate and a segregated Ag(001) film would be energetically favorable. It is therefore questionable whether the former reported Ag segregation at the Fe surface can rather be described as a Fe diffusion into the Ag substrate. We would like to note, that the $(\sqrt{2} \times \sqrt{2})\mathrm{R}45^\circ$ superstructure observed in the diffraction patterns has not been reported in connection to the segregation of Ag on UHV annealed Fe films on Ag(001) before.

## 5.4 Post deposition annealing of Fe films on Ag(001) in $O_2$ atmosphere

As a pre-investigation, we deposited very low amounts of Fe (0.05 ML estimated by STM) on the clean Ag(001) substrate and annealed it in molecular oxygen as explained above. Here, the influence of deposited iron on the reactivity between the Ag(001) surface and the oxygen was studied. Afterward Fe films of 0.5 ML, 3 ML and 4.5 ML thickness were deposited on Ag(001) and annealed (300°C for 1h) in an oxygen atmosphere ($10^{-5}$ mbar) as described in Chap. 4.7. Here, it is important to mention that the Fe films were exposed to the oxygen prior to heating in order to prevent Ag diffusion as reported in Chap. 5.3 and in former studies [30, 31]. The changes in surface structure and morphology were studied in detail by LEED and STM. The absolute film thickness of the Fe films was calibrated by quantitative XPS.

### 5.4.1 Annealing of very low Fe coverages in $O_2$ atmosphere

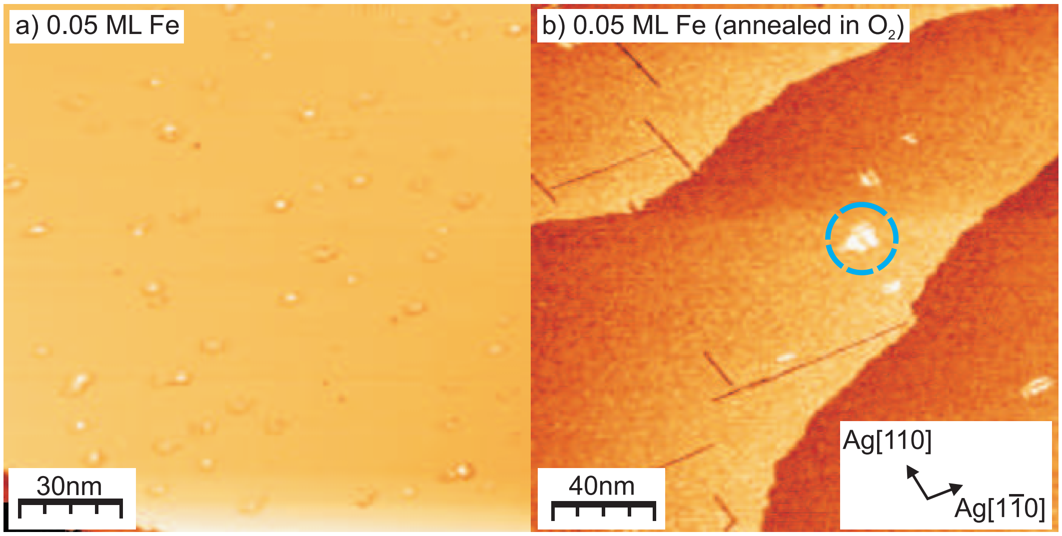

**Figure 5.26:** STM images of the **a)** as-deposited and the **b)** $O_2$ annealed 0.05 ML Fe film ($V = 0.4\,\mathrm{V}$, $I = 1\,\mathrm{nA}$). The Fe clusters disappeared after annealing and the surface shows trenches in Ag[110] and Ag[1$\bar{1}$0] direction. Some islands at the annealed surface are indicated by a blue, dashed circle.

In a first step, we deposited 0.05 ML of Fe on a clean Ag(001) substrate and analyzed the changes in surface structure upon annealing in $O_2$ atmosphere at 300°C.

Fig. 5.26 shows STM micrographs of the 0.05 ML Fe film before and after annealing.

It can be seen that the few Fe clusters of the as-deposited film disappeared and only some small accumulations remain at the surface (cf. blue, dashed circle). Compared to the deposited amount of Fe the few small accumulations can not contain the whole deposited Fe (estimated from several STM images). Hence, it is possible that the Fe gets incorporated into the silver surface during annealing in oxygen. A thermal desorption of Fe due to annealing can be excluded at temperatures around 300°C. Since Ag diffusion has been reported for UHV annealed Fe films [30, 31], this might be not too surprising. Nevertheless, this possible Fe-Ag interdiffusion will be addressed later in the discussion.

The annealed surface exhibits long trenches either along Ag[110] or Ag[$1\bar{1}0$] direction. The trenches all have a homogeneous width of $2-3\,\mathrm{nm}$ as can be seen in Fig. 5.27.

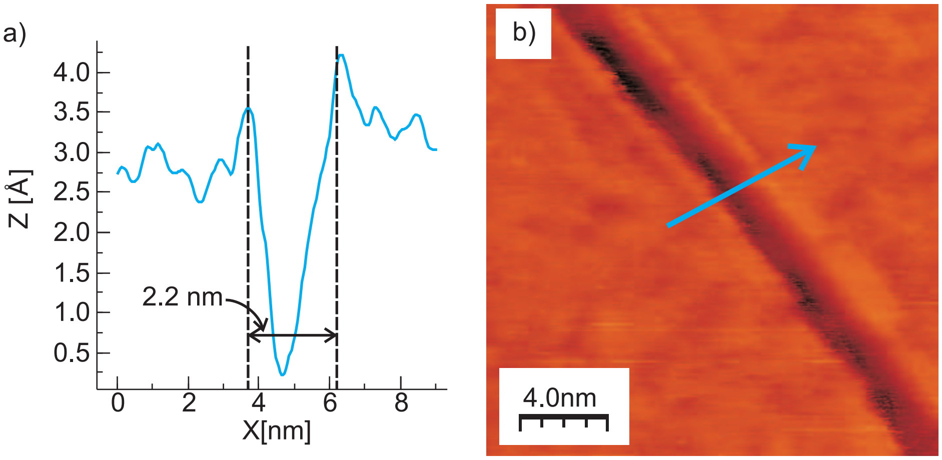

**Figure 5.27: a)** Linescan perpendicular to a trench taken from the STM image shown in **b)**.

It is unlikely that the trenches are domain boundaries of outspreading Fe islands due to the very low amount of Fe deposited on the surface. Furthermore, the surface seems to be roughened compared to atomically flat Ag(001) surface after preparation (cf. Fig. 5.27 b)). This indicates that the presence of small amounts of Fe at the Ag(001) surface has a significant influence on the reactivity between the Ag(001) substrate and the surrounding oxygen. This has to be kept in mind for interpretation of further experimental data and will be discussed later.

### 5.4.2 Electron diffraction

After this preliminary investigations, we deposited Fe films of 0.5 ML, 3 ML and 4.5 ML thickness on Ag(001) and annealed the films in an oxygen atmosphere, as described above. LEED images of these oxidized Fe films are presented in Fig. 5.28.

The diffraction pattern from the oxidized 0.5 ML film (Fig. 5.28 a)) shows a (1 × 1) structure. The intensity of the diffraction spots in this pattern has increased compared to the as-deposited 0.5 ML Fe film (cf. Fig. 5.13). Also, there are very weak streaks in Ag[$1\bar{1}0$] and Ag[110] direction visible in the diffraction pattern pointing to a low ordered superstructure with small domains in these directions. These streaks are more pronounced in the diffraction patterns of the oxidized 3 ML and the 4.5 ML film (cf. Fig. 5.28 b) and c))

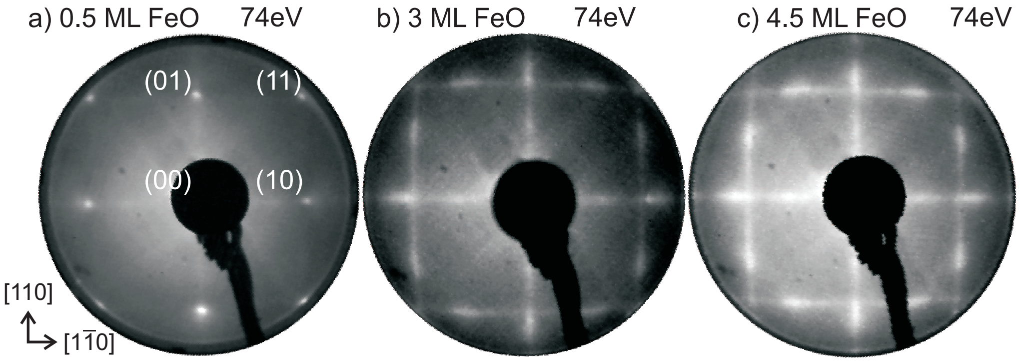

**Figure 5.28:** LEED patterns of the 0.5 ML, 3 ML and 4.5 ML Fe films annealed in $10^{-5}$ mbar $O_2$. Electron energy is 74 eV and the directions in reciprocal space corresponding to bulk Ag are indicated in the lower left corner of the patterns. The patterns from the 3 ML and 4.5 ML films reveal a quasi-hexagonal $(1 \times 1)$ structure and another weak superstructure (streaks) in Ag[1$\bar{1}$0] and Ag[110] direction.

indicating an increasing amount of the superstructure at the surface. However, a certain periodicity of this low ordered superstructure can not be determined by LEED.

Furthermore, Fig. 5.28 b) and c) show two quasi-hexagonal structures rotated by 90° against each other. The diffraction spots of this hexagonal structure are elongated either along the Ag[1$\bar{1}$0] or the Ag[110] direction, respectively. Finally, the diffuse background is quite high in all three diffraction patterns pointing to a high point defect density in the oxidized Fe films. For visibility we present a schematic drawing of the diffraction patterns in Fig. 5.29.

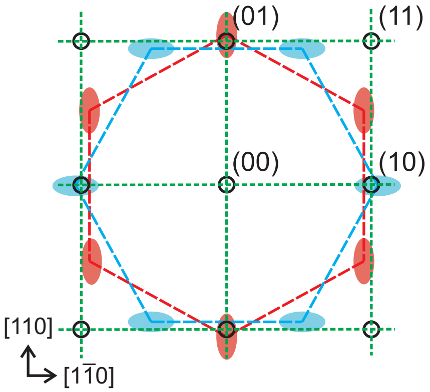

**Figure 5.29:** Schematic drawing of the diffraction patterns observed from the 3 ML and the 4.5 ML film. The $(1 \times 1)$ structure is indicated by black circles, the streaks in Ag[1$\bar{1}$0] and Ag[110] direction are marked by dotted, green lines and the two quasi-hexagonal structures rotated by 90° are shown by dashed, red and blue quasi-hexagons.

### 5.4.3 Scanning Tunneling Microscopy

We also performed STM measurements on the films after annealing in oxygen atmosphere to get more information about the surface structure and morphology. Fig. 5.30 shows STM micrographs of the oxidized 0.5 ML, 3 ML and 4.5 ML film.

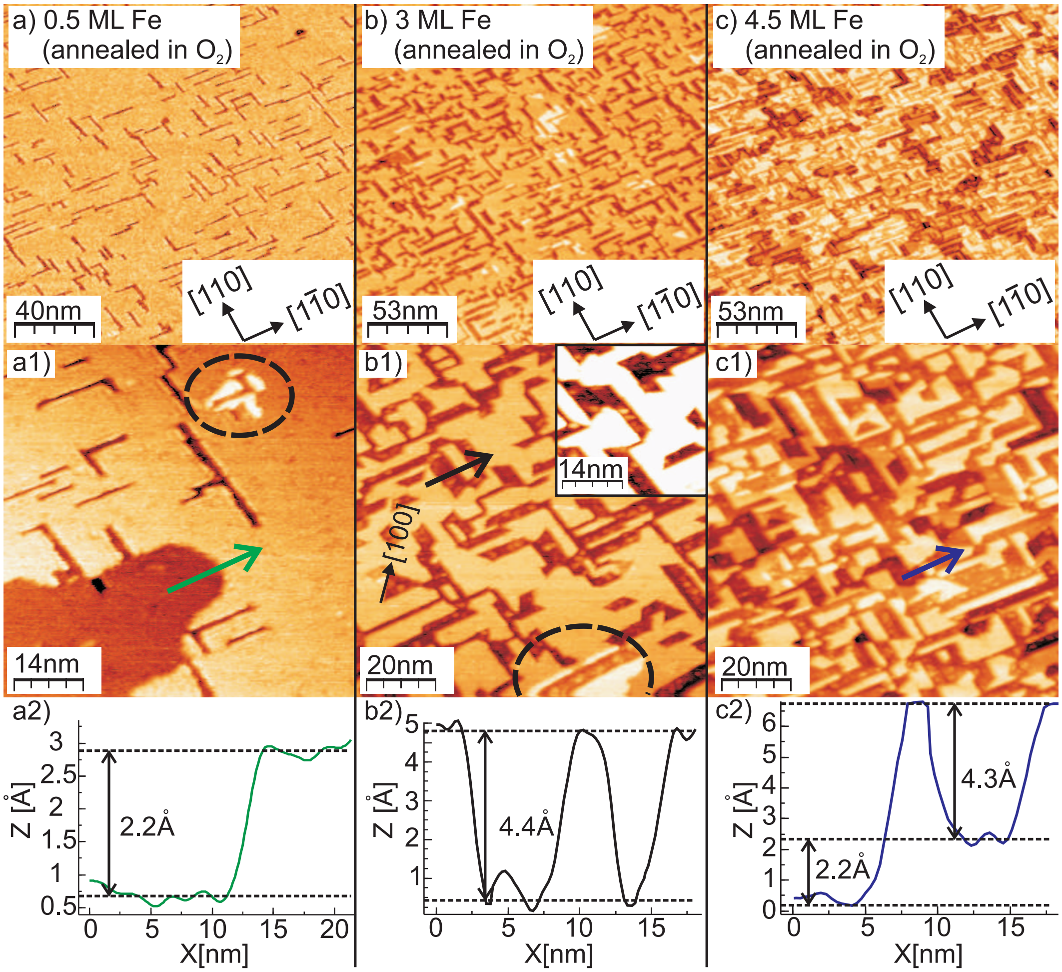

**Figure 5.30:** STM micrographs of the oxidized a) 0.5 ML, b) 3 ML and c) 4.5 ML Fe film ($V = 0.4\,\mathrm{V}\,, I = 0.9\,\mathrm{nA}$). Crystal directions corresponding to bulk Ag are given in the lower right corners of the STM images. The directions of the linescans are indicated in the images above by correspondingly colored arrows. Bias voltage was 760 mV for all measurements.

The round, three dimensional islands of the as-deposited Fe films have (almost) disappeared. Only inside the trenches, that separate the flat islands some three dimensional islands can be found for the 3 ML and 4.5 ML film (cf. inset in Fig. 5.30 b1)). In contrast to this the oxidized 0.5 ML film is atomically flat and exhibits thin, straight trenches either along the Ag[110] or the Ag[$1\bar{1}0$] direction (cf. Fig. 5.30 a)). On the first sight, these trenches may be domain boundaries resulting from the spreading of the Fe islands during oxidation. The domains of the oxidized 0.5 ML film (limited by the trenches) exhibit a rectangular shape. Nevertheless, comparing the STM images of the 0.5 ML film to the pre-investigations concerning very low Fe coverages several similarities can be found. The size and orientation of the trenches is the same as found for the annealed 0.05 ML Fe film. Only the number of trenches is significantly higher for the 0.5 ML film. This indicates a correlation between the deposited amount of Fe and the number of formed trenches upon annealing in oxygen. Given that the trenches observed for 0.05 ML Fe film can not be domain boundaries from spreading Fe islands, it is likely that the trenches in the oxidized 0.5 ML Fe film can neither be explained only by spreading of Fe islands. Additionally, the oxidation of 0.5 ML Fe would lead to 0.5 ML Fe oxide which would not cover the whole surface as seen in the STM images. This, however, will be discussed later.

With increasing coverage the flat domains are getting smaller while the trenches between the iron oxide domains are getting wider and the growth gets more and more three dimensional (cf. Fig. 5.30 b) and c)). Concerning the 3 ML and 4.5 ML film, the flat domains reveal also edges along the Ag<100> directions, indicated in Fig. 5.30 b1). We would like to point out, that the mixture of square (edges along Ag$< 110 >$) and hexagonal (edges along Ag$< 100 >$) shaped islands corresponds to the observed structures in the diffraction pattern (cf. Fig. 5.28). It can also be seen, that the nucleation of a new layer starts primarily at step edges (trenches), which is marked in Fig. 5.30 a1) and b1) by dashed, black ovals.

Linescans from the STM images show, that the step height between the different layers is always approximately a multiple of 2.2 Å (cf. Fig. 5.30 a2), b2) and c2)). The directions of the linescans are indicted in the STM micrographs above. Although STM is not exact for measuring height differences on a surface, because it images a convolution of electron densities and topographic heights, we assume that 2.2 Å represents the single step height at the surface of the oxidized film. Hence, 4.4 Å would be a double step height. Please note, that this single step height is in agreement with the layer distance $d = 2.2\,\text{Å}$ of FeO(001).

We also performed atomically resolved STM measurements of the oxidized Fe films as introduced above to investigate the superstructures observed in the LEED patterns shown in Fig. 5.28. Since the diffraction patterns of the 3 ML film showed a lower diffuse background (lower defect density at the surface), we will concentrate on the examination of this film with atomically resolved STM.

Fig. 5.31 is a cascading zoom of the oxidized 3ML film indicating that the superstructure in Ag[$1\bar{1}0$] or Ag[110] direction is due to alternating atomic rows showing a *bridge and gap* behavior. The unit cell of the superstructure is marked by dashed rectangles in Fig. 5.31 d). Also an antiphase boundary is shown indicating that the domain sizes of the superstructure are rather small which is in agreement to the streaks in the LEED pattern in Fig. 5.28 b) and c).

For illustration, linescans of the observed superstructure from the STM micrographs are presented in Fig. 5.32.

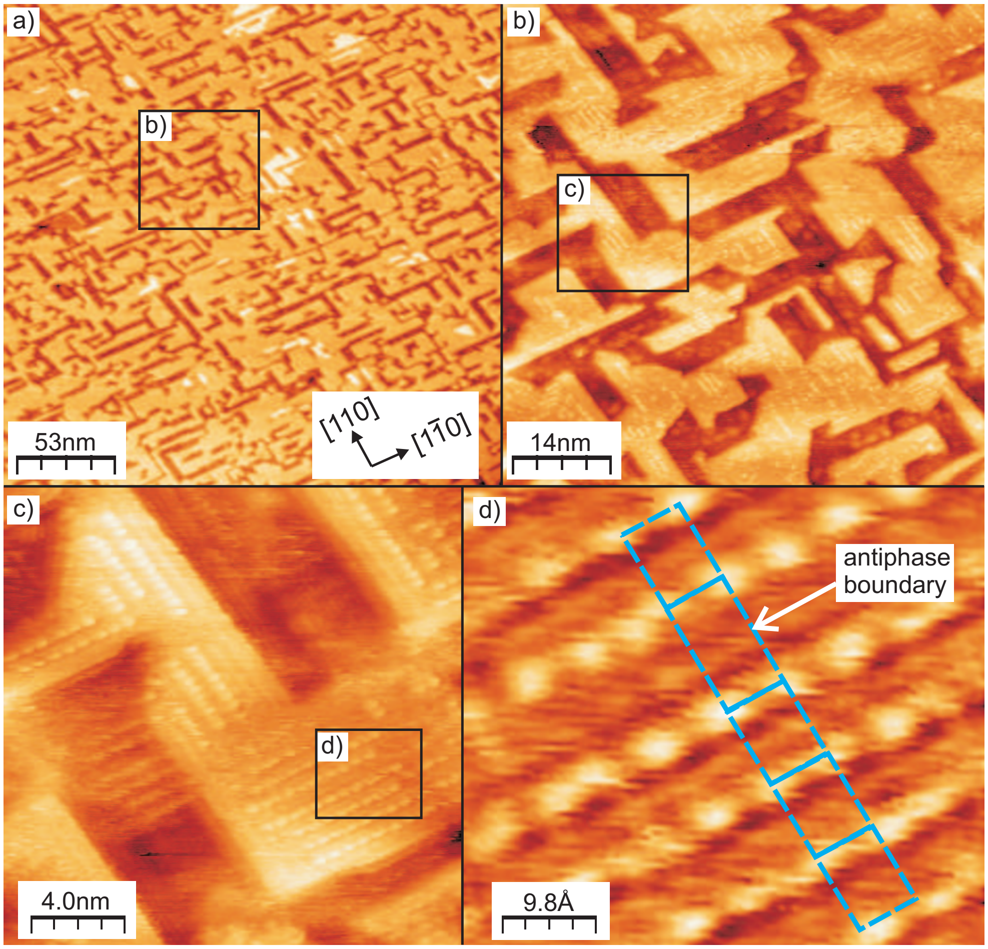

**Figure 5.31:** STM micrographs of the 3ML iron oxide film obtained at RT. The insets in a), b) and c) show the related enlarged areas in the subsequent micrograph. The observed superstructure is marked by dashed rectangles in d) ($V = 0.5\,\mathrm{V}$, $I = 1.6\,\mathrm{nA}$).

The presented linescans show that there is indeed a superstructure at the surface of the oxidized Fe film in Ag[1$\bar{1}$0] or Ag[110] direction. On the first sight, this superstructure is suggesting a (2×1) periodicity. But the measured atomic distances are larger than expected for a $(2 \times 1)$ structure corresponding to FeO(001), since a FeO(001)$(2 \times 1)$ superstructure in an STM image would result in a $(3.06 \times 6.12)\,\text{Å}^2$ surface unit cell. It has to be noted, that this can not be an experimental error through misadjustment of the STM, since all other measured atomic distances in this experiment produced reasonable values (cf. clean Ag(001) surface above). This superstructure will be discussed in more detail later.

So far, the analysis of atomic structures at the surface was focused on the topmost layer of the film. However, the growth of the oxidized Fe films seems to get more three dimensional for increasing coverage (cf. Fig. 5.30). Thus, it is reasonable to investigate the lower

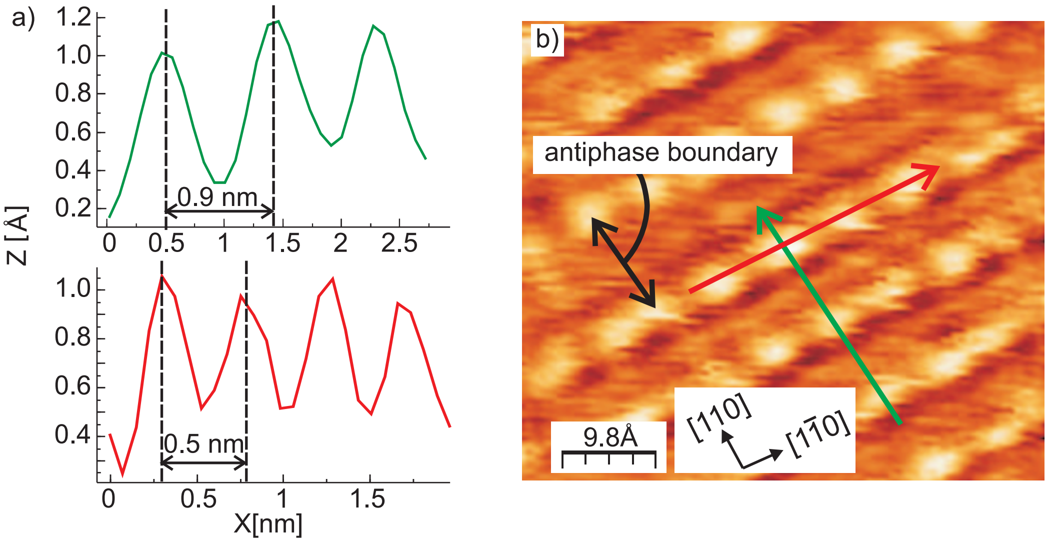

**Figure 5.32:** **a)** Linescans taken from the STM image of the 3 ML iron oxide film shown in **b)**. The average atomic distance in a row (red linescan) results in $a_{\mathrm{atm}} = 0.5\,\mathrm{nm}$ and the average row distance (green linescan) gives $a_{\mathrm{row}} = 0.9\,\mathrm{nm}$. An antiphase boundary can be identified by the bigger row distance (black arrow) ($V = 0.3\,\mathrm{V}\,, I = 1.5\,\mathrm{nA}$).

lying visible layers of the film. Fig. 5.33 presents a cascading zoom into the second layer (trenches) of the film, which is still visible between the topmost islands.

For better visibility we optimized the contrast of the STM image in Fig. 5.33 b) for the second layer of the film. Hence, the topmost layer looks overexposed. Clearly a hexagonal structure can be seen in Fig. 5.33 b1). This is in agreement with the diffraction experiments, mentioned above. These hexagonal structured areas seem to be undulated (cf. Fig. 5.33 b2)) but their visible size is to small to get quantitative information about a possible undulation length or height.

Again, we present linescans of the atomically resolved hexagonal structures in Fig. 5.34. Obviously, the observed structure is not hexagonal, but quasi-hexagonal as indicated by the inclined angle between the atomic rows, which is $\neq 60°$ as shown in Fig. 5.34. Hence, the atomic distances in the directions of the atomic rows must differ. Indeed this is the case, since the atomic distance in the direction of the vectors $\vec{a}$ and $\vec{b}$ is $a_{\mathrm{N.N.}} = b_{\mathrm{N.N.}} = 3.45\,\mathrm{Å}$. On the other hand, the next neighbor distance in direction of $\vec{c}$ is only $c_{\mathrm{N.N.}} = 2.6\,\mathrm{Å}$ (cf. Fig. 5.34). Although, these values have to be taken with caution because of the low resolution of the atomically STM images (cf. linescans in Fig. 5.34) it can be concluded that the second layer of the film exhibits an undulated quasi-hexagonal structure.

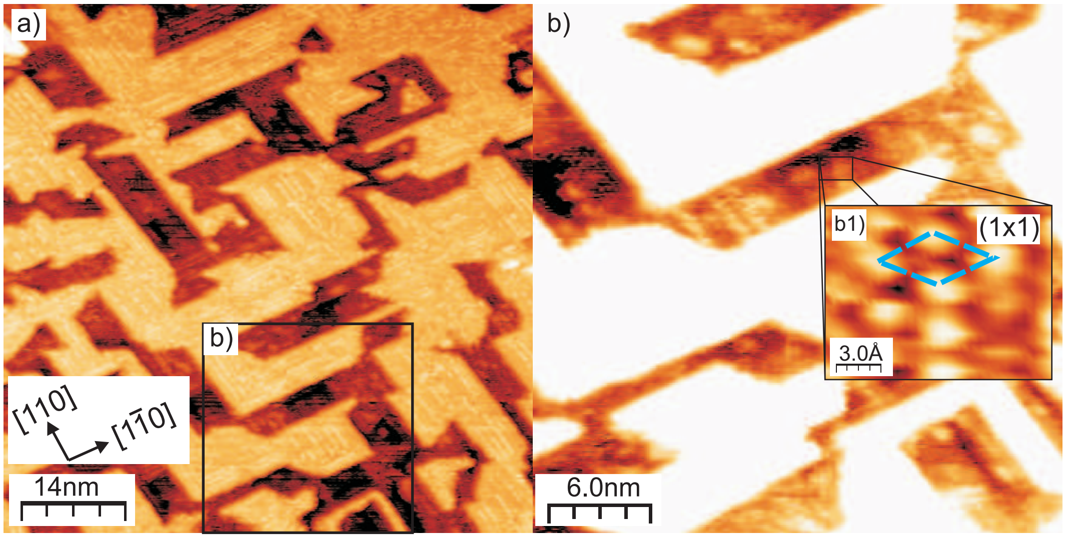

**Figure 5.33:** STM micrographs of the 3ML iron oxide film obtained at RT. The insets in b), b1) show the related enlarged areas in the micrographs. The contrast in b) is optimized for the visibility of the second layer. The hexagonal $(1 \times 1)$ structure is marked by a dashed rhomb in b1) ($V = 0.3\,\mathrm{V}\,, I = 1.6\,\mathrm{nA}$).

### 5.4.4 Discussion

Very low Fe coverages of 0.05 ML already lead to the formation of trenches with $2-3\,\mathrm{nm}$ width expanded either along the Ag[110] or Ag[1$\bar{1}$0] direction upon annealing in oxygen. Additionally, all initially deposited Fe clusters disappeared (cf. Fig 5.26). Due to the very low initial Fe coverage it is unlikely that the Fe clusters formed a closed wetting layer upon annealing in oxygen. This indicates that the presence of small amounts of Fe at the Ag(001) surface has a significant influence on the reactivity between the Ag(001) substrate and the surrounding oxygen. Although Ag(001) is inert against molecular oxygen it has been shown in theoretical studies that atomic oxygen reacts with the Ag(001) surface leading to different surface reconstructions depending on the oxygen amount [94]. Since Fe forms different kinds of oxides under temperature treatment in $O_2$ atmosphere, it is likely that the deposited Fe can serve as a catalyst for the reaction of oxygen with the Ag(001) surface especially for low coverages.

Even a 0.5 ML Fe films seems to completely wet the Ag(001) surface after oxidation at 300°C (cf. Fig 5.30 a)). Thus it is possible, that again the Fe clusters act as catalysts for a reaction of Ag(001) with atomic oxygen. Nevertheless, the oxidized 0.5 ML Fe film may also be FeO(001) without any formation of superstructures, since its diffraction pattern exhibits a clear $(1 \times 1)$ structure as shown in Fig. 5.28 a). At this point we can not give clear evidence for one of the possible explanations and further (theoretical) studies have to be done.

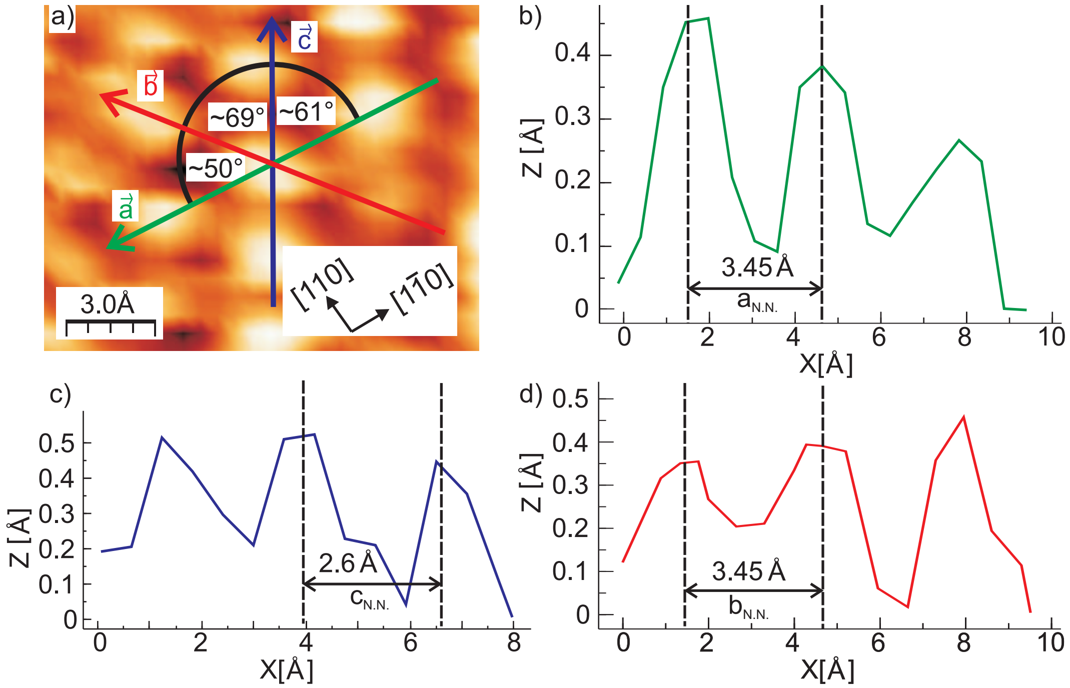

**Figure 5.34:** Linescans b), c) and d) from the STM micrograph shown in a). The average atomic distance in Ag[1$\bar{1}$0] direction (green linescan) and in the direction of the red linescan results in $a_{\text{N.N.}} = b_{\text{N.N.}} = 3.5\,\text{Å}$. The atomic distance in direction of the blue linescan is $c_{\text{N.N.}} = 2.6\,\text{Å}$. The inclination angles $\measuredangle(\vec{a},\vec{b}) \approx 50°$ and $\measuredangle(\vec{b},\vec{c}) \approx 69°$ indicate a quasi-hexagonal structure. Bias voltage was 330 mV.

Furthermore, we detected no hexagonal superstructure in atomically resolved STM images for the oxidized 0.5 ML Fe film as it was observed for higher Fe coverages. The growth of FeO(001) an Ag(001) may not be to surprising, since this growth was also reported in former studies [29] (at least for film thicknesses of 22 ML). In these studies the FeO film was prepared by subsequent deposition of ML Fe followed by annealing in oxygen atmosphere. For the low coverages studied in this work, this preparation method is comparable to ours.

The trenches in the oxidized 0.5 ML film do have a homogeneous width of 1 nm and may also be domain boundaries resulting from the outspreading of the Fe islands during the oxidation process. Here, it would be possible that two outspreading FeO islands exhibit an antiphase boundary between them. Nevertheless, our pre-investigations on very low Fe coverages annealed in oxygen suggest that the formation of trenches is caused by a chemical reaction between the Ag(001) substrate and atomic oxygen. In this case the deposited Fe would serve as catalyst for the dissociation of the molecular oxygen.

With increasing initial Fe coverage the oxidized film starts to grow in three dimensional structures. Forming a first wetting layer followed by formation of three dimensional islands due to annealing can be described as STRANSKI-KRASTANOV behavior (cf. Chap. 2.1.3).

The size of the flat islands decreases while the trenches get bigger (cf. Fig. 5.30).

A closer look at the trenches reveals that there is no atomically flat Ag(001) visible between the islands but the trenches (especially the larger trenches of the 3 ML and 4.5 ML film) are filled with residual clusters (probably Fe) and areas with hexagonal atomic structure, respectively (cf. Fig. 5.33). This hexagonal FeO areas reflect the two hexagonal structures in the diffraction patterns (cf. Fig. 5.28 b) and c)). There are two hexagonal domains visible in the diffraction patterns which are rotated by 90°, since it is energetically regardless for an hexagonal film in which of those two orientations it grows on the square substrate. Former studies have shown, that the first monolayer of FeO grows in quasi-hexagonal bilayers (FeO(111)-like) on different metal substrates with square surface unit cell such as Cu(001) or Pt(001) [26, 27, 28].

Furthermore, the quasi-hexagonal areas in the trenches show an undulation(cf. Fig. 5.33). Probably these undulations are a result of the strain reduction in the quasi-hexagonal film. Since these undulations will be important in the next chapter, a detailed discussion of the undulated FeO(111) film will be carried out then. Nevertheless, these undulations can act as a phase grating for slow electrons and lead to the elongated diffraction spots found in the LEED experiment (cf. Fig. 5.28 b) and c)) as explained in Chap. 2.2.6.

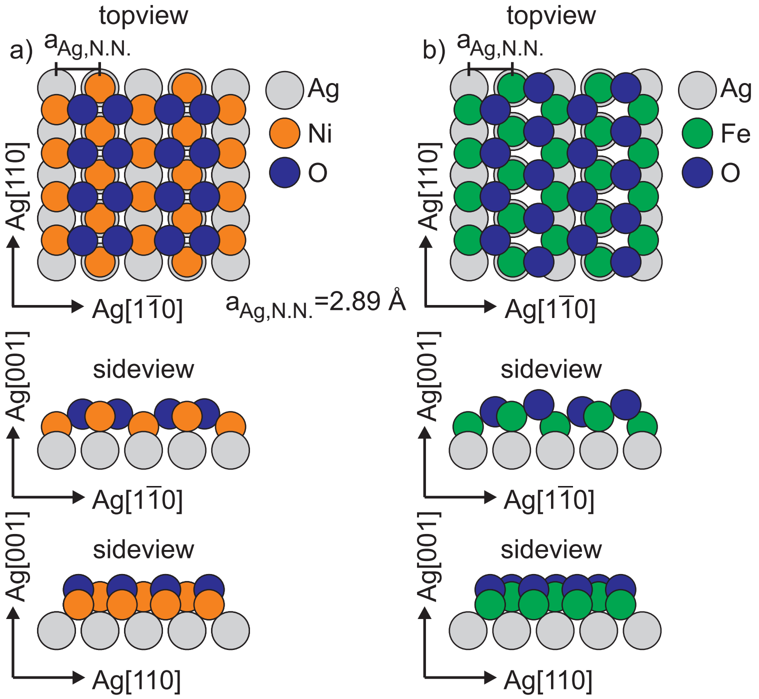

**Figure 5.35: a)** Model of the NiO structure as suggested by Bertrams et al. for the growth on Ag(001) [95]. **b)** Structure corresponding to our STM results forming a quasi-hexagonal FeO(111) bilayer.

We would like to note, that a similar structure was also found by Bertrams et al. for the growth of NiO on Ag(001) [95]. An adapted model of this superstructure for FeO on Ag(001) is shown in Fig. 5.35 a).

According to Bertrams' model, the Fe rows are located at top or bridge sites on top of the Ag(001) substrate (forming quasi-hexagons) while the oxygen atoms form a rectangular structure on the Fe sublayer occupying threefold hollow sites between the Fe atoms. Since NiO and FeO are both transition metal oxides, it is likely that FeO would form a quasi-hexagonal structure on Ag(001) as well. Since we did not observe a rectangular structure on top of the quasi-hexagonal layer in the STM image (cf. Fig. 5.34), we assume that in our case the oxygen also forms a quasi-hexagonal layer on top of the iron, what in total corresponds to a bilayer of FeO(111) (cf. Fig. 5.35 b)).

The second, poorly ordered superstructure with two domains along the Ag[$1\bar{1}0$] and Ag[110] direction that is indicated by the remaining streaks in the LEED pattern could be confirmed by the observed low ordered superstructure in the STM micrographs (cf. Fig. 5.28 and Fig. 5.31). This superstructure suggests a $(2\times1)$ periodicity on the first sight. Nevertheless, the superstructure found in our STM measurements does not fit the estimated size of a FeO(001)$(2\times1)$, since the surface unit cell measured by STM is $(5\times9)\,\text{Å}^2$ instead of $(2.89\times5.78)\,\text{Å}^2$.

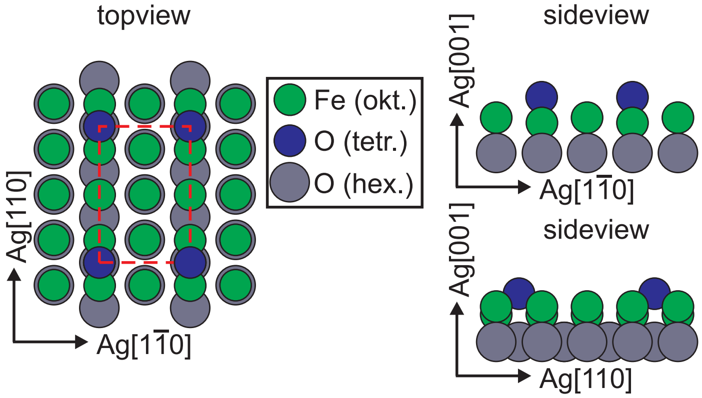

**Figure 5.36:** Our model of the topmost iron oxide layer leading to the observed superstructure in the STM images. Atoms in the hexagonal oxygen layer are only larger for visibility. The dashed rectangle corresponds to a $(2\times3)$ superstructure on Ag(001), respectively. In this model the topmost bilayer has Fe atoms onoctahedral sites (first layer) and oxygen on some tetrahedral sites (second layer) corresponding to $Fe_3O_4$(001).

This $(2\times1)$-like superstructure was only observed on the topmost layer, which is located on top of the quasi-hexagonal layer underneath. As mentioned above, it is known that iron oxide tends to grow as FeO(111) only in the first few layers but forms $Fe_3O_4$(001) on square, metal substrates for higher coverages [25, 26, 27, 28]. Therefore, it is possible that the topmost layer already shows $Fe_3O_4$(001) structure. Hence, we created a model that fits our STM results (see Fig. 5.36). This model assumes a $(2\times3)$ superstructure corresponding to the Ag(001) substrate (red, dashed rectangle).

In our model the atomic Fe rows in Ag$[1\bar{1}0]$ direction at the interface towards the quasi-hexagonal FeO layer occupy alternating octahedral top and bridge sites. The oxygen is tetrahedrally coordinated on top of the Fe atoms. It has to be noted, that in a $Fe_3O_4$(001) bilayer the tetrahedrally coordinated oxygen would form a $(2 \times 2)$ superstructure. Hence, the observed superstructure in our model would be an oxygen deficit structure. This may be an explanation for the small domains of the superstructure. We would like to point out, that this model gives only one possible explanation for the observed superstructure. Theoretical calculations have to be done in the future to verify this model.

Nevertheless, we suppose that our oxidized Fe films formed partly FeO(001) (for the 0.5 ML Fe film), as well as FeO(111) and a $Fe_3O_4$(001) like structure (for higher coverages) on the Ag(001) substrate. Our results suggest, that the topmost layer of the iron oxide film is mainly $Fe_3O_4$(001) with a poorly ordered $(2 \times 3)$ superstructure on it, while the quasi-hexagonal FeO(111) surface was only observed at the interface (inside the trenches) between film and substrate. It has to be mentioned that there is no study at this time that has reported both kinds of surface orientation ($Fe_3O_4$(001) and FeO(111)) as well as the two superstructures for the growth of iron oxide on Ag(001) at the same time.

## 5.5 Reactive deposition of Fe on Ag(001) in $O_2$ atmosphere

In this chapter Fe oxide films grown reactively in $10^{-5}$ mbar $O_2$ on Ag(001) will be discussed. The surface structure and morphology of these films are studied in detail using LEED, SPA-LEED and STM while the chemical composition of the films is analyzed by XPS. Prior to the measurements we deposited films of different thickness (substrate temperature 300°C) on the Ag(001) substrate and calibrated the absolute film thickness with quantitative AES (similar to Chap. 5.3). Fig. 5.37 a) presents the AE spectra obtained for three different film thicknesses.

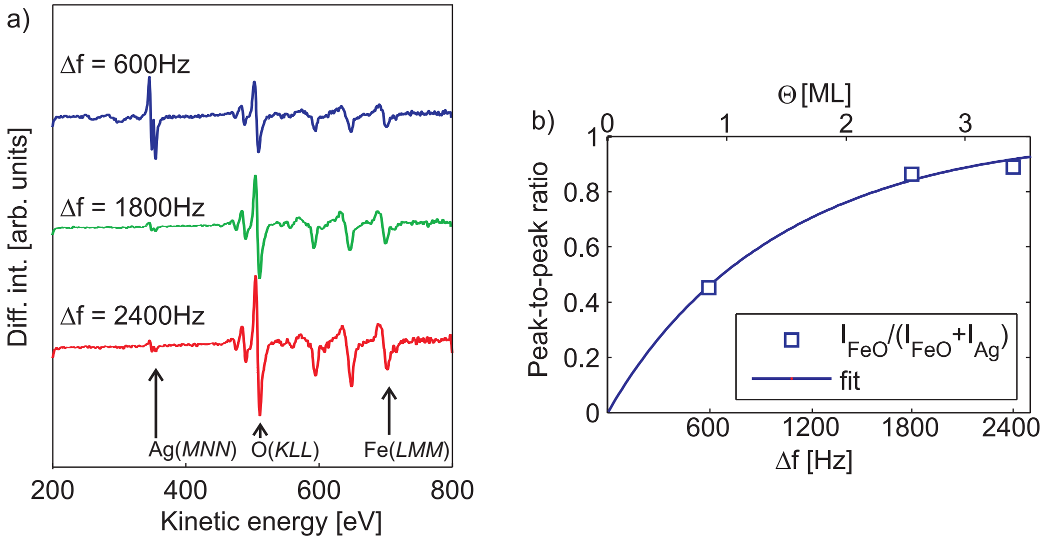

**Figure 5.37:** **a)** Exemplary AE spectra obtained from Fe oxide films of different thickness on Ag(001). The Fe($LMM$)(703eV), the Ag($MNN$)(351eV) as well as the O($KLL$)(503eV) Auger transitions are indicated by dashed lines. There is no contamination (e.g. C($KLL$)(271eV)) visible. **b)** peak-to-peak ratio between the sum of the Fe($LMM$)(703eV) and the O($KLL$)(503eV) signal and the Ag($MNN$)(351eV) signal (including the sensitivities $\sigma_i$) over coverage. The coverage in ML was calculated from Eq. 2.69.

In each spectrum the Auger transitions Ag($MNN$)(351eV), the O($KLL$)(503eV) and the Fe($LMM$)(703eV) can be seen. As expected the signal of the Ag substrate decreases with increasing film thickness, while the oxygen signal as well as the iron signal increase. No contamination of the films (e.g. carbon (271eV)) can be detected. Here, it is important to mention that the prior presented quantitative AES analysis is only exact for laminar growing films without the formation of an interface. Nevertheless, this analysis gives a good idea about the surface coverage and, therefore, an assignment between mass equivalent $\Delta f$ and coverage $\Theta$.

### 5.5.1 X-Ray Photoelectron Spectroscopy

From the position and shape of the Fe 2p peak in the X-ray photoelectron spectrum one can get information about the iron oxidation state and the stoichiometry of the films [96, 97]. Fig. 5.38 exemplarily shows the measured Fe 2p doublet of a 1 ML iron oxide film as well as the reference spectra: a) metallic iron ($Fe^0$), b) FeO ($Fe^{2+}$) and c) $Fe_2O_3$ ($Fe^{3+}$).

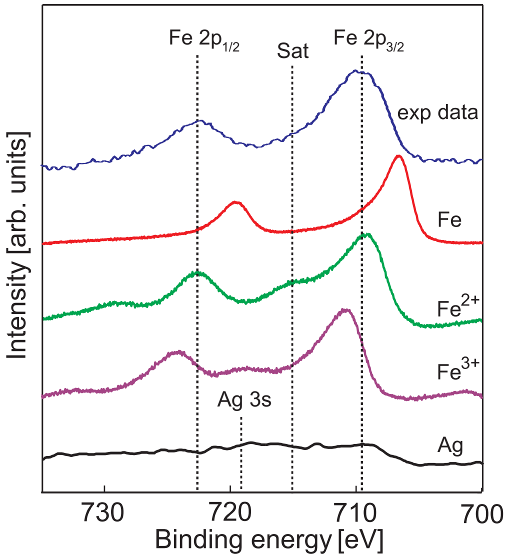

**Figure 5.38:** X-ray photoelectron spectrum of the measured Fe 2p doublet obtained from an iron oxide monolayer. Reference spectra of a pure Fe film, an FeO film ($Fe^{2+}$ spectrum) and $Fe_2O_3$ film ($Fe^{3+}$ spectrum) are additionally shown. The positions of the Fe $2p_{3/2}$ and Fe $2p_{1/2}$ peaks as well as the position of the Fe $2p_{3/2}$ satellite for $Fe^{2+}$ from the reference spectrum are marked by dotted lines. For comparison, the photoelectron spectrum of a pure Ag(001) substrate is presented at the bottom. This spectrum is scaled to the intensity of the Ag 3d peak in the spectrum of the iron oxide film. Thus, the substrate does not show any significant contributions.

The reference spectra were obtained from iron oxide films grown under oxygen deficiency and oxygen excess on MgO(001), respectively [98]. One can see, that for our sample both the positions at 706.3 eV and 722.5 eV of the Fe $2p_{3/2}$ and Fe $2p_{1/2}$ peaks, respectively, as well as their shapes point to the dominant presence of $Fe^{2+}$ ions in the film. In agreement with experiments performed on iron oxide films on Pt(111) [99] we conclude that FeO (wustite) monolayers grow on Ag(001). Another hint for FeO stoichiometry of the iron oxide film is the weak Fe $2p_{3/2}$ satellite at 715 eV which does not exist for $Fe_3O_4$ where the spectrum shows a plateau without satellites [100]. Also a Ag 3s peak at 719 eV obtained from a pure Ag(001) XPS spectrum can be seen in Fig. 5.38. For reasons of comparison, we scaled this spectrum to the iron oxide film using the intensity of the Ag 3d peak at 372 eV (not shown here). It can be concluded that the substrate Ag 3s signal from the Ag substrate has no significant influence on the measured Fe 2p signal. It has to be noted, that the Fe 2p doublet obtained from thicker samples (not shown here) resulted in an increasing amount of $Fe^{3+}$ ions with increasing film thickness. This indicates the at least partial formation of $Fe_3O_4$ (magnetite) within iron oxide films with thickness beyond monolayers.

### 5.5.2 Electron diffraction

We deposited 1 ML Fe oxide films on Ag(001) at different substrate temperatures (200°C, 300°C and 400°C) in order to determine the optimal growth temperature for our investigations. At first we investigated the surface structure of the films by SPA-LEED. Three exemplary diffraction patterns (electron energy 108 eV) are shown in Fig. 5.39.

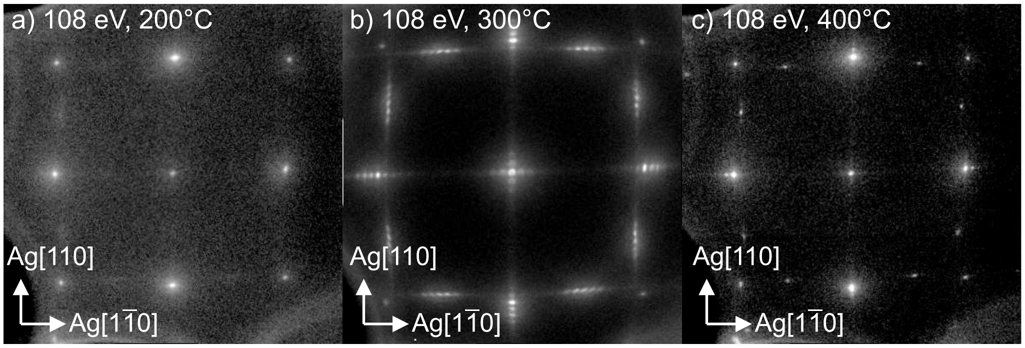

**Figure 5.39:** Diffraction patterns obtained from the 1 ML Fe oxide films grown at different substrate temperatures. Electron energy is 108 eV for all measurements.

Additional diffraction spots can be seen in all the diffraction patterns compared to the clean Ag(001) substrate. For the Fe oxide films grown at 200°C these additional diffraction spots are quite weak. The additional diffraction spots as well as the Ag(10) and Ag(01) (and equivalent) spots from the 300°C sample are split into five satellites either along Ag[110] or Ag[1$\bar{1}$0] direction. Such satellites can also be seen in the diffraction pattern of the 400°C sample. Nevertheless, the additional spots from the 400°C sample are only split into three weak satellites. Therefore, we will concentrate on the examination of the diffraction pattern from the Fe oxide film grown at 300°C.

The diffraction pattern presented in Fig. 5.40 a) can be decomposed into three components: (S) a square pattern of sharp diffraction peaks due to the Ag(001) substrate, (A) a hexagonal structure with diffraction spots which are split into five satellites along [110]-direction of the substrate due to the oxide film and (B) a second hexagonal pattern due to the oxide film which is rotated by 90° with respect to the first one and aligned in [1$\bar{1}$0]-direction of the substrate. Since the diffraction spots corresponding only to the Ag(001) substrate are not split the satellites are due to the Fe oxide film. This agrees with former studies on iron oxide films which reported that the growth of a few monolayers of FeO on cubic metal substrates like Cu(001) or Pt(001) shows (111) orientation [26, 27, 28]. Therefore, we conclude that a FeO(111) film growing in two domains was formed on the Ag(001) substrate.

Although, Ag as well as FeO have a cubic bulk structure, the corresponding crystallographic directions of the FeO monolayer and the Ag(001) substrate are obviously not parallel. Instead, the FeO monolayer grows epitaxially on Ag(001) with (111) orientation so that the crystallographic alignments are FeO[111] ∥ Ag[001], FeO[1$\bar{1}$0] ∥ Ag[1$\bar{1}$0] and FeO[11$\bar{2}$] ∥

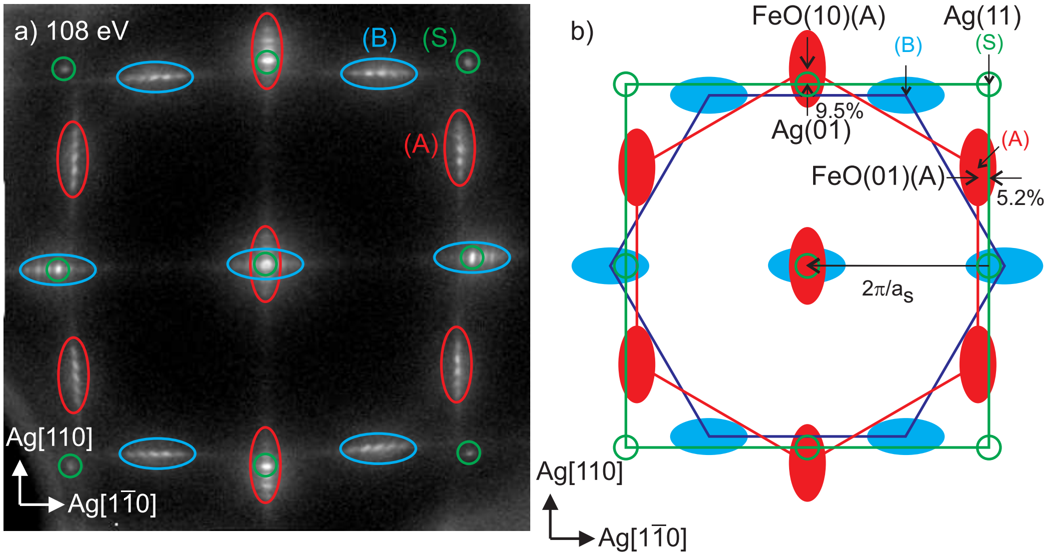

**Figure 5.40:** **a)** Diffraction pattern of the 1 ML Fe oxide film grown at 300°C. It can be decomposed into three components: (S) square pattern of sharp diffraction peaks due to the Ag(001) substrate, (A) a hexagonal structure with diffraction spots which are split into five satellites along [110] direction of the substrate and (B) a second hexagonal pattern which is rotated by 90° with respect to the first one and aligned in [1$\bar{1}$0] direction of the substrate. **b)** Schematic drawing of the diffraction pattern shown in **a)** for a relaxed FeO(111) film on Ag(001). The (10) and (01) spot of the FeO(A) domain are marked. Reciprocal distances between the diffraction spots of the FeO(A) domain and the reciprocal surface unit cell of Ag(001) are given in [% BZ].

Ag[110] for the A domain of the FeO(111) monolayer while the alignment is rotated by 90° for the B domain (cf. Fig. 5.41). Therefore, it is necessary to distinguish between crystal directions of FeO(111) film and Ag(001) substrate in the following.

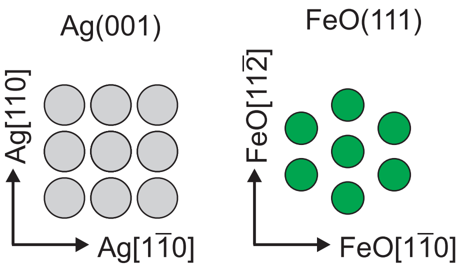

**Figure 5.41:** Crystallographic alignment of epitaxially grown FeO(111) on Ag(001). For visibility only the first layer of $Fe^{2+}$ ions is shown by green circles on the right.

As one can see in Fig. 5.40 b) there is a mismatch between a relaxed FeO film and a Ag(001) substrate in both surface directions (5.2% in Ag[1$\bar{1}$0] and 9.5% in Ag[110]-direction). The next neighbor FeO distance is $a_F = 3.05\,\text{Å}$ and the bulk FeO(111) row distance $c = 2.64\,\text{Å}$ while the surface lattice constant of Ag(001) is $a_s = 2.89\,\text{Å}$. Therefore, it is likely that the splitting of the diffraction spots is a result of a strain reducing structure of the film (e.g. facets or dislocation networks).

We performed high resolution diffraction experiments of the (00)-spot at different electron energies to analyze the splitting of the diffraction spots in more detail. Fig. 5.42 a) shows a cutout from the diffraction pattern shown in Fig. 5.40.

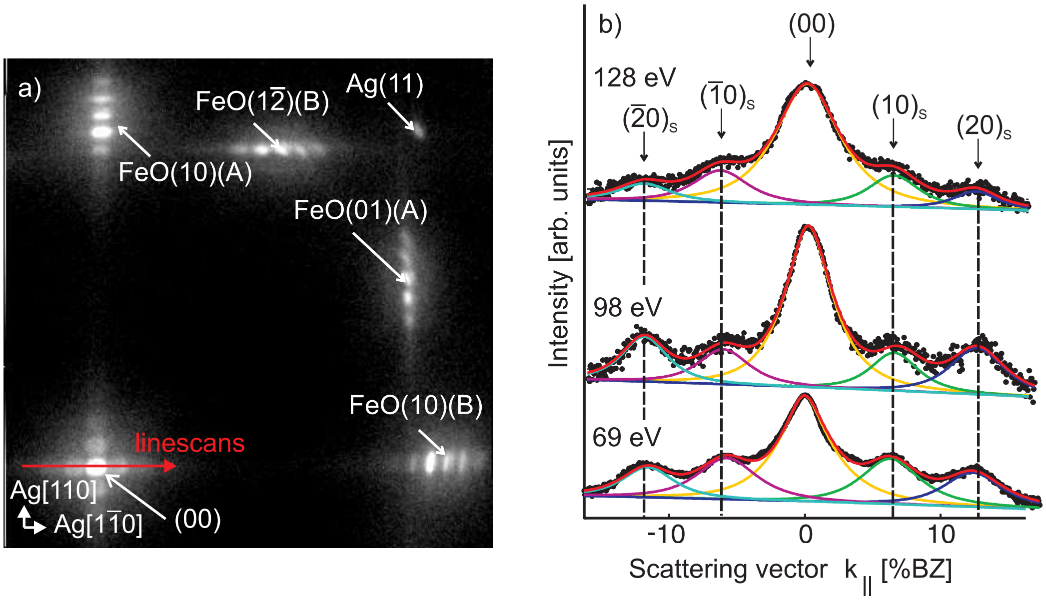

**Figure 5.42:** **a)** Cutout from the diffraction pattern of the 1 ML FeO film grown at 300°C. The corresponding diffraction spots from both FeO domains as well as the Ag(001) substrate are labeled for clarity. The direction of the linescans in **b)** is indicated by a red arrow in a). The satellites of the (00) diffraction spot are marked with an 'S' in the index.

The corresponding diffraction spots from both FeO domains as well as the Ag(001) substrate are labeled for clarity. The direction of the linescans presented in Fig. 5.42 b) is indicated by a red arrow in a). The satellites of the (00) diffraction spot are marked with an 'S' in the index to distinguish between satellite spots and fundamental diffraction spots. The satellite spots do not change their lateral position in reciprocal space with increasing electron energy (cf. dashed lines in Fig. 5.42 b)). This indicates that the satellites can not be a result of surface facets or mosaics, as explained in Chap. 2.2.5. Hence, the satellites correspond to an additional lateral periodicity at the surface of the FeO film. The average distance between the satellites is $\Delta k_{||} = (5.9 \pm 0.3)\%\,\mathrm{BZ}$ as obtained for various electron energies. It shows that the additional periodicity at the FeO monolayer in Ag[1$\bar{1}$0] direction is $\Gamma_{\mathrm{SPA}}[1\bar{1}0] = 49(\pm 3)\,\mathrm{\AA}$ for the B domain. Equivalent results are obtained for the A domain analyzing the splitting of the diffraction spots in satellite peaks for the Ag[110] direction.

The high resolution diffraction experiments also show that the FeO(01)(B) diffraction peak is located at 105.9% BZ. Thus, the row distance of the FeO(111) monolayer is $c = 2.78(\pm 0.01)\,\text{Å}$ showing that the hexagonal lattice of the FeO(111) monolayer is expanded by 3.4% for the Ag[1$\bar{1}$0] direction. Therefore, one can assume that in average 18 FeO(111) atomic rows have to match 17 Ag(001) atomic rows and the quasi-hexagonal LEED pattern of one FeO(111) domain shows a (1 × 17) superstructure. Fig. 5.43 a) presents a schematic drawing of the unit cell in reciprocal space (corresponding to the diffraction pattern from Fig. 5.43 b)) introducing the reciprocal base vectors $\vec{b}_1^*$ and $\vec{b}_2^*$ for the A domain.

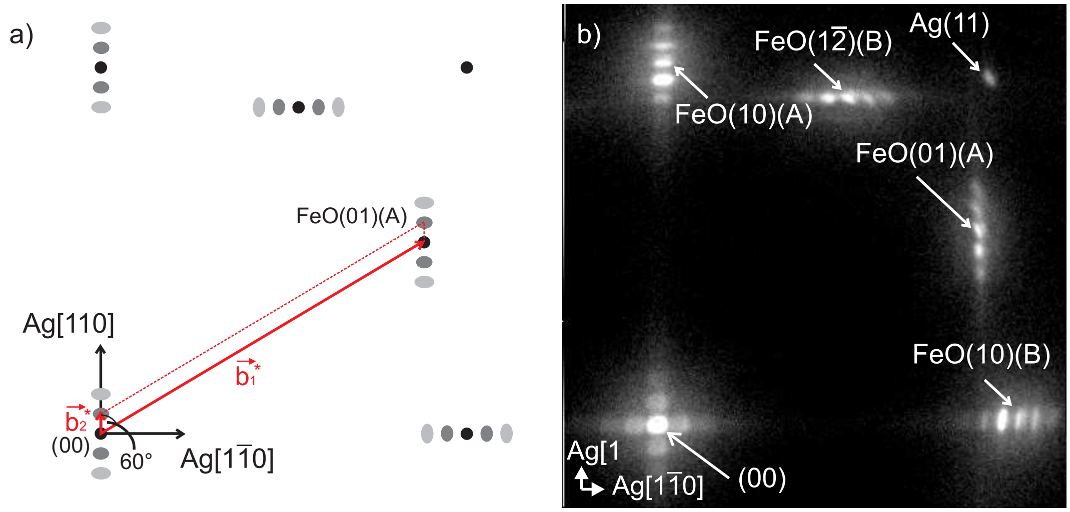

**Figure 5.43: a)** Schematic drawing of the superstructure reciprocal unit cell corresponding to the diffraction pattern shown in **b)**. The red arrows $\vec{b}_1^*$ and $\vec{b}_2^*$ are the reciprocal base vectors of the (1 × 17) superstructure.

This (1 × 17) superstructure and the non-vanishing of the intensity of the satellites for all electron energies is in accordance with the formation of an FeO(111) monolayer with undulation in Ag[1$\bar{1}$0] direction for the B domain of the film. Here, the periodic height undulation in one dimension acts as a phase grating for the electrons which leads to the raise of the observed satellite spots as explained in Chap. 2.2.6 and reported in former studies [49, 50, 101].

Finally we like to mention that we observe a slight increase of the full width at half maximum for increasing order $|h|$ (increasing $\left|\Delta \mathrm{k}_{||}\right|$) of the satellites marked by $(h0)_\mathrm{S}$ in Fig. 5.42 b). This effect can be explained by some degree of disorder of the undulation periodicity superposed to the quasi-hexagonal FeO(111) monolayer where the disorder can be attributed to variations of the dislocation distances.

The result of an uniaxial undulated FeO(111) monolayer with parallel dislocation lines for one domain as obtained from the diffraction data is quite surprising. In general one expects undulation in two lateral directions due to lattice mismatch. Furthermore the symmetry of the hexagonal FeO(111) monolayer is modulated by the Ag(001) substrate with square symmetry so that some anisotropy of the undulation is expected due to the non-equivalence of crystallographic directions of monolayer and substrate. Therefore, we also performed STM measurements at room temperature in order to have more insight into the structure of the undulated FeO(111) monolayer.

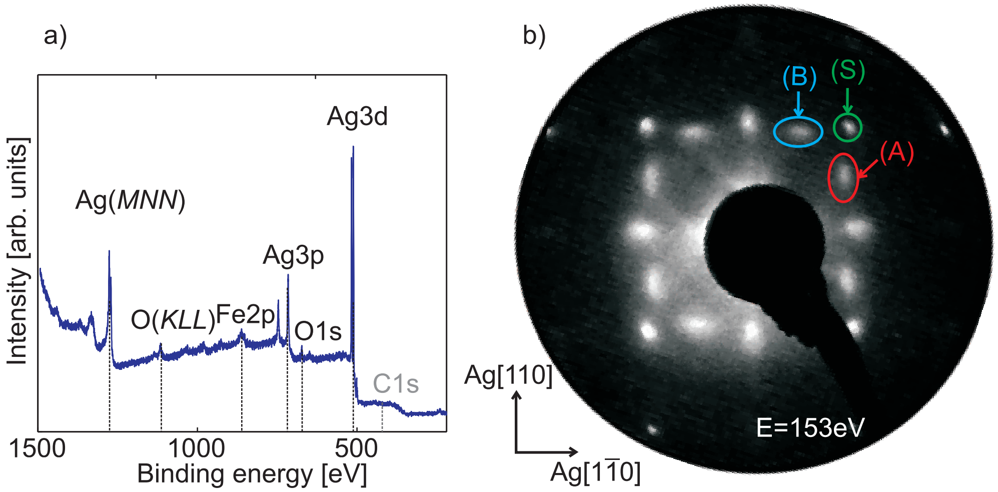

**Figure 5.44:** **a)** XP spectrum (survey) of the 0.5 ML FeO film. Ag, O and Fe transitions can be seen, while no contamination (e.g. by carbon) was found. **b)** LEED pattern of the film obtained at 153 eV. The diffraction spots due to the two hexagonal FeO(111) domains and the Ag(001) substrate are indicated in the diffraction pattern (cf. Fig. 5.40).

We also deposited FeO(111) films of different thickness on top of the Ag(001) substrates in the UHV chamber #1 using the same preparation parameters as for the films introduced above in order to perform STM experiments on these films. LEED and XPS experiments were carried out to guarantee a comparable quality as for the prior discussed FeO films. Fig. 5.44 presents the XP spectrum and a LEED pattern of a 0.5 ML FeO film.

The XP spectrum shows no contamination of the film (for example with carbon) while Ag, O and Fe transitions can be seen in the survey. The diffraction pattern reveals diffraction spots due to the two hexagonal FeO(111) domains and the Ag(001) substrate in agreement to the FeO(111) films investigated by SPA-LEED (see above). While the SPA-LEED patterns showed split diffraction spots of the FeO film, the LEED pattern shows elongated diffraction spots due to the lower resolution of the LEED system. Nevertheless, we conclude that the prepared FeO(111) films are of the same quality as the prior discussed films.

### 5.5.3 Scanning Tunneling Microscopy

To obtain more insight in the structure of the overlayer we performed STM measurements on reactively grown FeO(111) films. An STM micrograph obtained after deposition of FeO films with different thickness on Ag(001) at 300°C is presented in Fig. 5.45.

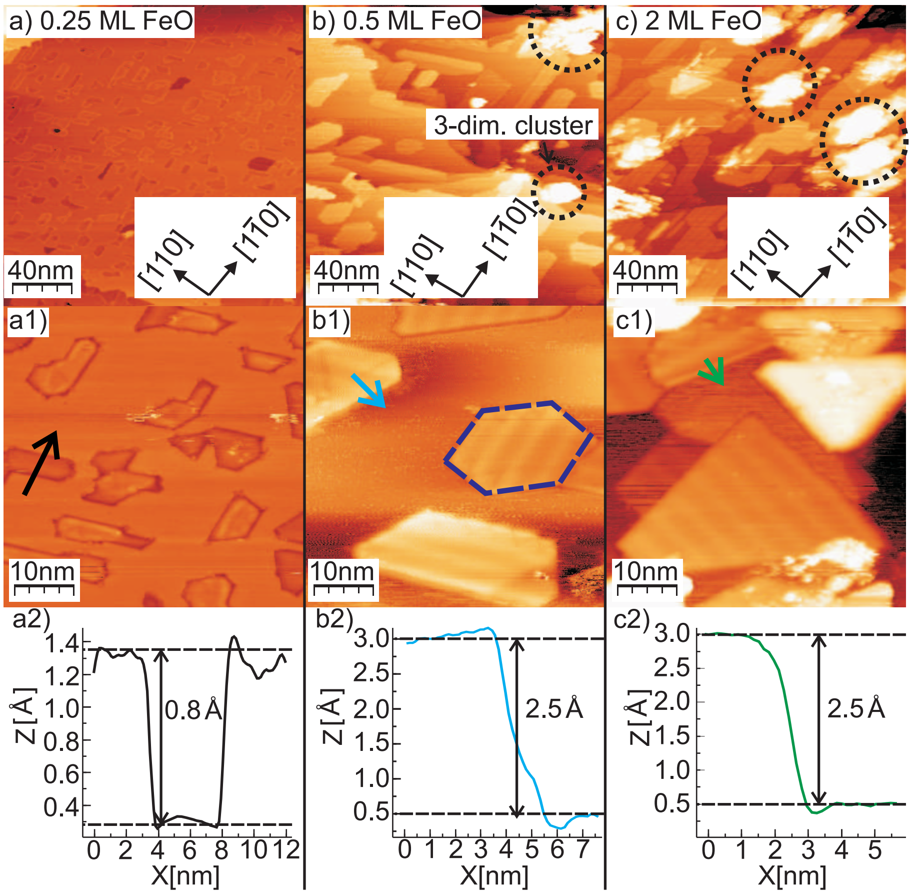

**Figure 5.45:** STM micrographs of **a)** 0.25 ML, **b)** 0.5 ML and **c)** 2 ML FeO films deposited on Ag(001) at 300°C ($V = 1\,\mathrm{V}, I = 0.8\,\mathrm{nA}$). Linescans within the micrographs are marked by arrows in the corresponding STM images. Three dimensional clusters are indicated by dotted circles in a), b) and c). The hexagonal structure of the islands is indicated by a dashed hexagon in b1).

On the first sight, it seems that the small islands of the 0.25 ML FeO film (cf. Fig. 5.45 a), a1) and a2)) are lowered into the surrounding substrate, while the islands of the 0.5 ML and 2 ML FeO film are pointing out. This effect, however, can be caused by the tunneling parameters during the STM measurement as described in Chap. 2.6.3. Obviously the FeO islands start to grow at various positions on the Ag(001) substrate, while no preferred conglomeration at substrate step edges is detected. With increasing coverage the islands are enlarging while the number of FeO islands per substrate area reduces. This points to coalescence of the FeO islands where material from the smaller islands diffuses towards the bigger islands. For the 2 ML FeO film the FeO islands overlap (cf. Fig. 5.45 c1)) indicating a three dimensional growth of the film at least for coverages beyond 1 ML. It can be also seen, that the amount of three dimensional clusters at the surface increases with the coverage (cf. dotted circles in Fig. 5.45 a), b) and c)). The edges of the FeO islands suggest a hexagonal structure of the film, which can be seen clearly in Fig. 5.45 b1) (blue, dashed hexagon). This is in agreement to the hexagonal structures found in the diffraction experiments. Furthermore, the undulations predicted from the SPA-LEED experiments are supported by the results from the STM measurements. These undulations either in Ag[1$\bar{1}$0] or Ag[110] direction can be already identified on some of the FeO islands shown in Fig. 5.45 b1) and c1). These undulations will be in the focus of investigations in the following section of this work. Finally, the step heights at edges of the FeO islands are about 2.5 Å for the 0.5 ML and 2 ML film (cf. Fig. 5.45 b2) and c2)). This exactly matches the step height of FeO(111). Nevertheless, the step height of the lowered seeming islands in Fig. 5.45 a2) is only about 0.8 Å. This phenomenon was discussed in Chap. 2.6.3.

### 5.5.4 Determination of the undulated islands by atomically resolved STM

A derived STM micrograph obtained after deposition of 0.5 ML FeO film on Ag(001) at 300°C is presented in Fig. 5.46.

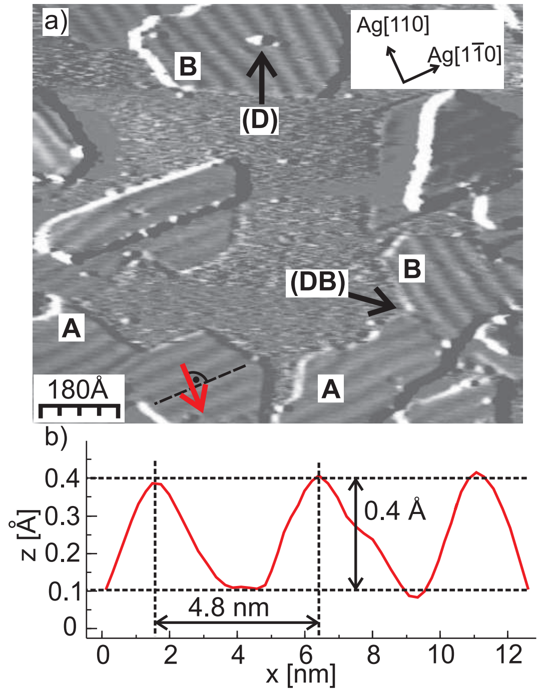

**Figure 5.46: a)** STM micrograph from a sample with 0.5 ML FeO(111) on Ag(001) (sample bias voltage 2.15 V, tunneling current 0.4 nA). The undulations are pointed out using the derived micrograph. Undulated FeO(111) islands of the two different FeO(111) domains are labeled by A and B as identified by the 90° rotated height undulations. In addition, a domain boundary (DB) and the formation of an additional undulation line (probably due to an defect (D)) are marked. An exemplary line scan perpendicular to the undulation is shown underneath the STM micrograph. The direction of the linescan in **b)** is indicated by a red arrow in the micrograph.

Clearly one can see that the heights of the FeO islands are undulated and that the undulation lines run (almost) parallel for each FeO island. The undulation orientation of the FeO islands, however, can be rotated by 90° for different islands (cf. the undulation of the two FeO domains A and B identified by electron diffraction). In accordance with the diffraction results, we named the undulation of the FeO islands by A and B in the STM micrograph shown in Fig. 5.46 a). The apparent height undulation of the FeO islands has been analyzed by one dimensional cuts from various STM micrographs (cf. also Fig. 5.46 b)). The periodicity of the undulation of $\Gamma_{\mathrm{STM}}\mathrm{Ag}[1\bar{1}0] = (48 \pm 2)\,\text{Å}$ obtained from these cuts agrees well with the diffraction results. Thus, the matching of 18 atomic FeO(111) rows to 17 atomic rows of Ag(001) for the Ag[$1\bar{1}0$] direction is confirmed by STM.

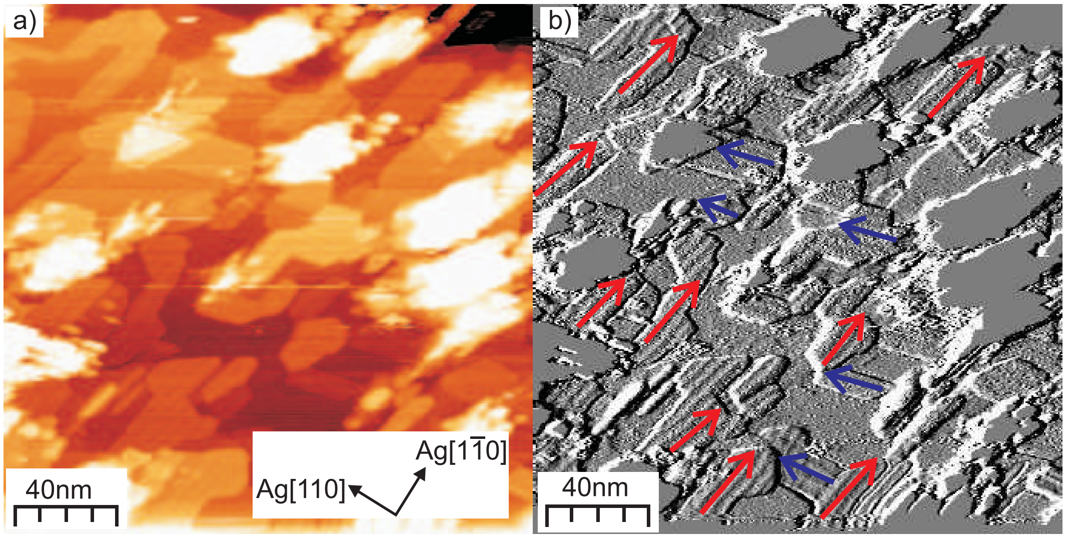

**Figure 5.47: a)** STM micrograph from the 2 ML FeO film ($V = 0.8\,\mathrm{V}$, $I = 0.6\,\mathrm{nA}$). **b)** derived image obtained from **a)** to point out the undulation on the FeO islands. The red and blue arrows indicate the directions of the undulations for FeO domain A nd B, respectively. One can see, that there is a slight variation in the direction of the undulation that was calculated to ±5° from various STM images.

Sometimes point defects seem to promote the nucleation of the undulation lines as may be concluded from the FeO island at the top of Fig. 5.46 a) where an additional undulation line can be seen close to a protrusion (marked by (D)). Occasionally, FeO islands with 90° domains meet each other and form domain boundaries (marked by (DB) in Fig. 5.46 a)). We attribute this effect to the coalescence of two adjacent FeO islands which are nucleated with different orientation of the undulation. Nevertheless, analyzing carefully the direction of the undulation lines for various FeO monolayers we deduce that their orientation is parallel within an variation of ±5°. Fig. 5.47 gives an overview over one of the STM micrographs that served for the calculation of this variation in orientation.

The flat areas in the derived image are resulting from the overexposed clusters in Fig. 5.47 a). Thus the formation of two types of domains observed by diffraction can be attributed to the nucleation of FeO islands with differently oriented undulations during early stages of FeO epitaxy.

It has to be noted that the variation angle of ±5° in orientation of the undulation lines is probably caused by a slight rotation of the FeO layer itself, which indicates a weak FeO-Ag interaction. A slight rotation of the FeO film can already lead to the observed variation angle of ±5° due to a moiré pattern like behavior of the undulation lines. This, however, will be discussed later.

Furthermore, some FeO islands showed no undulation but still had edges suggesting a hexagonal structure of the film. Fig. 5.48 a) shows an STM image obtained from the 0.5 ML FeO film.

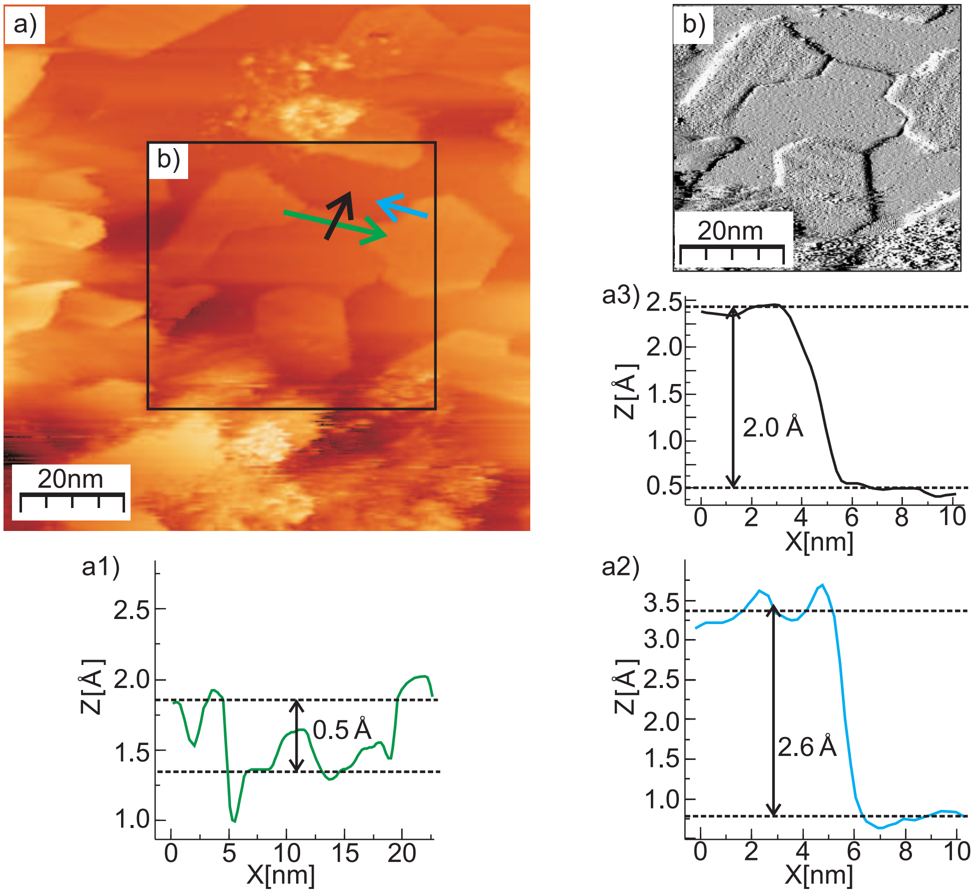

**Figure 5.48:** **a)** STM image obtained from the 0.5 ML FeO film. The island in the middle of the image is located between two undulated FeO islands but does not show any undulation itself. A derived image of these islands is given in **b)** to pronounce the undulations. Direction of the linescans taken from **a)** are indicated by the correspondingly colored arrows in **a)**.

The island in the middle of the image is located between two undulated FeO islands but does not show any undulation itself. A derived image of these islands is given in Fig. 5.48 b) to pronounce the undulations on the one hand and to show that the centered island is not-undulated on the other hand. The linescans reveal that the surface of the not undulated island is only about 0.5 Å lower than the undulated islands on both sides of it (cf Fig. 5.48 a1)). The linescan in Fig. 5.48 a3) indicates, that the step height (to the substrate) of the not undulated island is about 2 Å. This is about 0.5 Å less than the step heights of the undulated islands.

We performed atomically resolved STM measurements at RT to get a detailed insight on the atomic surface structure of the undulations. An atomically resolved STM micrograph of one undulated FeO island is shown in Fig. 5.49 a).

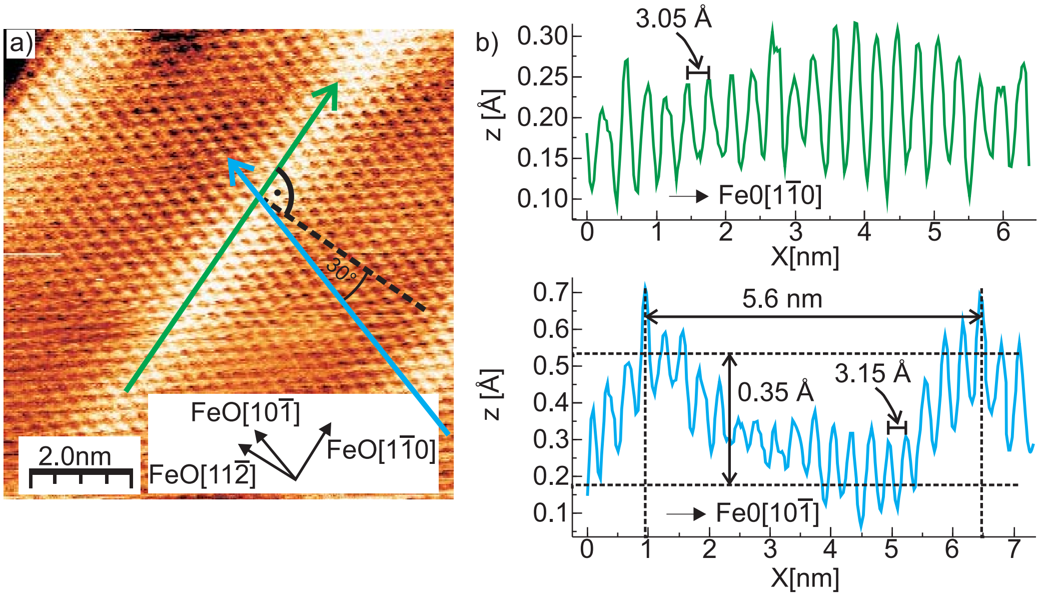

**Figure 5.49: a)** Atomically resolved STM micrograph of an FeO(111) island ($V = 0.1\,\mathrm{V}\,, I = 1.2\,\mathrm{nA}$). The undulation pattern propagates in FeO[$11\bar{2}$] direction. **b)** Linescans along the FeO[$10\bar{1}$] and FeO[$1\bar{1}0$] (FeO rows, scan directions indicated in STM micrograph) to show both the atomic distances along these directions as well as the undulation.

Since the STM images show the hexagonal FeO(111) islands it is useful to give crystal directions in the FeO system. The micrograph demonstrates that the FeO undulation lines of the undulation propagate parallel to the atomic FeO rows (Ag[110] || FeO[$1\bar{1}0$] direction) while the undulation 'wave' pattern can be characterized by a wave vector $\vec{Q}$ pointing in Ag[$1\bar{1}0$] || FeO[$11\bar{2}$] direction with $|\vec{Q}| = 2\pi/\Gamma_{\mathrm{STM}}\mathrm{FeO}[11\bar{2}]$. Obviously, the periodicity of the undulation is described by 18 atomically resolved FeO rows distributed over $(56 \pm 2)$ Å (cf. Fig. 5.49 b)).

Taking into account the projection on the FeO[$10\bar{1}$] direction (inclination angle 30° to

FeO$[11\bar{2}]$ direction) reproduces $\Gamma_{\mathrm{STM}}\mathrm{Ag}[1\bar{1}0] = (48 \pm 2)\,\text{Å}$ as obtained from the non atomically resolved STM micrographs. The linescan in FeO$[1\bar{1}0]$ direction reveals an atomic distance of 3.05 Å which is in good agreement to the next neighbor distance $a_{\mathrm{N.N.}} = 3.06\,\text{Å}$ on FeO(111). In contrast to this, the atomic distance along the FeO$[10\bar{1}]$ direction turns out to be 3.15 Å which is corresponds to a 3% expansion of the FeO film in this direction. This is close to the result obained from the diffraction experiments presented before (cf. Fig. 5.42 and corresponding explanations). Therefore, we conclude that the FeO film is expanded only in FeO$[11\bar{2}]$ direction, while the film is almost relaxed in FeO$[1\bar{1}0]$ direction. This suggests that the undulation is the result of the expansion of the film in FeO$[11\bar{2}]$ direction.

Although we stated that a quantitative height measurement via STM is difficult to do, we would like to point out that the STM linescan in Fig. 5.49 b) results in a undulation height of about 0.35 Å. Nevertheless, this value needs to be certified by a method which is sensitive to the nuclei positions of the surface atoms and not to the electronic structure as mentioned before. Since SPA-LEED is such a method, the height of the undulation will be determined carrying out a G(S) analysis of the diffraction measurements (cf. Chap. 2.2.7).

### 5.5.5 G(S) analysis of the undulation

As introduced in Chap. 2.2.7 and shown in former studies [49, 50], electron diffraction can give information about the height of undulations of thin films. Therefore, we analyzed the intensities of the (00) spot satellites from the 1 ML FeO film shown in Fig. 5.42 according to this theory. In Fig. 5.50 the relative integrated intensities of the satellites from the (00)-spot are shown, with

$$I_1 = \frac{I_{(10)_S} + I_{(\bar{1}0)_S}}{I_{(10)_S} + I_{(\bar{1}0)_S} + I_{(20)_S} + I_{(\bar{2}0)_S} + I_{(00)}} \text{ and}$$
$$I_2 = \frac{I_{(20)_S} + I_{(\bar{2}0)_S}}{I_{(10)_S} + I_{(\bar{1}0)_S} + I_{(20)_S} + I_{(\bar{2}0)_S} + I_{(00)}} \; .$$

For clarity a spot profile with the corresponding satellites is also given in Fig. 5.50. The calculated height of the undulation results in

$$\Delta h = \omega_0 2\sqrt{2} = 0.18\,\text{Å} \; , \qquad 5.2$$

whereas This value is almost two times smaller than the value $\Delta h_{\mathrm{STM}} = 0.35\,\text{Å}$ obtained from the STM measurements. We suppose this is a result of interference of the FeO(00) and the Ag(00) diffraction spot. Since for the (00) diffraction spot both diffracted intensities from the FeO film and Ag substrate interfere, this has a strong influence on the intensities of the central spot compared to the satellites and, therefore, on the result of the shown G(S) analysis. Hence, it is necessary to analyze the satellite spot intensities of an FeO spot

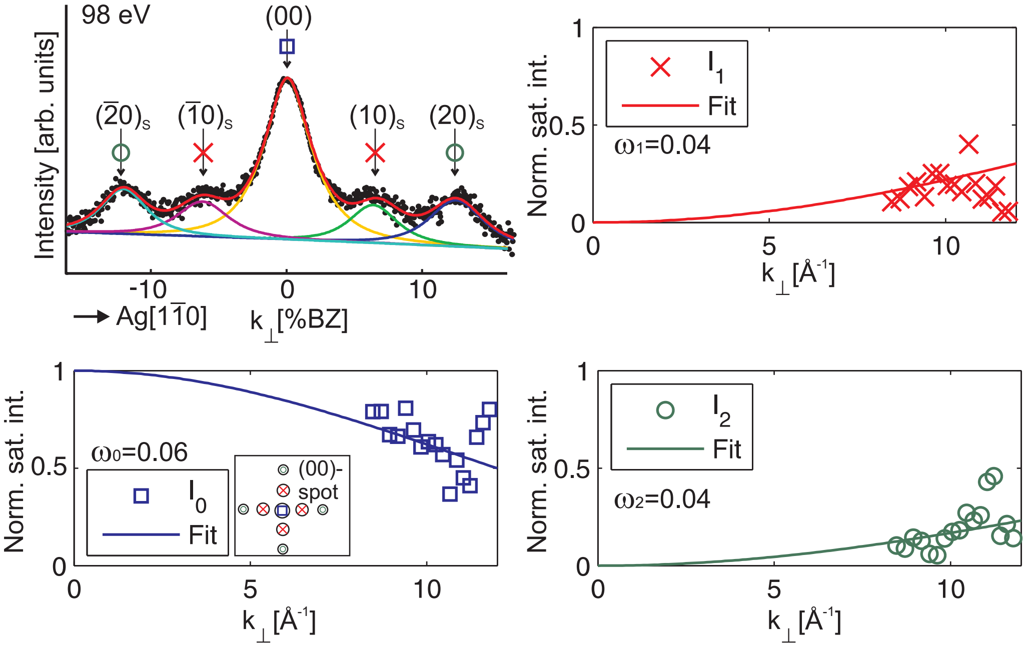

**Figure 5.50:** Normalized integrated intensities of the satellites from the (00)-spot in Ag[1$\bar{1}$0] direction over $k_\perp$. For clarity a spot profile with the corresponding satellites is also given (upper left part). The normalized satellite intensities were fitted by GAUSSIAN functions and the $\omega_i$ were obtained as fitting parameters under condition of Eq. 2.54 as described in Chap. 2.2.7.

that does not interfere with diffracted intensity coming from the Ag substrate. We chose the FeO(01)(A) diffraction spot for this analysis (cf. Fig. 5.43).

We present the linescans of the FeO(01)(A) diffraction spot in Ag[110] direction for the electron energies 81 eV, 109 eV and 128 eV in Fig. 5.51.

One can easily see that the part of intensity contributed by the central spot is much smaller compared to the (00) spot. This already shows clearly the influence of the substrate on the calculations presented above. Just like for the (00) spot we analyzed the relative integrated intensities of the satellite spots of the FeO(01)(A) diffraction spot. The results are presented in Fig. 5.52.

Here, the calculated height of the undulation results in

$$\Delta h = \omega_0 2\sqrt{2} = 0.34\,\text{Å}\ , \qquad 5.3$$

which is close to our STM results. Nevertheless, it can be seen in Fig. 5.52 that the used GAUSSIANS do not fit the data for energies higher than 100 eV = 11.5 Å$^{-1}$. It seems that the normalized intensity of the central spot reveals a minimum at about 100 eV while the

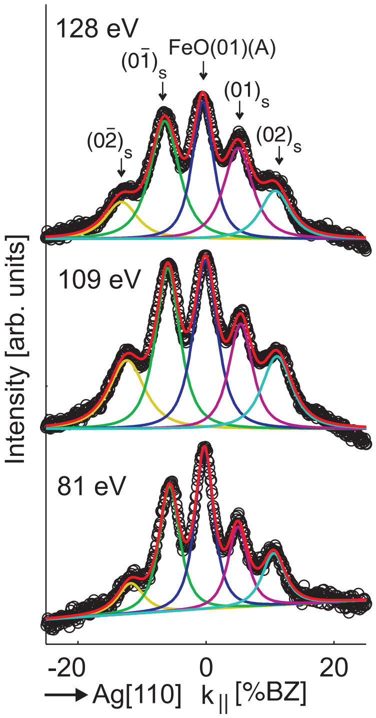

**Figure 5.51:** Linescans of the FeO(01)(A) diffraction spot in Ag[110] direction at 81 eV, 109 eV and 128 eV. The satellites of the diffraction spot are marked with an 'S' in the index.

intensity of the 2nd order satellites shows a maximum. This means, that a description via Bessel functions is needed to sufficiently match the data (cf. Fig. 2.19).

However, in our case a description via Bessel functions is not trivial, since standard Bessel functions as presented in Fig. 2.19 can not describe a minimum for $J_0(\mathrm{k}_\perp)^2$ and $J_2(\mathrm{k}_\perp)^2$ for the same $\mathrm{k}_\perp$, as it seems to be the case for our data. Furthermore, naming a maximum for $J_2(\mathrm{k}_\perp)^2$ at $\mathrm{k}_\perp = 10\,\text{Å}^{-1}$ one would assume a maximum for $J_1(\mathrm{k}_\perp)^2$ at lower $\mathrm{k}_\perp$ values (cf. Fig. 2.19) which is not observed in our data. This, however, can be attributed to the absence of data for $\mathrm{k}_\perp < 8\,\text{Å}^{-1}$. Having in mind, that the height value obtained from the Gaussian fit is already in good agreement to the STM measurements the conformation of our data for $\mathrm{k}_\perp > 11\,\text{Å}^{-1} = 98\,\text{eV}$ with modified Bessel functions would be beyond the scope of this work.

### 5.5.6 Discussion

As outlined above our studies on the growth of iron oxide monolayers on Ag(001) show that undulated quasi-hexagonal FeO(111) films are initially formed. We assume this happens for the following reasons: Firstly, the XPS measurements of the Fe 2p photo electron emission indicate the formation of FeO due to the dominant presence of Fe$^{2+}$ related photoemission electrons while no considerable Fe$^{3+}$ signal could be detected. This result agrees well with the results of other authors for the initial iron oxide growth on Pt(111) [102]. Therefore, the initial formation of FeO under various conditions seems to be well

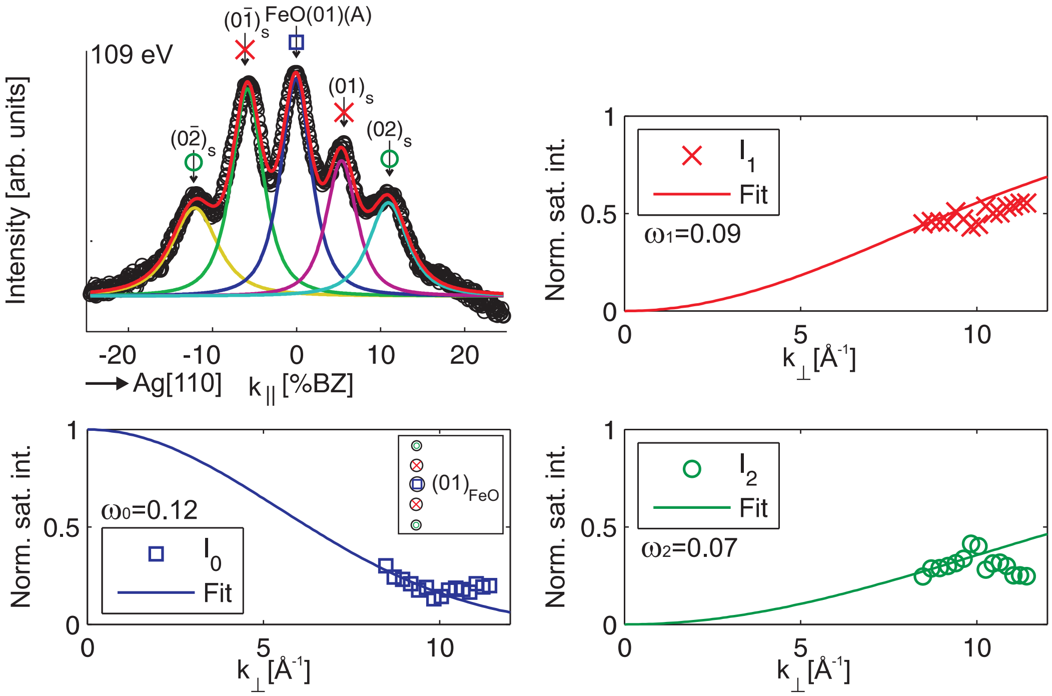

**Figure 5.52:** Normalized integrated intensities of the satellites from the FeO(01)(A) spot in Ag[110] direction over $k_\perp$. For clarity a spot profile with the corresponding satellites is also given (upper left part). The normalized satellite intensities were fitted by GAUSSIAN functions and the $\omega_i$ were obtained as fitting parameters under condition 2.54.

established. Secondly, additional diffraction spots would be expected in the diffraction experiments if the grown monolayers were $Fe_2O_3$ or $Fe_3O_4$ since the lattice constants of these structures are approximately twice the lattice constants of FeO. Thirdly, the hexagonal surface structure of the FeO monolayers as detected by both electron diffraction and STM indicates the growth of quasi-hexagonal FeO(111) with a slightly changed lattice constant in FeO$[11\bar{2}]$ direction compared to bulk values. In addition, both techniques demonstrate that the FeO(111) monolayer is undulated so that a large commensurate FeO superstructure is formed on Ag(001).

These results are in accordance with results obtained for the initial growth of iron oxide on other metal substrates. For instance, it has been reported that iron oxide initially grows a few monolayers with FeO stoichiometry on Pt(111) substrates while further growth proceeds as $Fe_3O_4$(111) for subsequent deposition of iron followed by annealing in oxygen atmosphere [20, 21, 22, 23, 102]. Other studies showed that even on fcc(001) substrates with square surface unit cell, such as Cu(001) or Pt(001), iron oxide grows initially with quasi-hexagonal symmetry and forms FeO(111) monolayers [25, 26, 27, 28]. On the other hand, however, it has been reported that ultrathin FeO films (several monolayer thickness) grow with (001) orientation on Ag(001) [29].

Interestingly, in contrast to the growth of FeO monolayers, monolayers of other TM oxides with rock salt structure, such as NiO, CoO or MnO, initially grow with (001) orientation on Ag(001) substrates for similar growth conditions as used in our study [95, 103, 104, 105, 106, 107, 108, 109, 110]. The preferred growth of oxide (001) monolayers can easily be explained by several arguments. Firstly, only non-polar surfaces are stable for ionic crystal surfaces since the surface dipole of polar surfaces leads to energetic instabilities [111]. This effect, however, can partially be compensated by the formation of superstructures at the oxide surface [13, 102]. Secondly, for the growth of oxide monolayers on the metallic substrates the energetically unfavorable monolayer dipole can be compensated by the mirror dipole formed in the metal substrate. Nevertheless, it is obvious from classical electrodynamics that flat lying dipoles (non-polar monolayer) is energetically unambiguously preferred compared to vertical dipoles (polar monolayer).

Here, we assume in accordance with other authors (cf. Ref. [13, 102] and references therein) that the first bilayer of FeO(111) grows with a layer of $Fe^{2+}$ at the interface and an $O^{2-}$ layer on top. Therefore, we have to conclude that there must be some interaction between $Fe^{2+}$ ions and metal substrates which prefer the iron layer in direct contact with the metal substrate while the oxygen layer is moved away from the interface and terminates the iron oxide bilayer. While this assumption is verified, e.g., for FeO(111)/Pt(111) using X-Ray Photoelectron Diffraction [112] we cannot give clear evidence for this assumption for FeO(111)/Ag(001). For quasi-hexagonal FeO(111) monolayers forming c(2×10) or (2×9) superstructures on Pt(001), however, the oxygen termination of the monolayer and the $Fe^{2+}$ interface layer are reported, too [26]. Nevertheless, the experimental results for the growth of FeO(111) on various metal substrates point to some site and element unspecific interaction between $Fe^{2+}$ and metals. Thus, VAN DER WAALS interactions may also be involved in this effect.

Most of the FeO(111) islands are undulated due to the lattice mismatch between film and substrate. This is observed in our study for deposition on Ag(001) in accordance with growth on Pt(111) [20, 21], Pt(001) [26] or Cu(001) [27, 28]. Nevertheless, there are some hexagonal FeO islands that show no undulation (cf. Fig. 5.48). Since these islands were only observed located between other, undulated FeO islands, it is possible that the limiting boundaries of the enclosed FeO islands suppress the formation of an undulation. The step height of the not-undulated FeO islands is about 0.5 Å smaller compared to the undulated islands (step height of 2.5 Å).

For the undulated islands the FeO molecules have to probe various different adsorption sites ranging from on-top to bridge or hollow sites and, on first sight, interaction between FeO layer and metal substrate also seems not to be very site specific. This is supported by the measured variation angle of about ±5° in the orientation of the undulations. As mentioned before, the variation angle in orientation of the undulations can be caused by a slight rotation of the FeO film. This phenomenon is known a moiré pattern and is illustrated in Fig. 5.53.

One can see that only a slight rotation of 1° of the quasi-hexagonal lattice already leads to a

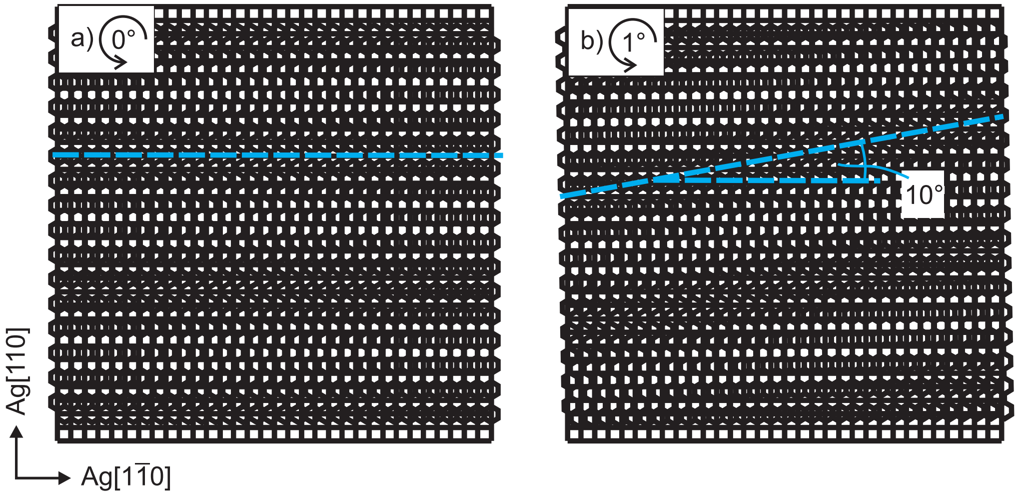

**Figure 5.53:** Moiré pattern forming due to the superposition of a quasi-hexagonal and a square lattice. The side length of the quasi-hexagons and the squares is true to scale measured by STM and SPA-LEED. **a)** shows an unrotated superposition where the density lines (undulation lines) run parallel to the Ag[1$\bar{1}$0] direction. The density lines in **b)** are already rotated by 10° due to a rotation of only 1° of the quasi-hexagonal lattice.

10° rotation of the undulation lines. Assuming a not very site specific FeO-Ag interaction, this explains the observed variation angle of about ±5° in orientation of the undulations.

On the other hand, all these studies as well as our study show some specific commensurate structures with substrate induced periodicity. Thus, there must also be some site specific (but possibly smaller) interaction between $\mathrm{Fe}^{2+}$ ion and Ag atoms.

For instance, among the superstructures for FeO on Pt(001) mentioned above FeO forms a $(\sqrt{84} \times \sqrt{84})R10.9^\circ$ superstructure on Pt(111) [26]. In general, these commensurate structures are only possible by some distortion of the FeO(111) bulk structures. For instance, the $(\sqrt{84} \times \sqrt{84})R10.9^\circ$ on Pt(111) involves 3% expansion of the entire FeO(111) monolayer while for the quasi-hexagonal FeO(111) monolayers on Pt(001) the distortion is anisotropic. Here, the FeO film is expanded by 5.2% in FeO[11$\bar{2}$] direction while a smaller expansion of 1.2% to 2.5% (depending on the superstructure) is reported for the FeO[1$\bar{1}$0] direction. On the one hand, the expansion of 3.4%, we observe for the FeO[11$\bar{2}$] direction of the FeO(111) monolayer on Ag(001), agrees with these data. On the other hand, in contrast to FeO(111) on Pt(001), we observe no distortion for the next neighbor FeO row. Here, the smaller lattice mismatch is probably advantageous.

We created a hard sphere model to describe the alignment of the FeO layer using the ionic radius of $\mathrm{Fe}^{2+}$ ions (0.76 Å) and the atomic radius of Ag (1.44 Å) taken from Ref. [79]. Since we assume that this model oversimplifies the details of the arrangement of the FeO(111) film on the Ag(001) substrate we focus on the corrugation height of the undulations. Assuming an on-top site for the most pronounced $Fe^{2+}$ ion we expect an undulation height of 1.3 Å for the undulation in FeO$[11\bar{2}]$ direction since the FeO molecule in the center between two on-top sites is located on a hollow site due to the zigzag arrangement between adjacent FeO rows. Fig. 5.54 a) shows the model obtained from the considerations presented above.

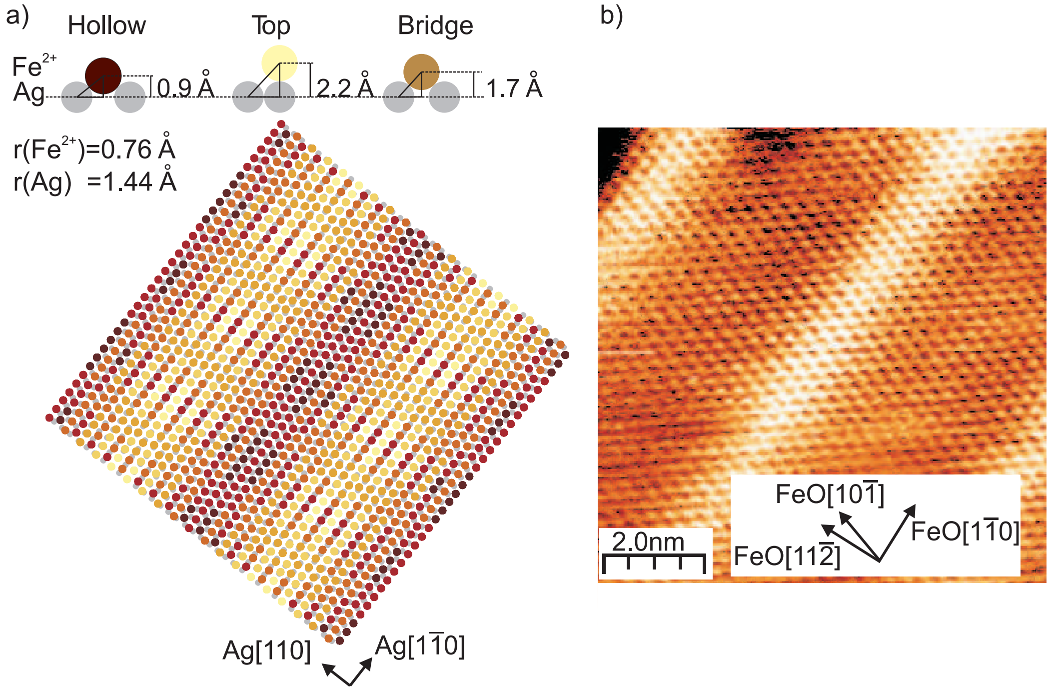

**Figure 5.54: a)** Hard sphere model of a FeO(111) film on Ag(001) which is relaxed in FeO$[1\bar{1}0]$ direction and expanded by 3.4% in FeO$[11\bar{2}]$ direction. Top, bridge, and hollow sites are presented including surface disctances and colors in the model. **b)** STM image of an undulated FeO island for comparison.

The periodicity of the undulation is reflected very well by the model, since 18 atomic FeO rows do match 17 atomic Ag rows in Ag[110] direction as is was expected from the STM and SPA-LEED results. We would like to add that a fully relaxed FeO(111) monolayer would lead to a $(1 \times 12)$ superstructure in this model, which was neither found by SPA-LEED or STM. But it can also be seen, that this hard sphere model can not describe the undulation in detail, since for a relaxed FeO(111) film in FeO$[1\bar{1}0]$ direction the FeO molecules probe different positions along an atomic Ag$[1\bar{1}0]$ row. This would lead to a second, weak undulation along this direction in a hard sphere model, as indicated in Fig. 5.54 a). Nevertheless, we did not observe an undulation along FeO$[1\bar{1}0]$ direction with STM or SPA-LEED. Thus, this model can only serve as a first idea about the origin of the observed undulation.

If the FeO islands would exhibit a perfectly ordered undulation, the diffraction pattern would indeed show a $(1 \times 17)$ superstructure. The fact that the fundamental diffraction spots do only exhibit satellites up to second order can be attributed to two things. Firstly, a degree of disorder in the size of the undulation and secondly, the relatively small share of undulated FeO islands compared to the whole surface. The average value of $\Gamma_{\mathrm{STM}}\mathrm{Ag}[1\bar{1}0] = (48 \pm 2)\,\mathrm{\AA}$ indicates that the size of an undulations can vary from 17 to 19 FeO atomic rows. This variation benefits the vanishing of the satellites spots for higher orders.

The G(S) analysis of the undulation height was problematic for the (00) spot due to interference of diffracted intensity from FeO film and Ag(001) substrate. In contrast to this, former studies concerning Ge films on Si(111) and Ag films on Si(001) were able to perform a G(S) analysis at the (00) spot [49, 50]. Here, the observed films were much thicker compared to our FeO film (16 nm Ge and 20 nm Ag films). Since the mean free path of slow electrons is much smaller than 16 nm, there is no remaining diffracted intensity from the substrates which would lead to a superposition of substrate and film signal. We solved this problem by analyzing the satellite spot intensities of the FeO(01)(A) spot (cf. Fig. 5.52) where no Ag(001) diffraction spot interferes with the measured intensity.

The obtained corrugation of the FeO film of $\Delta h = \omega_0 2\sqrt{2} = 0.34\,\mathrm{\AA}$ is in the same magnitude and, therefore, good agreement to the corrugations quantified in the studies mentioned above [49, 50]. In addition, the G(S) analysis of the FeO(01)(A) spot reflects well the results of the STM measurements. As mentioned before, a height measurement with STM is difficult to handle. We still assume the value of $\Delta h_{\mathrm{STM}} = 0.35\,\mathrm{\AA}$ to be reliable, since a FeO(111) surface consists only of $\mathrm{O}^{2-}$ or $\mathrm{Fe}^{2+}$ ions. Hence, the electronic structure should be similar for every atom at the surface of an FeO(111) island. Of course, the corrugation of the surface, and therefore the position of the surface atoms over the Ag substrate, may have an influence on the electronic structure at the surface. Nevertheless, we assume this influence to be small for FeO(111) films growing in bilayers ($\mathrm{Fe}^{2+}$ layer at the interface and $\mathrm{O}^{2-}$ layer on top), since the relevant electronic influence for the topmost atomic layer will come from the underlaying and is, therefore, comparable for every surface atom.

In summary, we have demonstrated that reactively deposited iron oxide initially grows as FeO (wustite) layer on Ag(001). Detailed analysis of SPA-LEED and STM experiments showed that the FeO(111) structure of the oxide film is undulated and forms a commensurate superstructure with respect to the Ag(001) substrate. Therefore, the quasi-hexagonal structure of the FeO(111) layer is distorted with respect to its bulk structure.

# 6 Conclusion

In a first step we analyzed the Ag segregation due to UHV annealing of ultrathin Fe films on Ag(001) at 300°C as observed in former studies [30, 31]. The Ag segregation was confirmed by AES and XPS. STM suggests a drastic change in surface structure upon annealing in UHV. The round, column-shaped Fe islands from the as-deposited films disappeared and the surface exhibits large, atomically flat areas with a square $(1 \times 1)$ surface unit cell corresponding to Ag(001). Three dimensional islands of about 5 Å height and branched structures are likely to be remaining Fe at the surface. Since the Fe in these islands and branched structures observed by STM is much less than expected from the AES and XPS measurements, we assume that Fe is buried underneath the flat Ag(001) areas. This is supported by energetic considerations.

Furthermore, electron diffraction suggests a $(\sqrt{2} \times \sqrt{2})$R45° superstructure after annealing of the Fe films in UHV. This superstructure, however, could not be resolved via STM. The atomically flat Ag(001) areas showed no superstructure and the Fe islands and branched structures did not allow an atomic resolution with STM due to their strongly three dimensional structure. Nevertheless, the $(\sqrt{2} \times \sqrt{2})$R45° superstructure observed in the diffraction patterns has not been reported in connection to the segregation of Ag on UHV annealed Fe films before.

Afterward we analyzed the changes in surface structure due to annealing of Fe films on Ag(001) in $O_2$ atmosphere. Our pre-investigations concerning very low Fe coverages of 0.05 ML suggest a significant influence of the Fe on the reactivity of the Ag(001) surface. Here, the surface forms trenches of $2-3$ nm width expanded along Ag[110] or Ag[$1\bar{1}0$] direction, respectively. Although it is known that Ag(001) is inert against molecular oxygen, the Ag(001) forms different reconstructions due to exposure to atomic oxygen [94]. It is likely that the atomic oxygen is provided by the Fe oxides formed at the Ag(001) surface during annealing in $O_2$ atmosphere. Hence, Fe acts as a catalyst for the oxidation of the Ag(001) surface.

Up to an Fe coverage of 0.5 ML the oxidized films wet the substrate. No superstructures can be seen in atomically resolved STM micrographs and the diffraction patterns show clear $(1 \times 1)$ structures. With increasing initial Fe coverage the oxidized films start to form three dimensional structures (Stranski-Krastanov behavior). The topmost layer of the oxidized films (for coverages above 3 ML) is $Fe_3O_4$(001)-like with a poorly ordered $(3 \times 2)$ superstructure on it (cf. Fig. 5.32).

The layers underneath, which are visible due to the Stranski-Krastanov behavior of the annealed films, exhibit a hexagonal surface structure. An inspection of the atomic next neighbor distances on this hexagonal structure reveals that it is in fact quasi-hexagonal. This is due an expansion of the hexagonal structure in one direction (cf. Fig. 5.34). Additionally, these hexagonal layers are undulated either along Ag[110] or Ag[$1\bar{1}0$] direction, but the visible areas are to small to give quantitative information about undulation heights ors lengths (cf. Fig. 5.33). Nevertheless, the corresponding diffraction patterns showed two quasi-hexagonal structures, which are rotated by 90° confirming the STM results. In accordance with former studies we assume these hexagonal layers to be FeO(111). Those studies reported the initial growth of FeO(111)-like iron oxide on Cu(001) or Pt(001), while $Fe_3O_4(001)$ formation was reported for higher coverages [25, 26, 27, 28]. It has to be mentioned that there is no study at this time that has reported both kinds of surface orientation ($Fe_3O_4(001)$ and FeO(111)) as well as the two superstructures for the growth of iron oxide on Ag(001) at the same time.

Finally we analyzed the reactive growth of Fe oxide by deposition of Fe in an $O_2$ atmosphere. Similar to the post deposition annealed (PDA) Fe oxide films, the here obtained diffraction patterns show two quasi-hexagonal structures, which are rotated by 90° against each other. On the other hand, no streaks in Ag[110] or Ag[$1\bar{1}0$] direction are observed in the diffraction patterns. XPS measurements suggest a dominant presence of $Fe^{2+}$ related photoemission electrons while no considerable $Fe^{3+}$ signal could be detected. Therefore, we assume that quasi-hexagonal FeO(111) films in two orthogonal domains are initially formed by reactive deposition of Fe on Ag(001).

The diffraction spots of the quasi hexagonal FeO(111) film are split into several satellite spots either along Ag[110] or Ag[$1\bar{1}0$] direction. For a substrate temperature of 300°C five satellites can be seen, while for higher temperatures the number of satellite spots decreases. These satellites do not change their position in reciprocal space with increasing scattering phase pointing to an additional periodicity at the surface of the FeO(111) film. This additional periodicity was found to be an undulation as confirmed by STM. The undulation lines run parallel to the atomic FeO rows within a variation angle of $\pm 5°$. It has to be mentioned that a slight rotation of the FeO(111) film can already lead to a significant rotation of the undulation lines due to a moiré pattern behavior. Hence, the interaction between FeO layer and metal substrate seems not to be very site specific.

The average undulation length determined by SPA-LEED and STM is $D = (48 \pm 2)\,\text{Å}$ corresponding to a $(1 \times 17)$ superstructure. The height of the undulation was measured via STM and calculated by a G(S) analysis of the satellite spot intensities from the diffraction experiments. This results in an average undulation height of 0.34 Å.

Atomically resolved STM micrographs show an expansion of 3.4% in FeO[$11\bar{2}$] direction for both domains of the FeO(111) film. This expansion can lead to the observed undulation as shown in the hard shepre model. Nevertheless, this model can not describe the undulation in detail since secondary undulations alon the FeO[$1\bar{1}0$] direction would appear due to probing of various positions of the $Fe^{2+}$ at the Ag(001) surface. This, however, was not observed in the STM measurements.

All in all we showed that it is possible to grow ultrathin Fe oxide films with different crystal structure and stoichiometry on Ag(001). Submonolayer Fe films, which are post deposition annealed in $O_2$ atmosphere at 300°C seem to wet the Ag(001) substrate forming FeO(001). Higher Fe coverages lead to STRANSKI-KRASTANOV morphology upon annealing in $O_2$ with the formation of quasi-hexagonal FeO(111)-like and $Fe_3O_4(001)$-like structures on different layers of the films. On the other hand reactive deposition of Fe in an $O_2$ atmosphere at 300°C results in the formation of undulated quasi-hexagonal FeO(111) islands.

# Bibliography

[1] R. M. Cornell and U. Schwertmann. *The Iron Oxides: Structure, Properties, Reactions, Occurrences and Uses.* Weiley-VCH, 2003.

[2] G. Ertl, H. Knözinger, and J. Weitkamp (Eds.). *Handbook of Heterogeneous Catalysis.* Wiley-VCH, 1997.

[3] M. N. Baibach, J. M. Broto, A. Fert, F. Nguyen Van Dau, F. Petroff, P. Etienne, G. Creuzet, A. Friederich, and J. Chazelas. Giant Magnetoresistance of (001)Fe/(001)Cr Magnetic Superlattices. *Phys. Rev. Lett.*, 61:2472, 1998.

[4] K. Matsuyama. *J. Magn. Soc. Jpn.*, 25:51, 2001.

[5] S. A. Wolf, D. D. Awschalom, R. A. Buhrman, J. M. Daughton, S. von Molnar, M. L. Roukes, A. Y. Chtchelkanova, and D. M. Treger. Spintronics: A Spin-Based Electronics Vision for the Future. *Science*, 294:1488, 2001.

[6] A. M. Haghiri, T. Arnal, R. Soulimane, M. Koubaa, and J. P. Renaud. Spintronics: perspectives for the half-metallic oxides. *phys. state. sol. (a)*, 201:1392, 2004.

[7] M. P. Singh, B. Carvello, and L. Ranno. Giant magnetoresistance in an all-oxide spacerless junction. *Appl. Phys. Lett.*, 89:022504, 2006.

[8] A. Nielsen, A. Brandlmaier, M. Althammer, W. Kaiser, M. Opel, J. Simon, W. Mader, S. T. B. Goennenwein, and R. Gross. All oxide ferromagnet/semiconductor epitaxial heterostructures. *Appl. Phys. Lett.*, 93:162510, 2008.

[9] X.-G. Zhang, W. H. Butler, and A. Bandyopadhyay. Effects of the iron-oxide layer in Fe-FeO-MgO-Fe tunneling junctions. *Phys. Rev. B*, 68:092402, 2003.

[10] C. Zhang, X.-G. Zhang, P. S. Krstic, H.-P. Cheng, W. H. Butler, and J. M. MacLaren. Electronic structure and spin-dependent tunneling conductance under a finite bias. *Phys. Rev. B*, 69:134406, 2004.

[11] S. H. Mirhosseini, K. K. Saha, A. Ernst, and J. Henk. Electron correlation effects in the magnetoresistance of Fe/MgO/Fe tunnel junctions: First-principles calculations. *Phys. Rev. B*, 78:012404, 2008.

[12] P. Bose, A. Ernst, I. Mertig, and J. Henk. Large reduction of the magnetoresistance in Fe/MgO/Fe tunnel junctions due to small oxygen concentrations at a single FeO interface layer: A first-principles study. *Phys. Rev. B*, 78:092403, 2008.

[13] S. A. Chambers. Epitaxial growth and properties of thin film oxides . *Surf. Sci. Rep.*, 39:105, 2000.

[14] J. F. Anderson, M. Kuhn, U. Diebold, K. Shaw, P. Stoyanov, and D. Lind. Surface structure and morphology of Mg-segregated epitaxial $Fe_3O_4(001)$ thin films on MgO(001). *Phys. Rev. B*, 56:9902–9909, 1997.

[15] K. A. Shaw. Interdiffusion study of magnesium in magnetite thin films grown on magnesium oxide (001) substrates . *J. Appl. Phys.*, 87:1727–1733, 2000.

[16] J. Wollschläger. Morphology and Defect Characterization of Epitaxial Oxide Films. *Defect and Diffusion Forum*, 164:37–56, 1998.

[17] Ch. Hagendorf, R. Shantry, H. Neddermeyer, and W. Widdra. Pressure-dependent Ni–O phase transitions and Ni oxide formation on Pt(111): An in situ STM study at elevated temperatures. *Phys. Chem. Chem. Phys.*, 8:1575, 2006.

[18] Ch. Hagendorf, S. Sachert, B. Bochmann, K. Kostov, and W. Widdra. Growth, atomic structure, and vibrational properties of MnO ultrathin films on Pt(111). *Phys. Rev. B*, 77:075406, 2008.

[19] T. Schedel-Niedrig, W. Weiss, and R. Schlogl. Electronic structure of ultrathin ordered iron oxide films grown onto Pt(111). *Phys. Rev. B*, 52:17449, 1995.

[20] H. C. Galloway, J. J. Benitez, and M. Salmeron. The structure of monolayer films of FeO on Pt(111). *Surf. Sci.*, 298:127, 1993.

[21] M. Ritter, W. Ranke, and W. Weiss. Growth and structure of ultrathin FeO films on Pt(111) studied by STM and LEED. *Phys. Rev. B*, 57:7240, 1998.

[22] W. Weiss and M. Ritter. Metal oxide heteroepitaxy: Stranski-Krastanov growth for iron oxides on Pt(111). *Phys. Rev. B*, 59:5201, 1999.

[23] W. Ranke, M. Ritter, and W. Weiss. Crystal structures and growth mechanism for ultrathin films of ionic compound materials: FeO(111) on Pt(111). *Phys. Rev. B*, 60:1527, 1999.

[24] S. K. Shaikhutdinov, M. Ritter, X. G. Wang, H. Over, and W. Weiss. Defect structures on epitaxial $Fe_3O_4(111)$ films. *Phys. Rev. B*, 60:11062, 1999.

[25] W. Weiss. Structure of epitaxial iron oxide films grown on Pt(100) determined by low energy electron diffraction . *Surf. Sci.*, 371:245, 1997.

[26] S. K. Shaikhutdinov, M. Ritter, and W. Weiss. Hexagonal heterolayers on a square lattice: A combined STM and LEED study of FeO(111) on Pt(100). *Phys. Rev. B*, 62:7535, 2000.

[27] J. Karunamuni, R. L. Kurtz, and R. L. Stockbauer. Growth of iron oxide on Cu(001) at elevated temperature. *Surf. Sci.*, 442:223, 1999.

[28] R. L. Kurtz, J. Karunamuni, and R. L. Stockbauer. Synthesis of epitaxial $Fe_3O_4$ films on Cu(001). *Phys. Rev. B*, 60:R16342, 1999.

[29] E. L. Lopes, G. J. P. Abreu, R. Paniago, E. A. Soares, V. E. Caravalho, and H. D. Pfannes. Atomic geometry determination of FeO(001) grown on Ag(001) by low energy electron diffraction . *Surf. Sci.*, 601:1239, 2007.

[30] M. Canepa, E. Magnano, A. Campora, P. Cantini, M. Salvietti, and L. Mattera. Diffusion by atomic place exchange in ultrathin iron films on Ag (100): an ion scattering spectroscopy study. *Surf. Sci.*, 352-354:36–40, 1996.

[31] M. H. Langelaar and D. O. Boerma. Fe adatoms on Ag(100): site exchange and mobility. *Surf. Sci.*, 395:131–137, 1998.

[32] M. A. Bravais. Mémoire sur les systèmes formé par des points distribués régulièrement sur un plan ou dans l'espace. *J. Ecole Polytech.*, 19:1–129, 1850.

[33] P. Herzog K. Kopitzki. *Einführung in die Festkörperphysik*. Teubner, 2002.

[34] E. A. Wood. Vocabulary of surface cristallography. *J. Appl. Phys.*, 35:1306, 1964.

[35] Jr. Strozier, D. W. Jepsen, and F. Jona. *Surface Physics of Materials*. Academic Press, 1975.

[36] A. Kroeck. SPA-LEED Untersuchungen an epitaktischen Co/Si(111)7 × 7 Schichten. Master's thesis, University of Hannover, 2002.

[37] D. E. Bürgler, C. M. Schmidt, D. M. Schaller, F. Meisinger, R. Hofer, and H.-J. Güntherodt. Optimized epitaxial growth of Fe on Ag(001). *Phys. Rev. B*, 56:4149, 1997.

[38] W. F. Egelhoff. X-Ray photoelectron and Auger electron forward-scattering studies of the epitaxial growth of Fe on Ag(001). *Mat. Res. Soc. Symp. Proc.*, 229:27–40, 1991.

[39] J. R. Smith and A. Banerjea. New Approach to Calculation of Total Energies of Solids with Defects: Surface-Energy Anisotropies. *Phys. Rev. Lett.*, 59:2451, 1987.

[40] L. J. Schowalter. Heteroepitaxy on Silicon by Molecular Beam Epitaxy. *Mat. Res. Soc. Symp. Proc.*, 116:3–14, 1988.

[41] G. Thomson. The early history of electron diffraction. *Contemp. Phys.*, 9:1–15, 1968.

[42] K. Oura, V. G. Lifshits, A. A. Saranin, A. V. Zotov, and M. Katayama. *Surface Science - An Introduction*. Springer, 2003.

[43] H. Bethe. Theorie der Beugung von Elektronen an Kristallen. *Ann. Phys.*, 392:1–75, 2006.

[44] S. Lindemann. Charakterisierung dünner Eisenoxidschichten auf Ag(111). Bachelor's thesis, University of Osnabrück, 2012.

[45] M. A. Van Hove, W. H. Weinberg, and C. M. Chan. *Low-Energy Electron Diffraction*, volume 6. Springer, 1986.

[46] S. Gevers. *Praseodymia on non-passivated and passivated Si(111) surfaces.* PhD thesis, University of Osnabrück, 2011.

[47] J. Wollschläger. *Ordnungsvorgänge in einatomaren Metallschichten auf hochindizierten Metallschichten.* PhD thesis, University of Hannover, 1990.

[48] J. Wollschläger, J. Falta, and M. Henzler. Electron Diffraction at Stepped Homogeneous and Inhomogeneous Surfaces. *Appl. Phys. A*, 50:57–68, 1989.

[49] M. Horn-von Hoegen, A. Al-Falou, H. Pietsch, B. H. Müller, and M. Henzler. Formation of interfacial dislocation network in surfactant mediated growth of Ge on Si(111) investigated by SPA-LEED. *Surf. Sci.*, 298:29, 1993.

[50] M. Horn-von Hoegen, T. Schmidt, G. Meyer, D. Winau, and K. H. Rieder. Lattice accommodation of low-index planes: Ag(111) on Si(001). *Phys. Rev. B*, 52:10764, 1995.

[51] H. Hertz. Ueber einen Einfluss des Ultravioletten Lichtes auf die electrische Entladung. *Wied. Ann.*, 31:983, 1887.

[52] W. Hellwachs. Ueber der Einfluss des Lichtes auf electrostatisch geladene Körper. *Ann. Phys.*, 269:301–312, 1888.

[53] A. Einstein. Ueber einen die Erzeugung und Verwandlung des Lichtes betreffenden heuristischen Gesichtspunkt. *Ann. Phys.*, 17:132, 1905.

[54] J. F. Moulder, W. F. Stickle, P. E. Sobol, and K. Bomben. *Handbook of X-ray Photoelectron Spectroscopy.* Physical Electronics Inc., Eden Prairie, USA, 1992.

[55] N. V. Alov. Fifty Years of X-ray Photoelectron Spectroscopy. *J. Anal. Chem.*, 60:297–300, 2004.

[56] T. Mizokawa, T. Saitoh, H. Namatame, and A. Fujimori. Electronic structure of 3d-transition-metal compounds by analysisof the 2p core-level photoemission spectra. *Phys. Rev. B*, 46:3771, 1992.

[57] P. Auger. The Auger effect. *Surf. Sci.*, 48:1–8, 1975.

[58] S. Jentsch. Epitaktische Eisenschichten auf Ag(001). Bachelor's thesis, Universisy of Osnabrück, 2010.

[59] C. C. Chang. Auger electron spectroscopy. *Surf. Sci.*, 25:53–79, 1971.

[60] J. C. Vickermann. *Surface Analysis - The Principal Techniques*. John Wiley & Sons, 2005.

[61] S. Mróz. Physical foundation of quantitative Auger analysis. *Prog. Surf. Sci.*, 46:377, 1994.

[62] D. A. Shirley. High-Resolution X-Ray Photoemission Spectrum of the Valence Bands of Gold. *Phys. Rev. B*, 5:4709, 1972.

[63] S. Hofmann. Practical surface analysis: state of the art and recent developments in AES, XPS, ISS and SIMS. *Surf. Interface Anal.*, 9:3–20, 1986.

[64] D. J. O'Connor, B. A. Sexton, and R. St. C. Smart. *Surface Analysis Methods in Material Science*. Springer-Verlag, 2003.

[65] G. Binning and H. Rohrer. Scanning Tunneling Microscopy. *Helv. Phys. Acta*, 55:726–735, 1982.

[66] H. Eisele. *Cross-Sectional Scanning Tunneling Microscopy of InAs/GaAs Quantum Dots*. PhD thesis, TU Berlin, 2001.

[67] C. Otte. Rastertunnelmikroskopie an epitaktischen Eisenschichten auf MgO(001). Master's thesis, University of Osnabrück, 2011.

[68] W. Nolting. *Grundkurs: Theoretische Physik 5, Quantenmechanik, Teil 1: Grundlagen*. Verlag Zimmermann-Neufang, 1996.

[69] P. Münster. Abbildungsprozesse beim STM auf atomarer Skala Simulation und Experimente. Master's thesis, University of Karlsruhe, 1997.

[70] L. Lichtenstein, M. Heyde, S. Ulrich, N. Nilius, and H.-J. Freund. Probing the properties of metal–oxide interfaces: silica films on Mo and Ru supports . *J. Phys.: Condens. Matter*, 24:354010, 2012.

[71] E. D. L. Rienks, N. Nilius, H.-P. Rust, and H.-J. Freund. Surface potential of a polar oxide film: FeO on Pt(111). *Phys. Rev. B*, 71:241404(R), 2005.

[72] J. Tersoff and D. R. Hamann. Theory of the scanning tunneling microscope. *Phys. Rev. Lett.*, 50:1998, 1983.

[73] J. Bardeen. Tunnelling from a Many-Particle Point of View. *Phys. Rev. Lett.*, 6:57–59, 1961.

[74] A. D. Gottlieb and L. Wesoloski. Bardeen's tunnelling theory as applied to scanning tunnelling microscopy: a technical guide to the traditional interpretation. *Nanotechnology*, 17:R57–R65, 2006.

[75] Z. Sun, S. K. Hamalainen, J. Sainio, J. Lahtinen, D. Vanmaekelbergh, and P. Liljeroth. Topographic and electronic contrast of the graphenemoireon Ir(111) probed by scanning tunneling microscopy and non contact atomic force microscopy. *Phys. Rev. B*, 83:081415(R), 2011.

[76] C. Silien, N. A. Pradhan, and W. Ho. Influence of adsorbate-substrate interaction on the local electronic structure of C60 studied by low-temperature STM. *Phys. Rev. B*, 69:115434, 2004.

[77] C. Ludwig, B. Gompf, J. Petersen, R. Strohmaier, and W. Eisenmenger. STM investigations of PTCDA and PTCDI on graphite and $MoS_2$. A systematic study of epitaxy and STM image contrast. *Z. Phys. B*, 93:365–373, 1994.

[78] I. Sebastian, T. Bertrams, K. Meinel, and H. Neddermeyer. Scanning tunnelling microscopy on the growth and structure of NiO(100) and CoO(100) thin films. *Faraday Discuss.*, 114:129–140, 1999.

[79] M. Winter. *Webelements*. The University of Sheffield and WebElements Ltd, UK, www.webelements.com, 2012.

[80] G. Ketteler, W. Weiss, W. Ranke, and R. Schlögl. Bulk and surface phases of iron oxides in an oxygen and water atmosphere at low pressure. *Phys. Chem. Chem. Phys.*, 3:1114–1122, 2001.

[81] F. Bertram. *The structure of ultrathin iron oxide films studied by x-ray diffraction*. PhD thesis, University of Osnabrück, 2012.

[82] B. Heinrich, K. B. Urquhart, A. S. Arrott, J. F. Cochran, K. Myrtle, and S. T. Purcell. Ferromagnetic resonance in ultrahigh vacuum of bcc Fe(001) films grown on Ag(001). *Phys. Rev. Lett.*, 59:1756–1759, 1987.

[83] W. R. Tyson and W. A. Miller. Surface free energies of solid metals- estimation from liquid surface tension measurements. *Surf. Sci.*, 62:267–276, 1977.

[84] R. M. Hanzen and R. Jeanloz. Wustite ($Fe_{1-\delta}O$): a review of its defect structure and physical properties. *Rev. Geophys.*, 22:37, 1984.

[85] J. Korecki, B. Handke, N. Spiridis, T. Slezak, F. Flis-Kabulska, and J. Haber. Size effects in epitaxial films of magnetite. *Thin Solid Films*, 412:14–23, 2002.

[86] R. Pentcheva, W. Moritz, J. Rundgren, S. Frank, D. Schrupp, and M. Scheffler. A combined DFT/LEED-approach for complex oxide surface structure determination: Fe3O4(001). *Surf. Sci.*, 602(7):1299–1305, 2008.

[87] N. Spiridis, J. Barbasz, Z. Lodziana, and J. Korecki. Fe3O4(001) films on Fe(001): Termination and reconstruction of iron-rich surfaces. *Phys. Rev. B*, 74:155423, 2006.

[88] U. Scheithauer, G. Meyer, and M. Henzler. A new LEED Instrument for Quantitative Spot Profile Analysis. *Surf. Sci.*, 178:441–451, 1986.

[89] H. Lüth. *Solid Surfaces, Interfaces and Thin Films.* Springer, 4. edition, 2001.

[90] I. Horcas, R. Fernandez.and J. M. Gomez-Rodriguez, J. Colchero, J. Gomez-Herrero, and A. M. Baro. WSXM: A software for scanning probe microscopy and a tool for nanotechnology. *Rev. Sci. Instrum.*, 78:013705–013705–8, 2007.

[91] G. Sauerbrey. Verwendung von Schwingquarzen zur Wägung dünner Schichten und zur Mikrowägung. *Zeitschrift fuer Physik A*, 155:206–222, 1959.

[92] G. Costantini, S. Rusponi, R. Gianotti, C. Boragno, and U. Valbusa. Temperature evolution of nanostructures induced by Ar+ sputtering on Ag(001). *Surf. Sci.*, 416:245–254, 1998.

[93] F. Bisio, R. Moroni, F. Buatier de Mongeot, M. Canepa, and L. Mattera. Isolating the Step Contribution to the Uniaxial Magnetic Anisotropy in Nanostructured Fe/Ag(001) Films. *Phys. Rev. Lett.*, 96:057204, 2006.

[94] G. Cipriani, D. Loffreda, A. Dal Corso, S. de Gironcoli, and S. Baroni. Adsorption of atomic oxygen on Ag(001): a study based on density-functional theory. *Surf. Sci.*, 501:182–190, 2002.

[95] Th. Bertrams and H. Neddermeyer. Growth of NiO(100) layers on Ag(100): Characterization by scanning tunneling microscopy. *J. Vac. Sci. Technol.*, 14:1141, 1996.

[96] P. C. J. Graat and M. A. J. Somers. Simultaneous determination of composition and thickness of thin iron-oxide films from XPS Fe 2p spectra. *Appl. Surf. Sci.*, 100/101:36, 1996.

[97] S. J. Roosendaal, B. van Asselen, J. W. Elsenaar, A. M. Vredenberg, and F. H. P. M. Habraken. The oxidation state of Fe(100) after initial oxidation in $O_2$. *Surf. Sci.*, 442:329, 1999.

[98] T. Schemme. Oxidation von Eisenschichten auf MgO(001)-Substraten. Master's thesis, University of Osnabrück, 2011.

[99] W. Weiss. Structure and composition of thin epitaxial iron oxide films grown onto Pt(111). *Surf. Sci.*, 377-379:943, 1997.

[100] T. Fujii, F. M. F. de Groot, G. A. Sawatzky, F. C. Voogt, T. Hibma, and K. Okada. In situ XPS analysis of various iron oxide films grown by $NO_2$-assisted molecular-beam epitaxy. *Phys. Rev. B*, 59:3195, 1999.

[101] M. Horn-von Hoegen, T. Schmidt, M. Henzler, G. Meyer, D. Winau, and K. H. Rieder. Epitaxial layer growth of Ag(111)-films on Si(100). *Surf. Sci.*, 331:575, 1995.

[102] W. Weiss and W. Ranke. Surface chemistry and catalysis on well-defined epitaxial iron-oxide layers . *Prog. Surf. Sci.*, 70:1, 2002.

[103] J. Wollschläger, D. Erdös, H. Goldbach, R. Höpken, and K. M. Schröder. Growth of NiO and MgO Films on Ag(100). *Thin Solid Films*, 400:1, 2001.

[104] C. Giovanardi, A. di Bona, S. Altieri, P. Luches, M. Liberati, F. Rossi, and S. Valeri. Structure and morphology of ultrathin NiO layers on Ag(001). *Thin Solid Films*, 428:195, 2003.

[105] M. Caffio, B. Cortigiani, G. Rovida, A. Atrei, C. Giovanardi, A. di Bona, and S. Valeri. Ultrathin nickel oxide films grown on Ag(001): a study by XPS, LEIS and LEED intensity analysis. *Surf. Sci.*, 531:368, 2003.

[106] Ch. Hagendorf, R. Shantyr, K. Meinel, K. M. Schindler, and H. Neddermeyer. Scanning tunneling microscopy and spectroscopy investigation of the atomic and electronic structure of CoO islands on Ag(001). *Surf. Sci.*, 532-535:346, 2003.

[107] K. M. Schindler, J. Wang, A. Chassé, H. Neddermeyer, and W. Widdra. Low-energy electron diffraction structure determination of an ultrathin CoO film on Ag(001). *Surf. Sci.*, 603:2658, 2009.

[108] F. Müller, R. de Masi, D. Reinicke, P. Steiner, S. Hüfner, and K. Stöwe. Epitaxial growth of MnO/Ag(001) films . *Surf. Sci.*, 520:158, 2002.

[109] E. A. Soares, R. Paniago, V. E. de Carvalho, E. L. Lopes, G. J. P. Abreu, and H. D. Pfannes. Quantitative low-energy electron diffraction analysis of MnO(100) films grown on Ag(100). *Phys. Rev. B*, 73:035419, 2005.

[110] A. Chassé, Ch. Langheinrich, F. Müller, and S. Hüfner. Growth and structure of thin MnO films on Ag(001) in dependence on film thickness . *Surf. Sci.*, 602:597, 2008.

[111] P. W. Tasker. The stability of ionic crystal surfaces. *J. Phys. C*, 12:4977, 1979.

[112] Y. J. Kim, C. Westphal, R. X. Ynzunza, Z. Wang, H. C. Galloway, M. Salmeron, M. A. Van Hove, and C. S. Fadley. The growth of iron oxide films on Pt(111): a combined XPD, STM, and LEED study. *Surf. Sci.*, 416:68–111, 1998.

# List of Figures

## List of peer-reviewed publications

- **D. Bruns**, S.Gevers and J. Wollschläger
  *Formation and morphology of step bunches during B-segregation on vicinal Si(111)*
  Surface Science **605**, 861–867 (2011).
  available at `http://dx.doi.org/10.1016/j.susc.2011.01.013`

- J. I. Flege, B. Kaemena, S. Gevers, F. Bertram, T. Wilkens, **D. Bruns**, J. Bätjer, T. Schmidt, J. Wollschläger and J. Falta
  *Silicate-free growth of high-quality ultrathin cerium oxide films on Si(111)*
  Physical Review B **84**, 235418 (2011).
  available at `http://link.aps.org/doi/10.1103/PhysRevB.84.235418`

- T. Kuschel, T. Becker, **D. Bruns**, M. Suendorf, F. Bertram, P. Fumagalli and J. Wollschläger
  *Uniaxial magnetic anisotropy for thin Co films on glass studied by magnetooptic Kerr effect*
  Journal of Applied Physics **109**, 093907 (2011).
  available at `http://dx.doi.org/10.1063/1.3576135`

- S. Gevers, T. Weisemoeller, **D. Bruns**, A. Giussani, T. Schroeder and J. Wollschläger
  *Post-deposition annealing of praseodymia films on Si(111) at low temperatures*
  Journal of Physics: Condensed Matter **23**, 115904 (2011).
  available at `doi:10.1088/0953-8984/23/11/115904`

- S. Gevers, J. I. Flege, B. Kaemena, **D. Bruns**, T. Weisemoeller, J. Falta and J. Wollschläger
  *Improved epitaxy of ultrathin praseodymia films on chlorine passivated Si(111) reducing silicate interface formation*
  Applied Physics Letters **97**, 242901 (2010).
  available at `http://dx.doi.org/10.1063/1.3525175`

## Acknowledgement

In the end, I would like to thank all the people who supported me during the work for this thesis.

Sincere thanks goes to my doctoral adviser Prof. Dr. Joachim Wollschläger, whose funded expertise and good advise was very helpful in countless situations during the last years.

I would also like to thank the members of my examination board Prof. Dr. Michael Rohlfing, Dr. Monika Wesner and especially my thesis examiner Prof. Dr. Marcus Bäumer from the University of Bremen, since the lecture of a doctoral thesis is always accompanied by a considerable effort of time.

I also acknowledge the Deutsche Forschungsgemeinschaft (DFG) via Graduate College 695 and its chair man apl. Prof. Dr. Klaus Betzler for financial support.

A special thanks is dedicated to Steffen Jentsch, Sören Lindemann and Irena Kiesel who directly assisted my work during their own bachelor or master theses. Your personal and scientific engagement provided the basis for this work.

This work did also benefit from the help of several other members and ex-members of my workgroup. Assisted measurements in the lab, technical support during repair phases and inspiring scientific discussions are only a few things to mention here. Without naming every one individually, I would really like to thank you all for your generous support.

My honest gratitude goes to my colleagues, mentors and friends Sebastian Gevers, Timo Kuschel and Martin Suendorf who shared an office with me for over four years. The valuable time with you during our work and after-work activities meant a lot to me.

From my whole heart I would like to thank my family and friends who gave me encouragement all the way during this thesis and beyond. Here, my parents Rita and Bernhard and my brother Sebastian are to mention first. Not only your financial support but especially your constant belief in me was a very big help. The next thanks goes to my best friend Malte Rosemann who supported me whenever I needed some balancing moments aside the lab.

The last but innermost thanks goes to my partner Vera Klose, who ceaselessly bolstered me during the last years and always found the right words to lift me up. I cannot measure all the work at home you relived me from to give me the necessary time to finish this thesis. You are the reason I could do this.

# Danksagung

Zu guter Letzt möchte ich gerne all denjenigen Personen danken, die mich während der Arbeit an dieser Dissertation unterstützt haben.

Aufrichtiger Dank gilt meinem Doktorvater Prof. Dr. Joachim Wollschläger. Seine fundierten Fachkenntnisse und sein guter Rat waren mir in zahllosen Situationen während der letzten Jahre eine unverzichtbare Hilfe.

Ich möchte auch den Mitgliedern meines Prüfungskomitees Prof. Dr. Michael Rohlfing, Dr. Monika Wesner und besonders meinem Zweitgutachter Prof. Dr. Marcus Bäumer von der Universität Bremen danken, denn die Lektüre einer Doktorarbeit ist immer mit einem großen Zeitaufwand verbunden.

Ich danke auch der Deutschen Forschungsgemeinschaft (DFG) in Vertretung durch das Graduiertenkolleg 695 und seinem Vorsitzenden apl. Prof. Dr. Klaus Betzler für die finanzielle Unterstützung.

Ein besonderer Dank ist an Steffen Jentsch, Sören Lindemann und Irena Kiesel gerichtet, die diese Doktorarbeit während ihrer eigenen Bachelor- und Masterarbeiten unterstützt haben. Euer persönliches und wissenschaftliches Engagement bildete die Grundlage für diese Arbeit.

Diese Arbeit hat zudem von der Hilfe vieler aktueller und ehemaliger Mitarbeiter meiner Arbeitsgruppe profitiert. Hilfe bei der Laborarbeit, technische Unterstützung bei Reparaturen und inspirierende, wissenschaftliche Diskussionen sind nur ein paar Dinge, die ich hier nennen möchte. Ohne jeden Einzelnen zu nennen, möchte ich euch allen herzlich für eure großzügige Hilfe danken.

Mein aufrichtiger Dank gilt meinen Kollegen, Mentoren und Freunden Sebastian Gevers, Timo Kuschel und Martin Suendorf, die sich mit mir über vier Jahre lang ein Büro geteilt haben. Die wertvolle Zeit während unserer Arbeits- und Freizeitaktivitäten bedeutete mir sehr viel.

Von ganzem Herzen danke ich meiner Familie und meinen Freunden, die mir im Verlaufe dieser Arbeit und darüber hinaus Rückhalt gegeben haben. Zuerst möchte ich an dieser Stelle meine Eltern Rita und Bernhard und mein Bruder Sebastian nennen. Nicht nur eure finanzielle Unterstützung, sondern umso mehr euer unablässiger Glaube an mich waren mir eine große Hilfe. Der nächste Dank geht an meinem besten Freund Malte Rosemann, der für mich da war wann immer ich etwas Zeit außerhalb des Labors brauchte.

Der letzte, aber innigste Dank gilt meiner Partnerin Vera Klose, die mich in den letzten Jahren unablässig unterstützte und stets die richtigen Worte fand um mich aufzubauen. Ich kann nicht ermessen, wie viel Arbeit du mir zu Hause abgenommen hast um mir die nötige Zeit zum Fertigstellen dieser Arbeit zu geben. Du bist der Grund dafür, dass ich dise Aufgabe meistern konnte.

# Eidesstattliche Erklärung

Hiermit erkläre ich an Eides Statt, die vorliegende Abhandlung selbständig und ohne unerlaubte Hilfe verfasst, die benutzten Hilfsmittel vollständig angegeben und noch keinen Promotionsversuch unternommen zu haben.

Osnabrück, 09.10.2012
Daniel Bruns